Defect Structure in Plastically Deformed High-Entropy Alloys

Anita Heczel

Ph.D. Dissertation

Supervisor: Prof. Jenő Gubicza, DSc

Eötvös Loránd University, Department of Materials Physics

Doctoral School of Physics Materials Science and Condensed Matter Physics program

Head of doctoral school: Prof. Tamás Tél
Head of doctoral program: Prof. István Groma

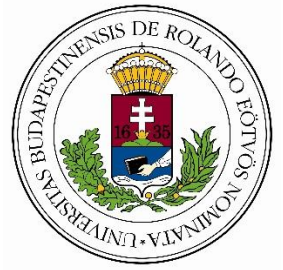

Budapest
2018

"Alloying is the greatest gift of metallurgy to humankind."

(B.S. Murty, J.W. Yeh and S. Ranganathan: High-entropy alloy)

TABLE OF CONTENTS

List of Figures

Fig. 3.9: The ratio of the correction factors for the indentation moduli with orientations 001 and 111. The curves correspond to the Poisson ratio (ν_{100}) values of 0.2, 0.25, 0.3, 0.35, 0.4 and 0.45. $(M_{001}/M_{111})_{exp}$ is the experimental value of the ratio of the indentation moduli measured in directions 001 and 111.

Fig. 3.10: The anisotropy factor A versus the Poisson ratio ν_{100} determined from the indentation moduli ratios for 001-101 and 001-111 orientation pairs. The two curves coincide at the anisotropy factor of 2.3 ± 0.2.

Fig. 3.11: TEM micrographs showing the dislocation patterning after compression test at room temperature for different plastic strains: (a) $\varepsilon \sim 1\%$; (b) $\varepsilon \sim 3\%$; (c) $\varepsilon \sim 10\%$ (The TEM images was taken at University of Paris 13).

Fig. 3.12: EBSD images showing the microstructure after impact deformation up to a true strain of ~50% at a velocity of 10 m/s (The EBSD image was taken at University of Paris 13).

Fig. 3.13: The yield strength as a function of the product of the modulus of the Burgers vector and the square-root of the dislocation density for the deformed HEA samples.

Fig. 3.14: Microstructure evolution in $Ti_{35}Zr_{27.5}Hf_{27.5}Nb_5Ta_5$ HEA during HPT deformation: a) Optical microscopy image of the initial sample, b) ACOM-TEM image showing the microstructure with orthorombic structure at the half-radius of the disk after 1 HPT turn.

Fig. 3.15: XRD patterns for (a) the initial $Ti_{35}Zr_{27.5}Hf_{27.5}Nb_5Ta_5$ HEA sample and (b) the half-radius of the disk processed by 1 turn of HPT. The orthorhombic peak positions are indicated by small vertical lines. In (b) the experimental diffractogram and the theoretical pattern fitted by the CMWP method are shown by open symbols and a solid line, respectively.

Fig. 3.16: True stress versus true strain curves obtained in compression test. The deformation was interrupted at the plastic strain of ~3.7% in order to investigate the microstructure, then the test was continued up to ~6.9% and ~11.5%.

Fig. 3.17: XRD patterns for (a) the sample deformed by compression to the plastic strain of ~3.7%, and (b) to the plastic strain ~11.5%. The peak positions are indicated by small vertical lines.

Fig. 3.18: EBSD images showing the bcc and orthorhombic phases after compression at the plastic strain of 3.7% (a) and 6.9% (b) (the green and the red regions represent the lamellae of bcc and orthorhombic phases, respectively).

Fig. 3.19: (a) SEM image showing the lamellar structure after compression at a plastic strain of 11.5% and (b) EBSD image showing the bcc and orthorhombic phases (the green and the red regions represent the bcc and orthorhombic phases, respectively).

Fig. 3.20: The Debye–Scherrer rings for the first five reflections after compression test at different strains.

Fig. 3.21: The average Vickers microhardness versus the distance from the center for the disk processed by 1 turn of HPT. The hardness obtained before HPT is also indicated which is much larger than three times the yield strength which is also shown in the figure as $3\sigma_y$.

Fig. 3.22: (a) EBSD image and (b) SEM-BSE picture for the initial as-cast sample. A part of (b) is shown in a higher magnification in (c). The chemical composition was investigated by EDS along the white dotted line in (c). The fractions of the five constituents versus the position along the dotted line are shown in (d).

Fig. 3.23: EBSD images showing the microstructures at (a) the center, (b) the half-radius and (c) the periphery of the HEA disk processed by 1/4 turn of HPT. The white arrows in (b) indicate twins formed due to HPT deformation. The color code for the maps is shown in the inset in Fig. 3.22a.

Fig. 3.24: EBSD images showing the center of the disks in the HEA sample after (a) 1/2, (b) 1 and (c) 2 turns of HPT. The thick black lines in (d) represent Σ3 boundaries and some twin crystals are indicated by white arrows. The color code for the maps is shown in the inset in Fig. 3.22a.

Fig. 3.25: Dark-field TEM images taken at the periphery of the disks processed by (a) 1/2, (b) 1(c) and 2 turns of HPT.

Fig. 3.26: Bright-field TEM images showing twinned grains at the periphery of the disk processed by 1 turn of HPT.

Fig. 3.27: The spatial distribution of the constituents in (a) the center and (b) the periphery of the CoCrFeMnNi HEA disk processed for ¼ turn and in (c) the center and (d) the periphery for 2 turns of HPT.

Fig. 3.28: Schematic depiction of the X-ray beam spot on the HPT-processed disks.

Fig. 3.29: Schematic showing that the total diffraction profile can be visualized as a sum of individual microstructural profiles scattered from regions with different lattice spacings. κ is the modulus of the scattering vector.

Fig. 3.30: (a) Reflection *200* for the initial material, as well as for the center and the periphery, of the disks processed for 1/4 and 2 turns of HPT, respectively. (b) the integral breadth versus the momentum of the diffraction vector, g (Williamson-Hall plot), for the initial material, as well as for the center and the periphery of the disks processed for 1/4 and 2 turns of HPT, respectively. (c) CMWP fitting for the center of the disk processed by 1/4 turn.

Fig. 3.31: (a) The grain size determined by EBSD or TEM, (b) the diffraction domain size and (c) the dislocation density obtained by XLPA as a function of shear strain imposed by HPT.

Fig. 3.32: The Vickers microhardness versus the distance from the center (a) and the shear strain (b) for the disks processed by HPT for 1/4, 1/2, 1 and 2 turns. The hardness plotted in (b) was calculated as the average of the two values obtained for the same distance from the center. The dashed line in (a) shows the average hardness for the initial sample without HPT. The error bars indicate the uncertainties in the hardness values.

Fig. 3.33: The yield strength estimated as one-third of the hardness versus the values calculated from eq. (3.12) for the center and the periphery of the disks processed by 1/4, 1/2, 1 and 2 turns.

Fig. 3.34: Elemental maps for the CoCrFeMnNi HEA obtained by EDS. The brighter the colour, the higher the concentration. The dashed and solid white circles indicate Co/Cr/Fe-rich and Mn/Ni-rich regions, respectively, where micropillar compression tests were carried out.

Fig. 3.35: A micropillar fabricated in a Co/Cr/Fe rich region (a) before and (b) after compression.

Fig. 3.36: Typical engineering stress-strain curves obtained by pillar compression for the Co/Cr/Fe-rich and the Mn/Ni-rich regions. The bars indicate the errors of the flow stress values determined from compressions of different pillars.

List of Tables

List of Acronyms

bcc	body-centered cubic
EBSD	electron backscatter diffraction
ECAP	equal-channel angular pressing
eCMWP	extended convolutional multiple whole profile (fitting procedure)
EDS	energy-dispersive X-ray spectroscopy
fcc	face-centered cubic
FIB	focused ion beam
FWHM	full width at half maximum
HAGB	high angle grain boundary
hcp	hexagonal close-packed
HEA	high-entropy alloy
HPT	high-pressure torsion
HV	Vickers hardness
IB	integral breadth
IP	imaging plate
IQ	image quality
LAGB	low angle grain boundary
SEM	scanning electron microscopy
SFE	stacking fault energy
SPD	severe plastic deformation
TEM	transmission electron microscopy
XLPA	x-ray line profile analysis

Introduction

Conventional solid solutions are generally based on one principle element, and other alloying atoms are added only in small concentrations for the improvement of properties. In the last decade, a new type of alloy concept, known as high-entropy alloys (HEAs), was proposed. HEAs are disordered solid solutions, containing five or more principal elements with atomic concentrations between 5% and 35%. These alloys are currently in the focus of materials science because they have desirable properties, such as high hardness and strength, good resistance to thermal softening, oxidation, wear and corrosion. The yield strength of these alloys can be further increased by refining the grain size and increasing the dislocation density.

The study of the plastic properties in HEAs is of great importance from the point of view of their practical applications. For the study of the plastic behavior of HEAs at high strains, severe plastic deformation (SPD) techniques must be applied. SPD is an effective tool for increasing the strength of materials. During SPD processing both the grain refinement and the increase in the dislocation density may contribute to hardening. SPD processing is expected to yield an additional improvement in hardness of HEAs. However, the evolution of the lattice defects, such as dislocations or twin-faults, during SPD and their influence on the mechanical behavior have not been deeply understood yet.

This thesis contains 3 chapters. In chapter 1, I review the current status of HEAs, with focus on mechanical properties. Then, in chapter 2 the experimental measurement techniques will be discussed, focusing on x-ray line profile analysis (XLPA). In chapter 3, my own research results are presented. I am going to show the evolution of microstructure in HEAs during SPD and uniaxial compression test.

The goal of my PhD work was to study the defect structure and mechanical properties of HEAs with different contents and crystal structures. The following alloys were investigated: $Ti_{20}Zr_{20}Hf_{20}Nb_{20}Ta_{20,}$ $Ti_{35}Zr_{27.5}Hf_{27.5}Nb_5Ta_5$ and $Co_{20}Cr_{20}Fe_{20}Mn_{20}Ni_{20}$ HEAs. I hope that my results will contribute to a deeper understanding of the relationship between lattice defects and mechanical properties of HEAs.

1 Literature Overview

In this chapter, the fundamental knowledge on HEAs is briefly reviewed. This will help to understand my own results and their discussion. The attractive properties of HEAs are due to four core effects. These are the cocktail effect, the high-entropy effect, the lattice distortion effect and the sluggish diffusion effect, which will all be described in the following sections. It is also important to discuss the effect of SPD on HEAs.

1.1 Basic Features of High-entropy Alloys

Conventional solid solutions are generally based on one principle element, and other alloying atoms are added only in small concentrations for the improvement of the properties. In the last decade, a new type of alloy concept, known as HEAs, was proposed [1,2]. These alloys are currently a focus of materials science due to their outstanding properties, such as high hardness and strength [3–6], good resistance to thermal softening [7–10], good corrosion resistance [11], outstanding wear and fatigue properties [12,13]. The first results on multi-component [1] and high-entropy alloys [2] were published in 2004, but the background work started much earlier [14–16]. It is not so easy to give a clear definition of HEAs. The different definitions may cause some confusion in materials science. Commonly, HEAs can be defined as single phase disordered solid solutions, containing five or more principal elements in equal or near-equal atomic ratios [2]. In practice, the atomic concentration for each constituent is usually between 5% and 35%. This is called as composition definition of HEAs. However, for example, an equiatomic alloy with 21 components is also a HEA, although the concentration of each element is smaller than 5 at% [17]. It is important to note that some authors have described four component alloys as HEAs [18–21].

Based on thermodynamics, the equilibrium of a material is achieved when the Gibbs free energy (G) reaches its minimum value. For an alloy, this minimum is

determined by the mixing component of the Gibbs free energy which can be expressed as:

$$\Delta G_{mix} = \Delta H_{mix} - T\,\Delta S_{mix}, \tag{1.1}$$

where ΔG_{mix} is the Gibbs free energy of mixing, ΔH_{mix} is the enthalpy of mixing, ΔS_{mix} is the entropy of mixing and T is the absolute temperature.

The statistical-mechanical definition of the entropy was developed by Ludwig Boltzmann in the 1870s [22] and he analysed first the statistical behavior of the microscopic components of a system [23]. Following Boltzmann's definition, for an alloy that consists of n elements with equal fractions the mixing configurational entropy can be given as:

$$\Delta S_{mix} = k\,ln\,w = -R\left(\frac{1}{n}ln\frac{1}{n} + \frac{1}{n}ln\frac{1}{n} + \cdots + \frac{1}{n}ln\frac{1}{n}\right) =$$

$$= -R\,ln\frac{1}{n} = R\,ln\,n, \tag{1.2}$$

where k is the Boltzmann's constant, w is the number of ways of mixing and R is the universal gas constant (8.314 J/K mol). For an equiatomic alloy (where all elements have the same concentration) with five different components, the configurational entropy equals $1.61R$. For a non-equiatomic HEA, the mixing entropy would be lower than this value. For example, the configurational entropy can be calculated as $1.523R$ for a nonequiatomic $Al_{33.3}Co_{22.2}Cr_{11.1}Fe_{22.2}Ni_{11.1}$ HEA which is slightly smaller than $1.61R$ of the equiatomic AlCoCrFeNi HEA [17]. Accordingly, Miracle et al. [6] recommended a configurational entropy-based definition that says if the $\Delta S_{mix} \geq 1.5R$, then the alloy can be called as HEA. This definition allows HEAs with two or more phases, opposite to the composition-based definition. As we know, the configurational entropy of a disordered solid solution is maximized by mixing a large number of alloying elements at near-equimolar concentrations and the high entropy of mixing stabilizes the disordered solid solution phases. For HEAs, the traditional alloy concept with solvent and solute elements can not be applied since these materials are composed of multiple principal elements.

Many factors infleunce the properties of HEAs. Yeh summarized the four main effects in his work [24]. These four "core effects" are often used to describe HEAs: the "cocktail" effect, the high-entropy effect, the lattice distortion effect and the sluggish diffusion [24]. In the next sections, I am going to discuss these four core effects briefly.

1.1.1 "Cocktail" Effect

The "cocktail effect" means that the properties of HEAs cannot be predicted from the properties of the constituent elements, because the behavior of HEAs depends on not only the properties of alloying elements but also on the mutual interaction among all the elements and from the severe lattice distortion [17]. Ranganathan [25] used first the phrase "cocktail effect" for metallic alloys, which was later confirmed by the investigation of mechanical and physical properties [26–29]. For example, with the increase of the Al content in $CuCoNiCrAl_xFe$ HEAs, the phase composition changes from fcc to the mixture of bcc and fcc phases, and then to bcc structures as shown in Fig. 1.1 [2]. Thus, the structures of the components do not determine the structure of the HEA. It can be seen that the lattice constants for both bcc and fcc phases increased, and the hardness was also dramatically enhanced with increasing Al concentration. Fig. 1.2 shows the change of the hardness as a function of the Al content in another HEA which contained the same elements as the formerly discussed HEA, except Cu (e.g., the composition is $CoNiCrAl_xFe$) [30]. The hardness of the fcc phase hardly changed with increasing Al content ($x=0—0.45$), while the hardness of the bcc phase decreased from about HV 538 to HV 480 as the Al content increased ($x=0.88—2.0$). Furthermore, the phase transformation from fcc to bcc starts at smaller x values for $CoNiCrAl_xFe$ compared to $CuCoNiCrAl_xFe$ (see Fig.1.1), which suggests that Cu stabilizes the fcc phase [5].

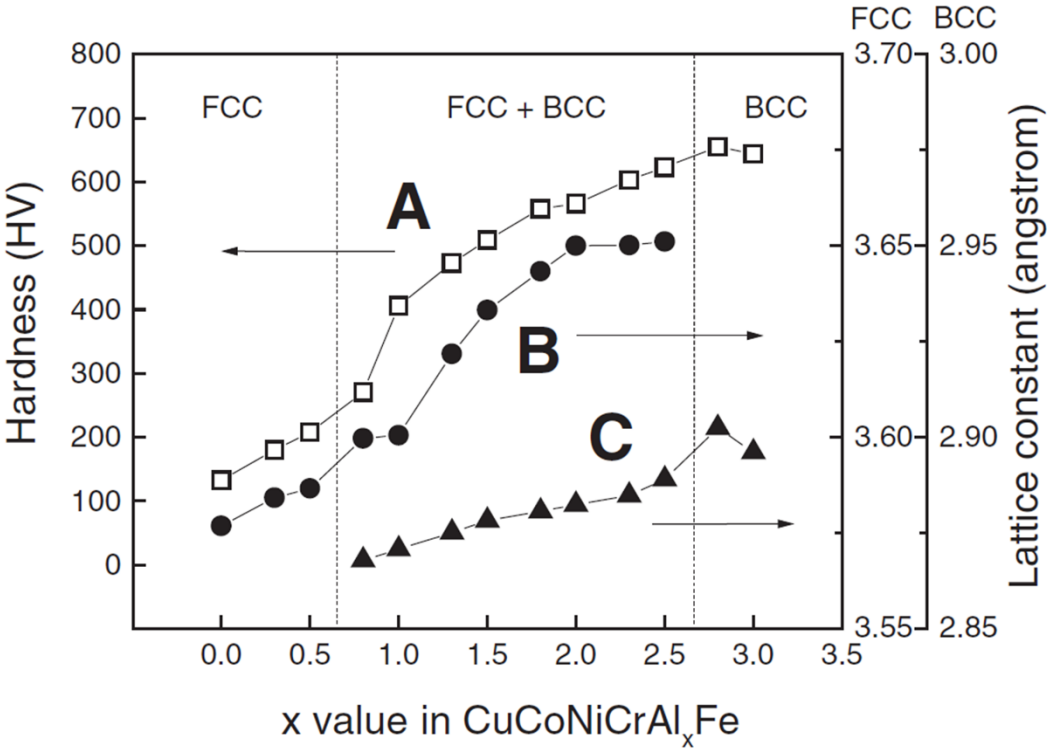

Fig. 1.1: Hardness and lattice constants of a CuCoNiCrAl$_x$Fe alloy system with different x values: (A) hardness of CuCoNiCrAl$_x$Fe alloys, (B) lattice constants of an fcc phase, (C) lattice constants of a bcc phase [2].

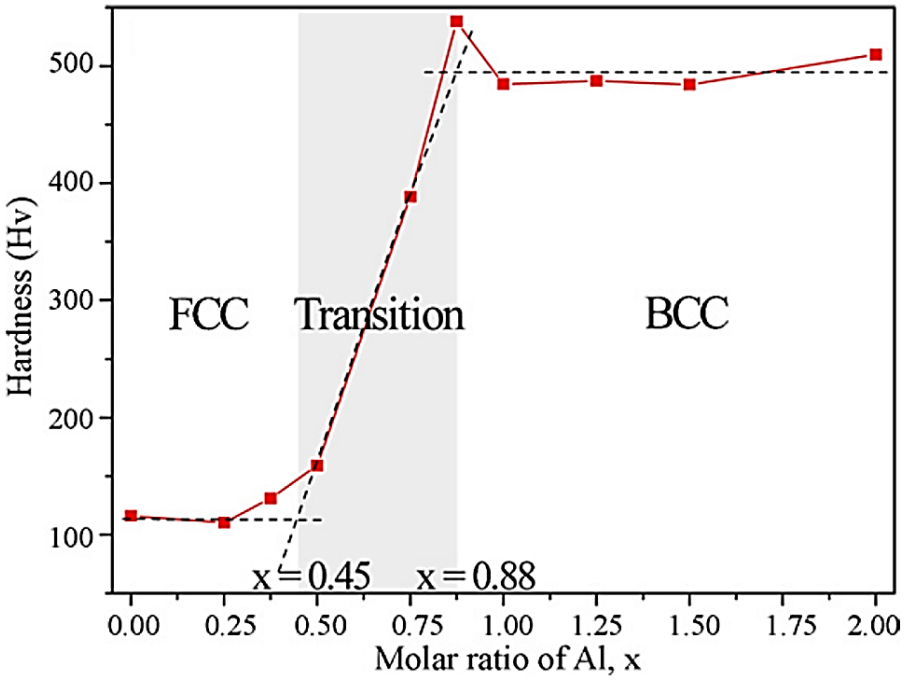

Fig. 1.2: Hardness of a CoNiCrAl$_x$Fe alloy system with different x values [30].

1.1.2 High-entropy Effect

The high-entropy effect has already been mentioned in the beginning of Section 1.1. First Yeh [24] suggested that the high-entropy effect stabilizes the high-entropy phases such as the disordered solid solutions. Fig. 1.3 illustrates chemically compatible elements before and after mixing in a disordered solid solution. It was obtained that HEAs form solid-solution phases rather than intermetallic phases due to their high mixing entropies [1,2,32], especially at elevated temperatures because the entropy contribution to the Gibbs energy in equation (1.1) increases with increasing temperature. This does not mean that all multi-component-alloys in equal molar ratio will create solid solution phases. Rather, it was found that only carefully selected compositions will form solid solutions instead of intermetallic compounds [17].

The high-entropy effect blocks the formation of intermetallic phases and helps the formation of solid solution phases. The entropy alone is not enough to stabilize the solid solution phase in HEA systems. The mixing enthalpy should also be taken into account which can be calculated as [32]:

$$\Delta H_{mix} = \sum_{i=1, i\neq j}^{N} 4\Delta H_{ij}^{mix} c_i c_j, \tag{1.3}$$

where c_i and c_j are the atomic percentages of the *ith* or *jth* element, ΔH_{ij}^{mix} is the enthalpy of mixing between the *ith* and *jth* elements at the equimolar composition. Zhang et al. [33] suggested that in order to form a complete solid solution ΔH_{mix} must be between -10 and 5 kJ/mol. Moreover, Otto et al. [34] found that if an equiatomic HEA contains a pair of elements that are inclinable to form ordered compounds in their binary system, this HEA material also likely forms an ordered compound. The mixing entropy, ΔS_{mix} and the mixing enthalpy, ΔH_{mix} can be combined into a single parameter Ω:

$$\Omega = \frac{T_m \Delta S_{mix}}{|\Delta H_{mix}|}, \tag{1.4}$$

where T_m is the average melting point of the elements in the alloy. Ω is a unitless parameter and should be ≥1.1 to form solid solution in HEAs.

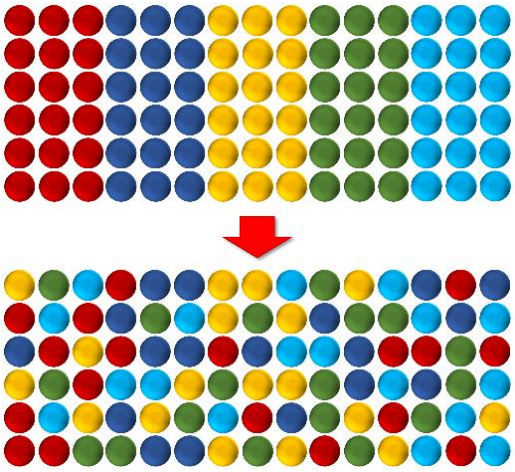

Fig. 1.3: Schematic illustration demonstrating a five-component alloy with equiatomic ratios before and after mixing.

1.1.3 Lattice Distortion Effect

The lattice distortion in HEAs may influence the properties of these materials. This distortion is caused by the different radii and bonding energies of the constituents [36,37]. Fig. 1.4 shows schematically the severe lattice distortion in a five-component bcc HEA lattice. The three-dimensional unit cell is highly distorted and the composition changes from cell to cell. However, an average lattice parameter can be determined by X-ray diffraction.

The lattice distortion in HEAs has a significant effect on the mechanical properties. The large friction stress in the severely distorted lattice effectively increases the hardness and strength of HEAs [17]. For example, Senkov et al. [37] studied the hardness of a coarse-grained refractory MoNbTaVW alloy with bcc structure, and the Vickers microhardness was found to be 5250 MPa at room temperature which is higher than the hardness of any individual constituent (each of them has a bcc structure in pure form).

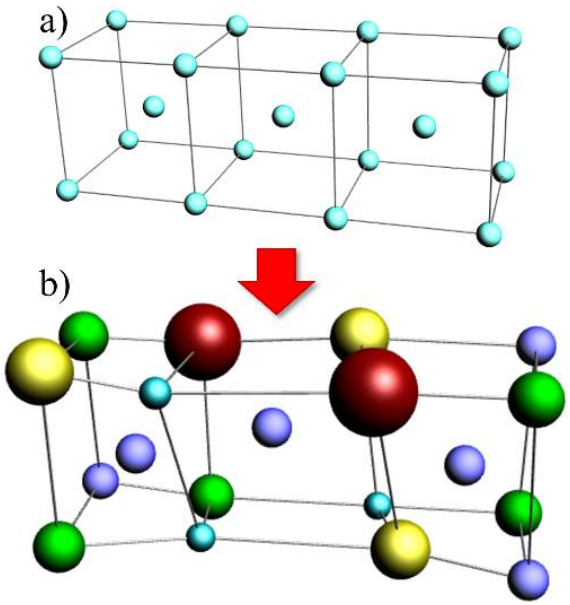

Fig. 1.4: Schematic illustration of a bcc crystal structure: (a) perfect lattice and (b) severely distorted lattice. The balls with different colors represent different elements in the material.

1.1.4 Sluggish Diffusion Effect

During a diffusion-driven phase transformation, the formation of new phases requires a simultaneous diffusion of different atoms. It was suggested that the diffusion and phase transformation kinetics in HEAs are slower than in conventional alloys [3]. In disordered solid solutions, the chemical environments of the neighboring lattice sites are somewhat different. Thus, before and after an atom jumps into a vacancy the neighbors are different. The difference in local atomic configuration leads to different local energies of the neighboring sites. When an atom jumps into a low potential energy site, it is trapped which inhibits further diffusion of this atom [3]. This causes the sluggish diffusion effect because a higher thermal activation is needed for the atomic migration which slows down the diffusion in the material.

Tsai et al. [36] measured the diffusion parameters in the CoCrFeMnNi HEA using the diffusion pair method. The results of this measurement were compared

with similar fcc lattices, including FeCrNi(Si) alloys and pure Fe, Co and Ni metals. It was found that the diffusion rates of each element in the CoCrFeMnNi HEA were low, which was caused by a higher activation energy of diffusion. M. Dabrowa et al. [38] studied the interdiffusion parameters in non-equimolar AlCoCrFeNi HEA and determined the tracer diffusion coefficients of the elements. These results also support the theory of sluggish diffusion in HEAs. Recently, Vaidya et al. [39] studied the tracer diffusivities of Ni in the equiatomic CoCrFeNi and CoCrFeMnNi alloys and showed that at any given temperature, the diffusion rate of Ni in the CoCrFeMnNi alloy was even faster than that in the CoCrFeNi alloy. They concluded that diffusion in HEAs is not inevitably decelerated and its rate is very sensitive to the composition of the alloy. Currently, there is not enough data for a deeper understanding of the diffusion processes in HEAs.

1.2 Processing of HEAs

Processing of HEAs does not require special processing techniques or equipment, therefore mass production of HEAs can easily be achieved with the existing equipments and technologies. The processing of HEAs is similar in equimolar and non-equimolar cases. Various processing methods are available for the production of HEAs; one of the most commonly used methods is the melting and casting of the alloys. Most frequently, the melting is done via vacuum arc melting, but sometimes via vacuum induction melting, followed by casting, often copper mold casting [17]. To achieve a homogeneous distribution of elements in HEAs, the melting and solidification processes are repeated several times.

Different processing methods, such as sputtering, molecular beam epitaxy, thermal spray, spark plasma sintering, laser cladding, and electrodeposition have successfully been employed in the production of HEAs [5,38–43]. In the past few years, many different HEAs were produced by powder metallurgy. This process can mainly produce nanocrystalline bulk HEAs [44–46]. More details on the processing of the HEAs studied in this thesis will be given in section 3.

1.3 Microstructure of HEAs

During arc melting and casting, usually a heterogeneous microstructure is formed due to segregation mechanisms caused by the slow rate of solidification. Fig. 1.5 shows a typical dendritic microstructure of a HEA produced by arc melting [49]. Similar dendritic microstructure can be seen in many other alloys produced by induction melting and casting.

Singh et al. [50] studied AlCoCrCuFeNi HEA processed by induction melting and casting. It was shown that splat quenching (at a rapid cooling rate of 10^6-10^7 K/s) led to the formation of a bcc ordered phase. At the same time, production at lower cooling rates of 10-20 K/s yielded a phase separation into six phases with bcc and fcc structures. Cantor and his co-workers [1] showed that equiatomic HEAs, such as CoCrFeMnNi, CoCrFeMnNiNb, CoCrFeMnNiTi, CoCrFeMnNiV, CoCrFeMnNiCu and CoCrFeMnNiGe, manufactured by casting and melt spinning led to predominantly single fcc phase. This work also showed that faster cooling prevented the precipitation of secondary phases, leading mainly to the formation of single phase alloys.

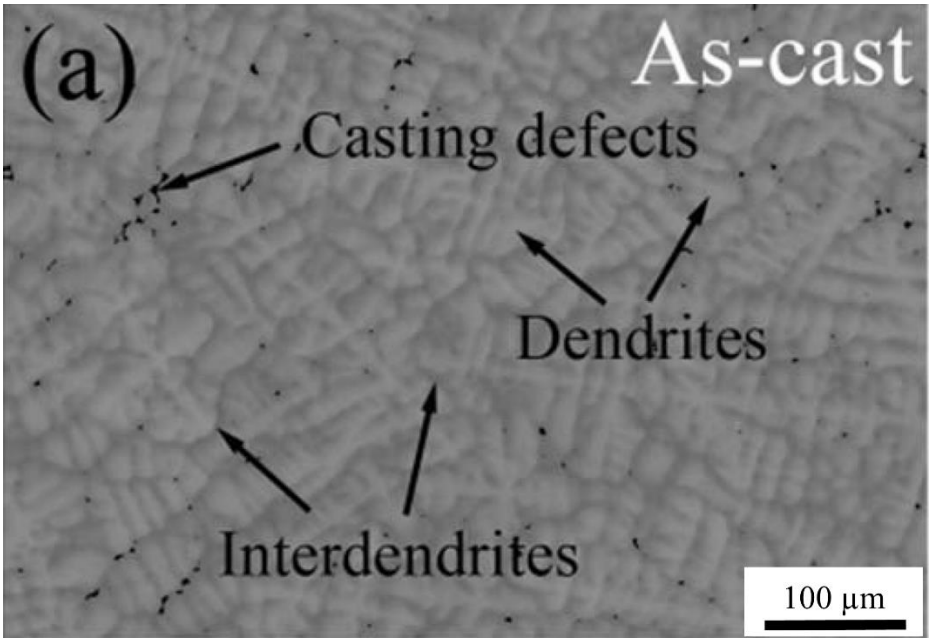

Fig. 1.5: Microstructure of the as-cast Cr–Mo–Nb–V sample produced by arc melting [49].

The major disadvantage of conventional cast alloys is the microstructural coarseness or non-uniformity of grain size. In HEAs prepared by vacuum arc-melting technology, coarse grains and a dendritic microstructure was also observed [49,50]. Fig. 1.6 shows a coarse grained dendritic microstructure in an equiatomic CoCrFeMnNi HEA obtained by induction melting.

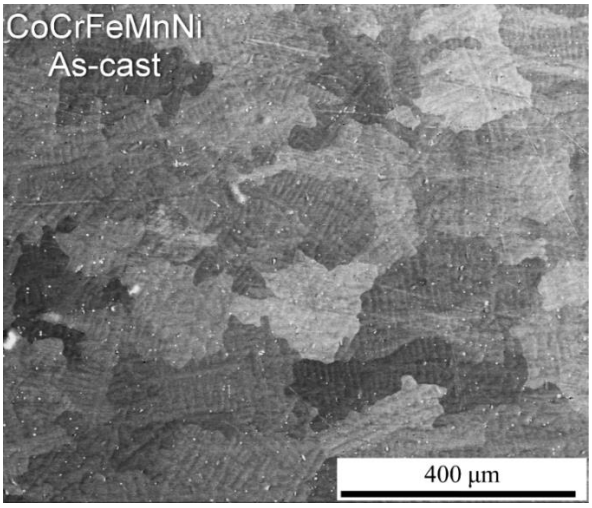

Fig. 1.6: The microstructure of the as-cast CoCrFeMnNi HEA. The grain size is few hundred micrometers.

1.4 Mechanical Properties of HEAs

The mechanical properties of HEAs usually differ from the properties of their components [53]. In addition, the crystal structure of HEAs strongly influences their mechanical strength. For instance, the yield strength of coarse-grained HEAs varies from ~300 MPa for fcc-structured alloys [28], such as the CoCrCuFeNiTix system, to about ~3000 MPa for bcc-structured alloys, such as the AlCoCrFeNiTix system [29]. $CuCoNiCrAl_xFe$ HEAs have been extensively studied in the literature [52–54]. The hardness of this alloy increases from 133 HV for x=0–0.5 to 655 HV for x=3.0 [54] (see Fig. 1.1), which can be attributed to the increase of the lattice distortion. Li et al. [57] showed a similar effect on hardness in other Al-containing HEA alloys. In another work, Chen et al. [58] reported that the addition of vanadium (V) to the $Al_{0.5}$CoCrCuFeNi alloy increased the hardness. If the additional elements have a larger atomic size, then secondary phases can be formed which causes precipitation

strengthening. For example, Li et al. [57] studied ten different types of HEAs, and the highest hardness was achieved with the addition of zirconium (Zr) and aluminium (Al) that have larger atomic sizes than for other elements in the studied alloys, and caused precipitation of secondary phases. Fig. 1.7 shows the specific-yield strength (defined as the yield strength over the density) versus the Young's modulus for some HEAs, bulk metallic glasses and conventional alloys. As shown in the figure, HEAs generally show superior specific strength compared to conventional alloys. The alloy VNbMoTaW, a well-known refractory bcc HEA, shows higher specific yield strength than most of stainless steels and nickel alloys. The specific strength of Al-containing HEAs such as $AlCoCrFeNiTi_{1.5}$ and $AlCoCrFeNiTi_{0.5}$ is even higher than that of VNbMoTaW, owing to their high content of light elements such as aluminum. We can see that the Young's modulus of HEAs spans a very large range.

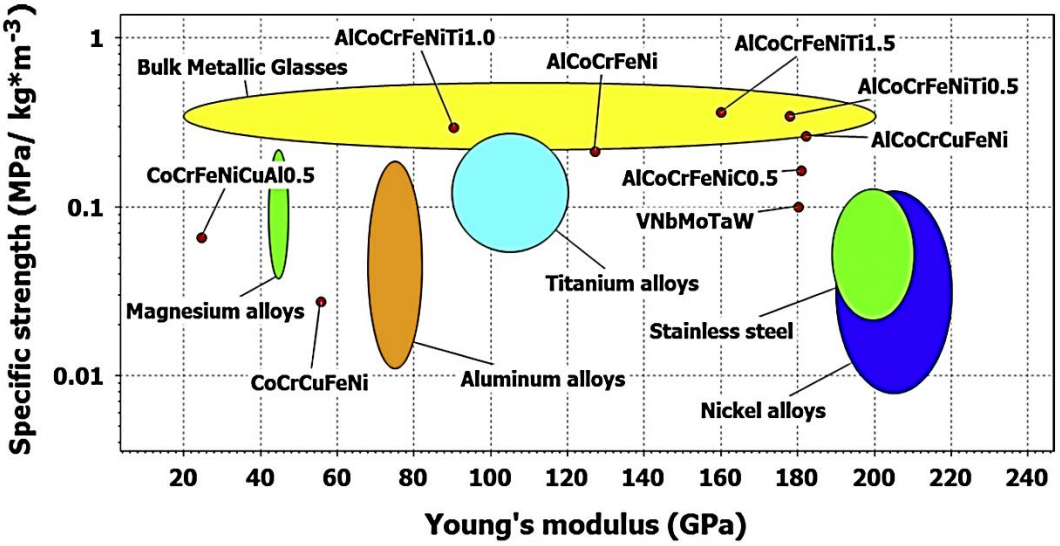

Fig. 1.7: Specific-yield strength vs. Young's modulus. The HEAs are compared with other materials, such as bulk metallic glasses and structural alloys [5].

The mechanical properties of HEAs can be different from the constituent elements. The crystal structure type is the main factor for controlling the strength or hardness of these alloys [5]. The fcc-structured HEAs are known to possess good ductility, but with relatively low strength [59], in contrast to bcc-structured HEAs that can have much higher strength, but almost always at the expense of ductility [37]. In fcc HEAs, dislocation slip and nanotwinning can lead to a large strain hardening [79–81]. In bcc HEAs, twinning is less noticeable during deformation

which may contribute to the lower strain hardening compared to that of fcc HEAs [8]. The mixture of bcc + fcc is expected to possess balanced mechanical properties, e.g., both high strength and good ductility. The AlCoCrCuFeNi HEA has a two-phase bcc+fcc structure. Wen et al. [63] studied the effect of temperature on the microstructure and mechanical properties. They found that annealing at~800 °C or below increased the fraction of the bcc phase. Annealing at temperatures higher than 800 °C increased the fraction of the fcc phase. Because the fcc phase is ductile and the bcc phase is relatively brittle, therefore annealing can be used to improve the mechanical properties.

Senkov et al. [7] studied the temperature dependence of the yield stress of two refractory $Nb_{25}Mo_{25}Ta_{25}W_{25}$ and $V_{20}Nb_{20}Mo_{20}Ta_{20}W_{20}$ HEAs and two high-temperature Ni-based superalloys, Inconel 718 and Haynes 230. The yield strength values were measured in the temperature range from room temperature to 1600 °C. They found that the yield strength of HEAs was much higher than that of Haynes 230 and Inconel 718 alloys at temperatures above 800 °C (see Fig. 1.8). In addition, the decrease in the yield strength of these refractory HEAs in the temperature range from 600 °C to 1600 °C is rather weak [7].

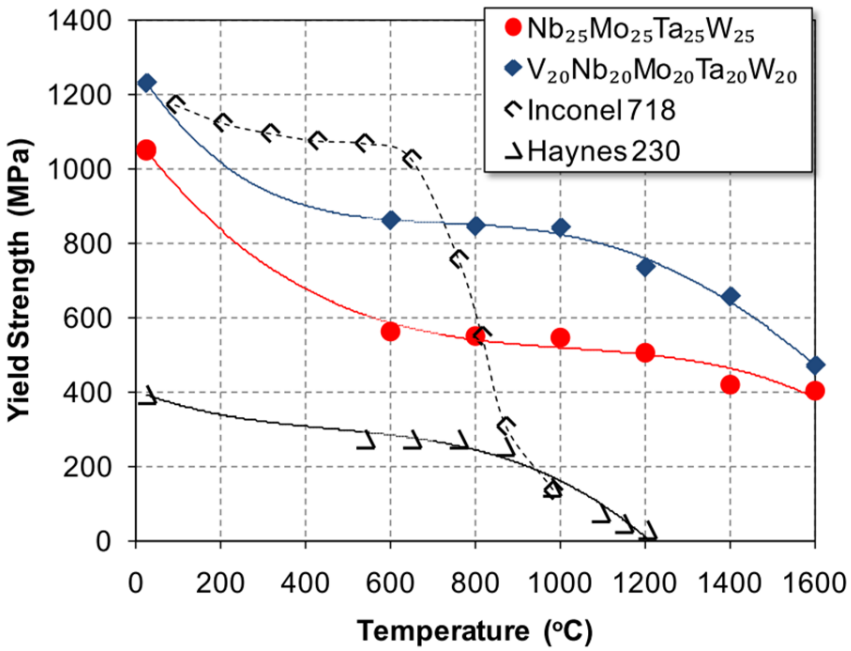

Fig. 1.8: Temperature dependence of the yield strength of NbMoTaW and VnbMoTaW HEAs, as well as Inconel 718, and Haynes 230 alloys [7].

Fig. 1.9 shows an Ashby map showing ultimate tensile strength versus density for structural metals, along with the data for bulk metallic glasses and HEAs [64]. The grey dashed lines show the specific strength from low (right bottom) to high (left top) values. It can be concluded that HEAs have a better combination of strength and density, compared to the majority of the conventional crystalline alloys (see Fig. 1.9) [64]. The ultimate tensile strength versus density data for HEAs are comparable to bulk metallic glasses. However, due to the crystalline structure the ductility of HEAs is much better than that for bulk metallic glasses.

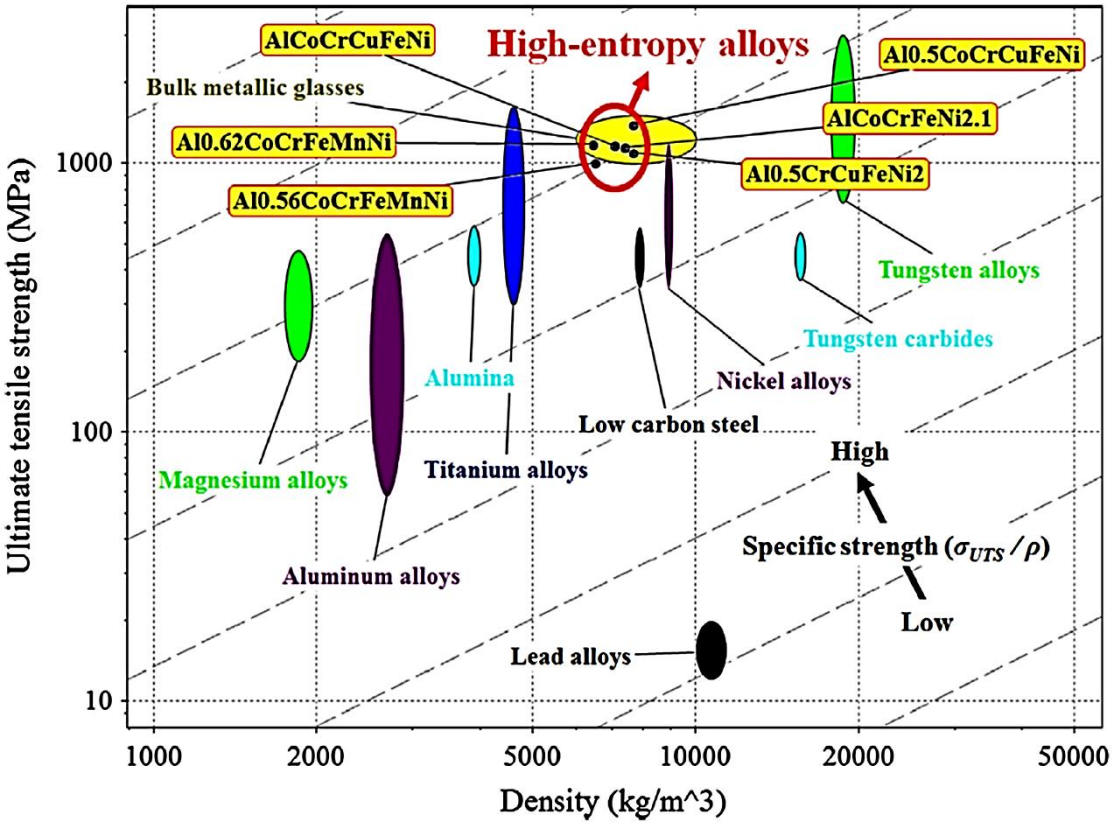

Fig. 1.9: An Ashby map showing ultimate tensile strength versus density for structural materials, along with the data for bulk metallic glasses and HEAs. The grey dashed lines label the specific strength from low (right bottom) to high (left top) values. HEAs are among the materials that have a better combination of mechanical properties of strength and density, compared to other materials [64].

1.5 Severe Plastic Deformation of HEAs

SPD is an effective tool for increasing the strength of materials [69,70]. During SPD processing, both grain refinement and an increase in dislocation density may contribute to hardening. SPD-induced grain refinement can occur mainly by dislocation activities or by combined deformation twinning and dislocation activities [71,72]. High-pressure torsion (HPT) is one of the most effective SPD techniques for achieving high strength in structural materials [69]. HPT processing is expected to yield an additional improvement in hardness of HEAs. Indeed, HPT-straining for an fcc CoCrFeNiMn and a bcc AlTiVNb HEAs resulted in an improvement in hardness due to the reduction of grain size into the nanocrystalline regime [74,75]. In an $Al_{0.3}Cu_{0.5}$CoCrFeNi HEA, HPT processing led to both significant grain refinement to about 50 nm and homogenization of the elemental distribution [72]. It should be noted that annealing at appropriate temperatures after HPT may yield additional hardening due to the formation of secondary phase particles, e.g., an ordered bcc phase in fcc $Al_{0.3}$CoCrFeNi HEA [73]. In fcc FeCoCrNi HEA, nanoband subdivision and deformation twinning contributed to the grain refinement, resulting in a significant reduction of the average grain size from ~25 μm to ~68 nm [74].

1.6 Motivation

HEAs are usually prepared by vacuum arc-melting technology, as described in section 1.2. Ingot metallurgy tends to create coarse grains with heterogeneous dendritic structures during cooling. In order to improve the mechanical properties, additional deformation methods can be employed, such as HPT.

The study of the plastic properties of HEAs is important from the point of view of their practical applications. For the investigation of the plastic behavior of HEAs at high strains, SPD techniques must be applied. SPD methods are promising tools to improve the mechanical properties of HEAs. During SPD processing, both grain refinement and an increase in the dislocation density occur that may contribute to hardening. The evolution of the lattice defects, such as dislocations or twin-faults during SPD and their influence on the mechanical behavior have not been deeply investigated. Therefore, a better understanding of the relationship between lattice defects and mechanical properties of HEAs is necessary.

The goal of my PhD work was to study the defect structure and mechanical properties of HEAs with different contents and crystal structures. The following alloys were investigated: a bcc $Ti_{20}Zr_{20}Hf_{20}Nb_{20}Ta_{20,}$ a bcc $Ti_{35}Zr_{27.5}Hf_{27.5}Nb_5Ta_5$ which was transformed to an orthorhombic structure during deformation, and an fcc $Co_{20}Cr_{20}Fe_{20}Mn_{20}Ni_{20}$ HEA. The defect structure was studied mainly by X-ray line profile analysis which method yields a good statistics of the results due to the relatively large studied volume.

2 Experimental Methods

In this section, I introduce the experimental methods used in my research. First, I show the fundamentals of the HPT technique used for the grain refinement, then I give a description of the methods applied in the characterization of the microstructure and the mechanical properties, such as microhardness measurement, transmission electron microscopy (TEM), scanning electron microscopy (SEM) etc. I used X-ray line profiles analysis (XLPA) for most of my doctoral work, so a detailed overview of this method is also presented.

2.1 Processing of HEAs by High-pressure Torsion

HPT is one of the most effective SPD technique in achieving high strength in structural materials [69]. HPT processing is expected to yield an additional improvement in hardness of HEAs. In this method, the sample in the form of a disk is located between two anvils. A large compressive stress (typically several GPa) is applied at room temperature, while the lower anvil is rotated to create a torsion deformation. In this process, the surface frictional forces deform the disk by shear [69]. During the HPT process, high plastic strains are achieved, resulting in materials with microstructures in the nanocrystalline or ultrafine-grained regime. The principle of the HPT process is illustrated schematically in Fig. 2.1. The number of revolutions, the rate of deformation and the temperature can be controlled and changed during processing. The shear strain (γ) imposed by HPT can be given as [69]:

$$\gamma = \frac{2\pi N \cdot r}{h}, \tag{2.1}$$

where N is the number of turns, r is the distance from the disk center and h is the height of the disk.

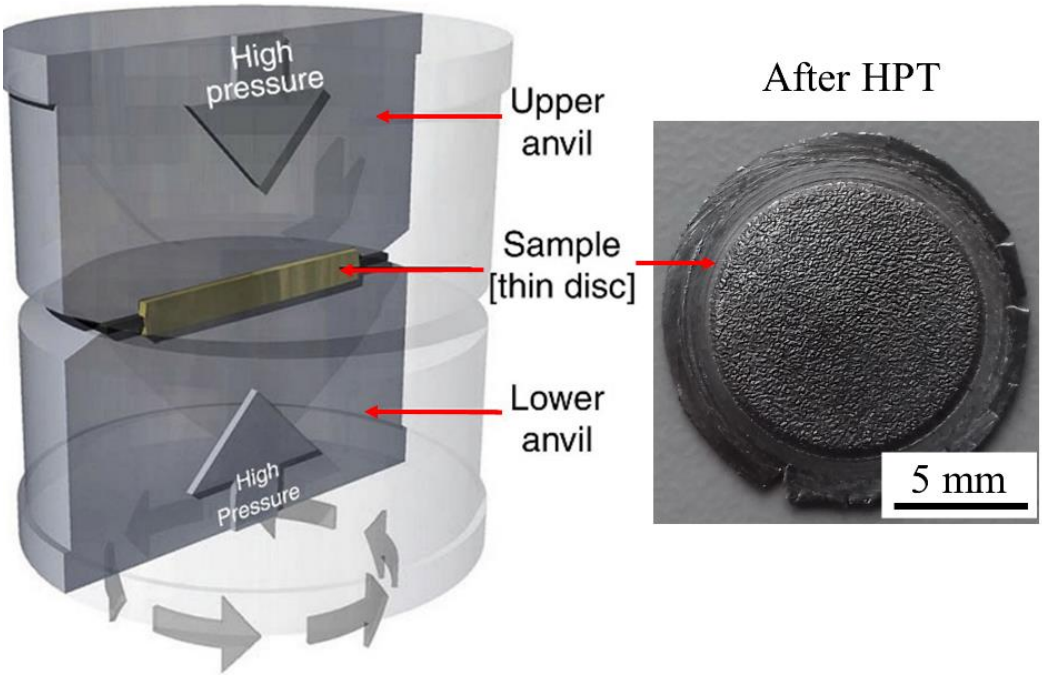

Fig. 2.1: Schematic view of the HPT process [75] and a HEA sample processed by 2 turns of HPT.

The equivalent strain can be calculated using the relationship [76]:

$$\varepsilon_{eq} = \frac{\gamma}{\sqrt{3}}. \tag{2.2}$$

It can be seen from the eq. 2.1, the strain is equal to zero at the center of the disk and increases linearly until reaching a maximum value near the periphery of the disk. Therefore, the microstructure of the deformed sample is heterogeneous. Consequently, the microhardness also changes significantly along the radius of the disks processed by HPT [119–121]. It is possible to obtain homogeneous structures along disk diameter by increasing the total number of HPT turns and by increasing the applied pressure [122,123].

There are only a few reports describing the influence of HPT processing on HEAs [124–129]. From the articles published so far, it can be seen that HPT is an effective method to improve the mechanical properties of HEAs. Grain refinement by HPT processing leads to excellent properties of HEAs.

2.2 X-ray Diffraction

The Bragg's equation expresses the correlation between the X-ray wavelength (λ), the interplanar spacing (d_{hkl}) for planes (hkl) and the scattering angle (θ):

$$2d_{hkl}sin\theta = \lambda \tag{2.3}$$

It follows that we can determine the lattice parameter (a) if the reflections are indexed, using the following equation for a cubic structure:

$$d_{hkl} = \frac{a}{\sqrt{h^2 + k^2 + l^2}}, \tag{2.4}$$

and another formula for an orthorhombic structure:

$$\frac{1}{{d_{hkl}}^2} = \frac{h^2}{a^2} + \frac{k^2}{b^2} + \frac{l^2}{c^2} \tag{2.5}$$

where *a, b, c* are the lattice parameters. Since in this thesis only cubic and orthorhombic materials are investigated, the formulas for other structures are not presented here but they can be found in the literature [88].

2.3 X-ray Line Profile Analysis

The purpose of line profile analysis is to determine the characteristic parameters of the microstructure from the shape of the diffraction peaks (e.g., crystallite size distribution, the type and density of dislocations) [88]. Any deviation from the perfect lattice leads to changes in the shape of the peaks [89]. These changes are caused by various microstructural elements: finite crystallite size, dislocations, twin and stacking faults, chemical heterogeneities, etc. It is important to note that there is one more broadening effect caused by the instrument [84,85].

The great advantage of this examination method is that the measurement is technically simple. In addition, it does not require any special sample preparation,

and it provides information from a larger volume than the conventional direct test methods, such as transmission or scanning electron microscopy (TEM or SEM). However, it is noted that chemical or electrochemical treatment of the sample surface is necessary before the measurement in order to remove the uppermost surface layer which may be distorted due to cutting and/or mechanical polishing.

According to the kinematical theory of diffraction, the measured intensity profile can be described as the convolution of the intensity profiles of the crystallite size, lattice defects, planar faults and instrumental broadening [86–89]. Therefore, the Fourier-coefficients of the measured profile, A^M, can be expressed using the following equation:

$$A^M(L) = A^S(L) \cdot A^D(L) \cdot A^{PF}(L) \cdot A^I(L), \tag{2.6}$$

where A^S, A^D, A^{PF} and A^I are the Fourier-coefficients of the size, strain (distortion), planar faults and instrumental broadening, respectively, and L is the Fourier length:

$$L = \frac{n\lambda}{2(sin\theta_2 - sin\theta_1)}, \tag{2.7}$$

where n is an integer, λ is the wavelength of X-rays, and Θ_1 and Θ_2 are the endpoints of the angular range of the measured diffraction profile [96].

2.3.1 The Effect of Crystallite Size on X-ray Line Broadening

In order to understand the effect of crystallite (or diffraction domain) size on peak broadening, first we have to imagine the crystallites that give the intensity of the diffracted peak. Then, cut these crystallites into columns parallel to the diffraction vector. As the diffraction vector is lying perpendicular to the (*hkl*) lattice planes, the columns will be perpendicular to these too. Using the column length distribution density function *p(t)*, the Fourier transform of the *hkl* size profile is given as [84,91]:

$$A^S(L) = \frac{1}{\langle t \rangle} \int_L^\infty (t - L) p(t) dt, \tag{2.8}$$

where $<t>$ is an average column length obtained as the ratio of the total volume of the diffracted crystallites and their cross-section normal to the *hkl* diffraction vector, $p(t)dt$ represents the relative fraction of columns for which the length parallel to the *hkl* diffraction vector lies between t and $t+dt$. It is important to emphasize that the broadening of the intensity profile is influenced only by the size of the reflected crystallites, which is lying perpendicular to the (*hkl*) planes. The function $p(t)$ is expressed by the crystallite size distribution density function, $f(x)$, as:

$$p(t) = N \int_0^\infty h(t, x) f(x) dx, \tag{2.9}$$

where N is a normalization factor and $h(t,x)dt$ is the relative fraction of columns, having lengths between t and $t+dt$ in the crystallite with diameter x [88]. There are several possible distributions that can describe the size of the crystallites (Gaussian or normal, Lorentz, lognormal, etc.). During the evaluation of the profiles I assumed spherical crystallites with log-normal size distribution, therefore:

$$h(t, x) = \frac{2t}{x^2}, \tag{2.10}$$

for $t \leq x$ and $h(t,x)=0$ for $t > x$, and

$$f(x) = \frac{1}{\sqrt{2\pi}\sigma x} exp\left\{ - \frac{[ln(x/m]^2}{2\sigma^2} \right\}, \tag{2.11}$$

where m and σ^2 are the median and the log-normal variance of the crystallite size distribution, respectively [91].

If equations (2.10) and (2.11) are substituted into the formula (2.9), and then equation (2.9) into equation (2.8), the size Fourier transform is written as [86,92]:

$$A^S(L) = \frac{1}{2} erfc\left[\frac{ln(|L|/m)}{\sqrt{2}\sigma} - 1.5\sqrt{2}\sigma\right] -$$

$$-\frac{3}{4mexp(8.125\sigma^2)}|L| erfc\left[\frac{ln(|L|/m)}{\sqrt{2}\sigma} - \sqrt{2}\sigma\right] +$$

$$+\frac{3}{4m^3 exp(10.125\sigma^2)}|L|^3 erfc\left[\frac{ln(|L|/m)}{\sqrt{2}\sigma}\right], \quad (2.12)$$

where *erfc* is the complementary error function given as:

$$erfc(x) = \frac{2}{\sqrt{\pi}} \int_x^\infty exp(-t^2)\, dt. \quad (2.13)$$

Equation (2.12) shows that the Fourier coefficients depend only on the two parameters (m and σ) of the size distribution of spherical crystallites. It is important to note that the smaller the crystallite size, the broader the diffraction peak.

In this thesis, the average crystallite size is taken as the area-weighted mean crystallite size, $<x>_{area}$, which can be calculated from the parameters of the crystallite size distribution as follows:

$$\langle x \rangle_{area} = m\, exp(2.5\sigma^2). \quad (2.14)$$

2.3.2 The Strain Effect on X-ray Line Broadening

The Fourier transform of the "deformation" profiles (A^D) can be given by the following formula [99]:

$$A^D(g, L) = exp\left(-2\pi^2 L^2 g^2 \langle \varepsilon_{g,L}^2 \rangle\right), \quad (2.15)$$

where g is the length of the *hkl* diffraction vector, $\langle \varepsilon_{g,L}^2 \rangle$ is the mean-square strain normal to (*hkl*) lattice planes that depends on both g and L. For understanding the

meaning of the $\langle \varepsilon_{g,L}^2 \rangle$, first we have to imagine a perfect lattice (distortion free). Then, we take two atoms where the section between them is lying normal to the (*hkl*) lattice plane and has a length of *L*. Due to lattice distortions, the positions of these points are displaced. Therefore, the projection of the section connecting these two points normal to (*hkl*) lattice planes changes to *L'*. Then, the ratio (*L'*-*L*)/*L* gives the local strain normal to planes (*hkl*). Averaging the square of this quantity for the reflecting volume yields the value of $\langle \varepsilon_{g,L}^2 \rangle$. Equation (2.15) suggests that the strain broadening of *hkl* peak profile is determined by the lattice distortions normal to (*hkl*) lattice planes in the reflecting crystallites [90]. The larger the lattice distortion, the broader the diffraction peak.

The strain field of a point defect has a short-range character because the magnitude decreases with r^{-3}, where *r* is the distance from the defect, therefore it decays very quickly with increasing *r*. By contrast, the strain field of dislocations decreases with r^{-1}, so it has a long-range character. From the reciprocity between the crystal and reciprocal spaces it follows that the scattering related to point defects (Huang scattering) does not give a substantial contribution to the Bragg peak, while the strain caused by dislocations yields a measurable broadening of the diffraction peak. If the distortion is caused by dislocations, the mean-square strain has the following form [100]:

$$\langle \varepsilon_{g,L}^2 \rangle = \frac{b^2}{4\pi} \rho C_{hkl} f^* \left(\frac{L}{R_e} \right), \tag{2.16}$$

where ρ and b are the dislocation density and the magnitude of the Burgers vector, respectively, C_{hkl} is the contrast factor of dislocations and R_e is the effective outer cut-off radius of dislocations. The R_e shows how far the deformation field is negligible from the core of dislocation. If dislocations are arranged into dipoles or low-angle grain boundaries, they shield the deformation field of each other and the value of R_e is smaller. Instead of R_e, the screening of the strain field of dislocations is rather described by the dimensionless dislocation arrangement parameter *M* that can be calculated as [90]:

$$M = R_e \rho^{1/2}. \tag{2.17}$$

The stronger the screening of the strain fields of dislocation, the smaller the value of *M*.

Dislocations have an anisotropic strain field, which causes anisotropic strain broadening of the diffraction profiles. This means that the line broadening has a strong dependence on the relative orientation of the diffraction vector, and the line and Burgers vectors of dislocations as well as the normal vector of the slip plane. Thus, the same dislocation structure causes different line broadening for the different *hkl* reflections. This is called strain anisotropy [101], and is taken into account by the contrast factor C_{hkl} in equation (2.16). In this thesis only cubic and orthorhombic materials are investigated, therefore the contrast factors are given only for these two crystal systems. In the case of a texture-free cubic polycrystal sample or if the different slip systems are equally populated by dislocations, the C_{hkl} factors can be averaged for the permutations of the *hkl* indices [102]. Then, the average contrast factor for cubic materials can be expressed as:

$$\overline{C}_{hkl} = \overline{C}_{h00}(1-qH^2), \tag{2.18}$$

where

$$H^2 = \frac{h^2k^2 + h^2l^2 + k^2l^2}{(h^2 + k^2 + l^2)^2}, \tag{2.19}$$

and q describes the edge/screw character of dislocations. $\overline{C}_{h00}$ is the contrast factor for reflection *h00*. The value of $\overline{C}_{h00}$ and q can be calculated on the basis of the dislocation crystallography and the elastic constants of the material. The contrast factors can be determined by the software ANIZC [103]. The theoretical values of parameter q for pure edge and screw dislocations are determined by the elastic constants and the dislocation slip systems activated in the crystal [104]. For orthorhombic crystals the average contrast factors can be expressed as [90,105]:

$$\overline{C}_{hkl} = \overline{C}_{h00}\left(H_0^2 + a_1H_1^2 + a_2H_2^2 + a_3H_3^2 + a_4H_4^2 + a_5H_5^2\right), \tag{2.20}$$

where

$$H_0^2 = \frac{h^4}{a^4\left(\frac{h^2}{a^2}+\frac{k^2}{b^2}+\frac{l^2}{c^2}\right)^2},$$

$$H_1^2 = \frac{k^4}{b^4\left(\frac{h^2}{a^2}+\frac{k^2}{b^2}+\frac{l^2}{c^2}\right)^2},$$

$$H_2^2 = \frac{l^4}{c^4\left(\frac{h^2}{a^2}+\frac{k^2}{b^2}+\frac{l^2}{c^2}\right)^2},$$

$$H_3^2 = \frac{h^2k^2}{a^2b^2\left(\frac{h^2}{a^2}+\frac{k^2}{b^2}+\frac{l^2}{c^2}\right)^2},$$

$$H_4^2 = \frac{h^2l^2}{a^2c^2\left(\frac{h^2}{a^2}+\frac{k^2}{b^2}+\frac{l^2}{c^2}\right)^2},$$

$$H_5^2 = \frac{k^2l^2}{b^2c^2\left(\frac{h^2}{a^2}+\frac{k^2}{b^2}+\frac{l^2}{c^2}\right)^2},$$

where a, b and c are the lattice constants, and a_1, a_2, a_3, a_4 and a_5 depend on the populated slip systems of dislocations and the anisotropic elastic constants of the crystal.

It should be noted that the strain anisotropy can be visualized in the Williamson-Hall plot [106]. In this method, the integral breadth (IB) or the full width at half maximum (FWHM) is plotted as a function of the modulus of the diffraction vector, g. This procedure enables the determination of the volume weighted average domain size and the microstrain [100,101].

2.3.3 The Effect of Planar Faults on X-ray Line Broadening

In addition to the finite crystallite size and dislocations, planar faults also cause diffraction peak broadening. Planar faults are two-dimensional lattice defects in crystalline materials. Stacking faults and twin boundaries are often formed in crystals either due to plastic deformation or during recrystallization of severely strained microstructures. Deformation twinning is a common and important phenomenon in alloys [109]. X-ray line profile analysis is an effective method in the study of stacking and twin faults in fcc and hcp materials due to the large probed volume. The intensity profile caused by plane defects (I_{hkl}^{PF}) can be written as [85,103]:

$$I_{hkl}^{PF}(g) = w_{\delta} I_{hkl}^{\delta}(g) + \sum_{j=1}^{N} w_j I_{hkl}^{j}(g), \qquad (2.21)$$

where I_{hkl}^{δ} is the Dirac-delta component of the profile at the exact Bragg position and $I_{hkl}^{j}$are the profile functions of the broadened sub-reflections, and w_{δ} and w_j are the fractions of the different sub-reflection components. The fractions are given by relative multiplicities of sub-reflection within reflection hkl [111].

2.3.4 X-ray Diffraction Experimental Setup and Evaluation

The X-ray line profiles were measured by high-resolution rotating anode diffractometers using Cu$K\alpha_1$ (wavelength, $\lambda = 0.15406$ nm) and Co$K\alpha_1$ (wavelength, $\lambda = 0.1789$ nm) radiations. The selection of the radiation wavelength depended on the chemical composition of the examined HEAs (TiZrHfNbTa and CoCrFeMnNi). Cu is the most widely used anode material, but for alloys containing Fe, Cr and Mn the high inelastic scattering reduces the peak intensity. For these materials, Co radiation with less inelastic scattering was used instead of Cu. In general, in the selection of X-

ray wavelengths for a diffraction experiment, it is important to avoid that the studied material contains chemical elements for which the absorption edges are located just above the used characteristic wavelength. For example, the K-absorption edge of Co is at 1.61 A. The $K\alpha_1$ spectral line of copper has a wavelength of about 1.54 A. Hence, the $K\alpha_1$ characteristic Cu radiation will be absorbed by Co, and a Cu X-ray tube is not suitable for X-ray line profile analysis of Co-based materials [112].

The measurement layout is shown in Fig. 2.2. One advantage of the devices used in my studies compared to conventional radiation sources is that the width of the instrumental profile is small, which increases the upper and lower limits of the diffraction domain size and dislocation density measurements, respectively. The small instrumental broadening was achieved by producing a narrow parallel beam. Due to the narrow cross-section of the beam, it is necessary to increase its brilliance which was achieved by applying a rotating anode X-ray source. Another advantage of the layout is its high resolution, which is due to the fact that the sample-detector distance can be increased up to 1 m. The high resolution is important to have enough points in the line profile. It is worth to note that one measurement took one or two days, depending on the sample-detector distance.

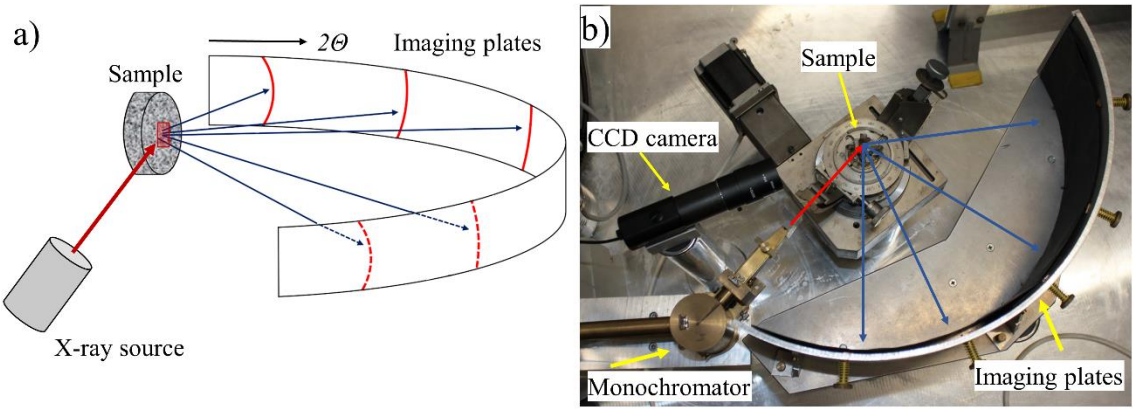

Fig. 2.2: Schematic of the X-ray diffraction geometry (a) and a photo of the device used in my experiments (b). The red arrow shows the primary beam and the dark blue arrows show the diffracted beams.

For the measurements, parallel and monochromatic beams were used. The diffracted intensity was detected by imaging plate (IP) detectors. Two-dimensional IPs detected the Debye–Scherrer diffraction rings. The line profiles were determined as the intensity distribution perpendicular to the rings obtained by integrating the two-dimensional intensity distribution along the rings (see Fig. 2.3).

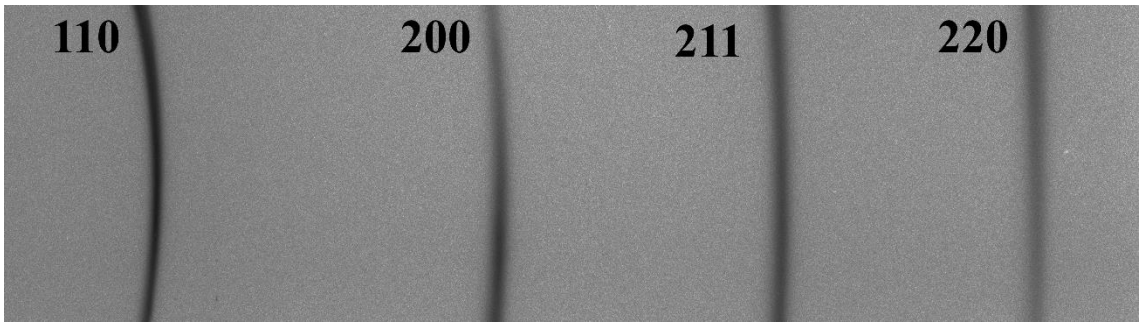

Fig. 2.3: Typical homogeneous intensity distribution in the Debye–Scherrer rings detected on an imaging plate.

The diffraction profiles were evaluated by the Convolutional Multiple Whole Profile (CMWP) fitting method [113]. In this method, the diffraction pattern is fitted by the sum of a background spline and the convolution of the instrumental pattern and the theoretical line profiles. The area-weighted mean diffraction domain size ($\langle x \rangle_{area}$), the dislocation density (ρ) and the twin fault probability (β) were determined from the CMWP fitting method. In fcc crystals the mean twin-fault spacing (d_{twin}) can be obtained from the twin fault probability (β) as:

$$d_{twin} = 100 \cdot \frac{d_{111}}{\beta} \tag{2.22}$$

where d_{111} is the distance between the neighboring $\{111\}$ planes. The $\langle x \rangle_{area}$ was calculated from the median (m) and the log-normal variance (σ^2) of the diffraction domain size distribution as shown in the equation (2.14). The twin fault probability in fcc materials is defined as the relative fraction of twin boundaries among the $\{111\}$ lattice planes. The edge/screw character of dislocation can be obtained from parameter q experimentally determined by XLPA. The comparison of the experimental q value obtained from XLPA with the theoretical values for pure edge and screw dislocations allows the determination of edge/screw character of

dislocations. If the experimental q value is close to the arithmetic average of the theoretical values for pure edge and screw dislocations, the dislocation structure has a mixed character. If the experimental q value is higher or lower than the theoretical average, then the type of dislocations can be considered as rather screw or rather edge, respectively.

2.3.5 Lattice Parameter Determination from X-ray Diffraction

If the studied sample has a cubic structure and the reflections are indexed, we can determine the lattice parameter from the values of interplanar spacing d_{hkl} using the following formula: $a = d_{hkl}\sqrt{h^2 + k^2 + l^2}$. This calculation can be carried out for any reflexion, but the experience shows that the lattice parameter values obtained from the different peaks are slightly different. This difference is caused by the error of the interplanar spacing due to the uncertainty of the Bragg-angle. This systematic error decreases with increasing the Bragg-angle, therefore it is reasonable to use the reflections having high 2Θ to determine the lattice parameter. However, due to the angle dependence of the atomic scattering factor, as 2Θ increases the intensity decreases, and the reflections with high 2Θ are usually noisy.

To overcome these problems, the lattice parameter is determined by extrapolating the d_{hkl} values to $\Theta = 90°$ using the following formula (Nelson–Riley method) [114]:

$$a_{hkl} = a_0 - D\cos\theta\left(ctg\theta + \frac{\cos\theta}{\theta}\right), \tag{2.23}$$

where D is a constant depending on the different systematic errors. In this analysis, the values of a_{hkl} are plotted as a function of $\cos\theta\left(ctg\theta + \frac{\cos\theta}{\theta}\right)$. The intersection of the straight line fitted to the data points with the vertical axis gives the lattice parameter a_0.

2.4 Electron Microscopy Techniques

2.4.1 Scanning Electron Microscopy

The microstructure was investigated by an FEI Quanta 3D scanning electron microscope (SEM), including energy-dispersive X-ray spectroscopy (EDS) and electron backscatter diffraction (EBSD). Before the EBSD investigation, the surface was mechanically polished with 1200, 2500 and 4000 grit SiC abrasive papers, and then the polishing was continued with a colloidal silica suspension (OP-S) with a particle size of 40 nm. Finally, the surface was electropolished at 25 V and 1 A, using an electrolyte with a composition of 70% ethanol, 20% glycerine and 10% perchloric acid (in vol. %) for the CoCrFeMnNi HEA or etched with HF/H_2O (1:3) solution for the TiZrHfNbTa at room temperature.

EDS was used for the elemental analysis. The EDS technique detects X-rays emitted from the sample during the bombardment by an electron beam and gives the elemental composition of the investigated volume. In Fig. 2.4, a typical EDS spectrum is presented.

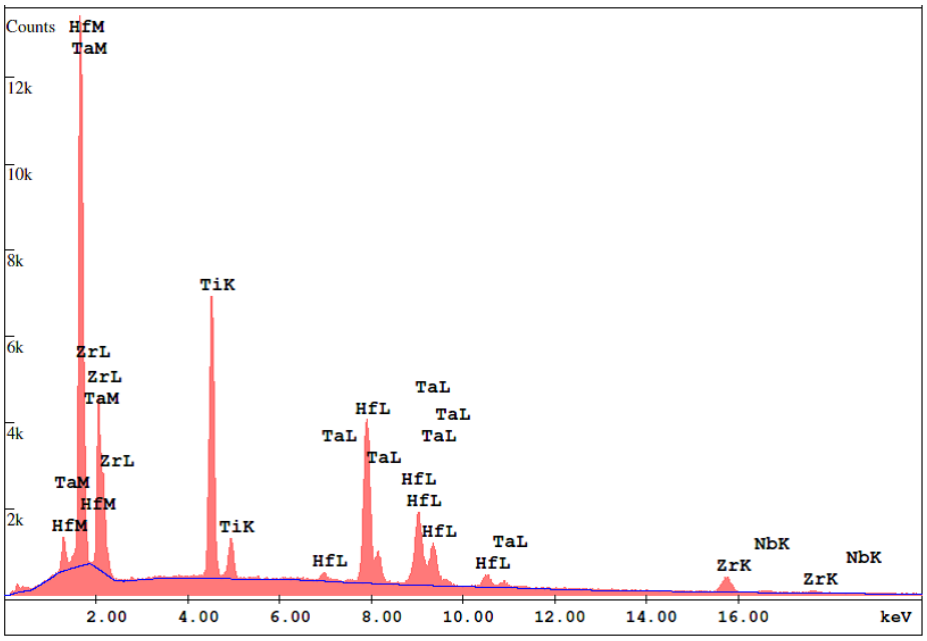

Fig. 2.4: Typical EDS spectrum of the $Ti_{20}Zr_{20}Hf_{20}Nb_{20}Ta_{20}$ HEA.

In the severely deformed samples, the microstructure was strongly refined and distorted, therefore EBSD was not able to study the grain structure. Thus, transmission electron microscopy (TEM) investigations were applied.

2.4.2 Transmission Electron Microscopy

TEM investigations were applied for the determination of the grain size on the severely deformed HEA samples. The TEM foils were thinned first by mechanical grinding to a thickness of 50 μm, and then they were ion milled using an Ar ion beam at an inclination angle of 5° until perforation. The ion milling was conducted at 7 keV and 2 mA with continuous cooling of the sample by liquid nitrogen. The TEM images were taken using a Philips CM-20 transmission electron microscope, operating at 200 kV. The twin faults inside the nanocrystals were studied with a higher magnification, using a JEOL-3010 transmission electron microscope, operating at 300 kV. The TEM pictures were detected by a GATAN Orius CCD camera, using Digital Micrograph software.

2.5 Mechanical Tests

2.5.1 Vickers Microhardness Testing

The microhardness of the samples was measured using a Zwick Roell ZHμ Vickers indenter with an applied load of 500 g and a dwell time of 10 s. The size of the indents was measured by optical microscopy (see Fig. 2.5). The Vickers hardness number (HV) can be obtained by the following expression:

$$HV = \frac{F}{A} \approx \frac{1.8544F}{d^2}, \tag{2.20}$$

where F is the load, A is the area of the indent and d is the average length of the diagonal of the square-shaped indentation pattern.

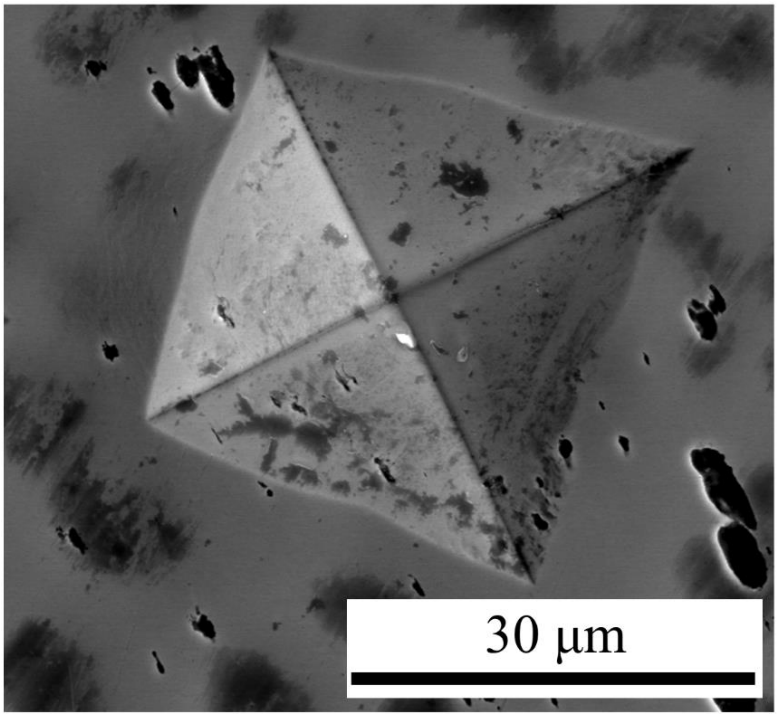

Fig. 2.5: Vickers indentation for $Co_{20}Cr_{20}Fe_{20}Mn_{20}Ni_{20}$ HEA disk processed by 1 turn of HPT.

2.5.2 Nanoindentation Testing

Depth-sensing indentation became a widely used technique for the mechanical characterization of materials [108,109]. In my work, this method was used for the determination of the anisotropic elastic constants of $Ti_{20}Zr_{20}Hf_{20}Nb_{20}Ta_{20}$ HEA in order to calculate the dislocation contrast factors for the CMWP evaluation of X-ray diffraction profiles. To determine the elastic moduli, nanoindentation measurements were carried out on the initial sample, using an UMIS nanoindentation device with a Berkovich indenter, and applying a maximum load of 100 mN. The computer-controlled measuring equipment used a constant loading rate. Fig. 2.6a shows nanohardness indents on the surface of the initial $Ti_{20}Zr_{20}Hf_{20}Nb_{20}Ta_{20}$ sample with the distance of 100 μm between the neighboring

indents. During the measurement, the machine continuously measures the load as a function of the indentation depth (see Fig. 2.6b). For more details on the method, see section 3.1.3.

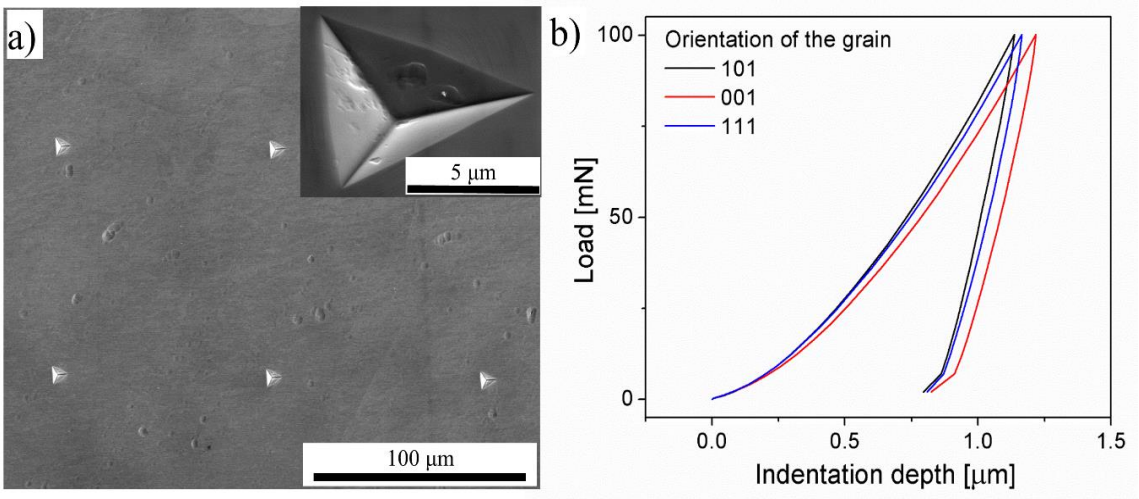

Fig. 2.6: a) SEM image of nanohardness indents taken on the initial coarse-grained $Ti_{20}Zr_{20}Hf_{20}Nb_{20}Ta_{20}$ sample. b) Load-indentation depth curves obtained for grains with different crystallographic orientations. The numbers indicate the Miller indices of the lattice planes parallel to the surface.

2.5.3 Uniaxial Compression Test

Compression tests were carried out on the $Ti_{20}Zr_{20}Hf_{20}Nb_{20}Ta_{20}$ HEA at room temperature at a strain rate of 1.5×10^{-3} s^{-1} using cylindrical specimens with 5 mm in diameter and 7 mm in length. The compression test was carried out using a 100 kN MTS testing machine (20/MH). In order to study the microstructure evolution during compression, samples were deformed up to different plastic strain values between 2 and 20%.

The dynamic mechanical properties of the $Ti_{20}Zr_{20}Hf_{20}Nb_{20}Ta_{20}$ HEA were investigated using direct impact Hopkinson pressure bar (DIHPB) technique. The schematic diagram of the DIHPB is shown in Fig. 2.7. The equipment consists of an incident and a transmitted bar. A strain gage is placed on the Hopkinson bar in order

to provide the loading history of the specimen [117]. DIHPB setup was used to generate plastic deformation at higher strain rates up to ~$3.4 \times 10^3\ s^{-1}$ (initial strain rate)[118]. In the DIHPB technique, originally introduced by Dharan [119], a specimen placed against a Hopkinson pressure bar was impacted by a striker moving at a constant velocity. The striker speed, V_i, typically between 5 and 100 m/s, was recorded using two laser beams separated by 18 mm and positioned 30 mm prior to the impact. Both the striker and the Hopkinson bar are made of tungsten alloy with 20 mm in diameter, 17.5 g cm^{-3} in density and 1500 MPa in yield strength. In our measurements, the impact velocities of 3.7, 6.14 and 10 m/s were applied on the $Ti_{20}Zr_{20}Hf_{20}Nb_{20}Ta_{20}$ HEA.

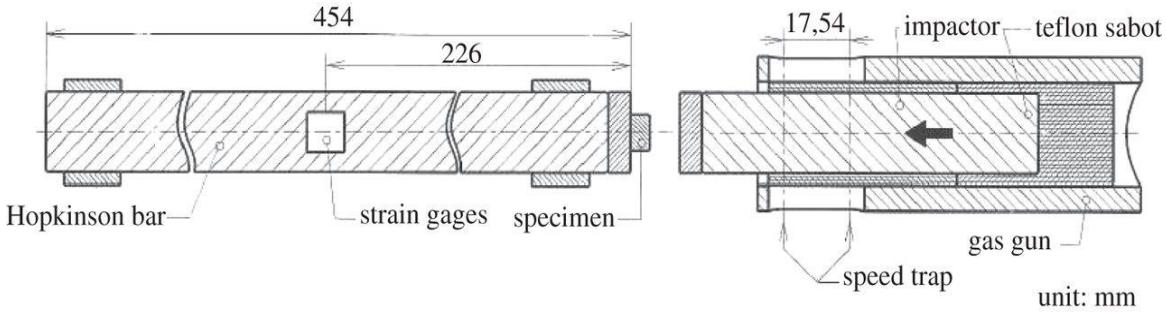

Fig. 2.7: A schematic diagram of the direct impact Hopkinson pressure bar technique [117].

A complementary compression test was carried out on the initial $Ti_{35}Zr_{27.5}Hf_{27.5}Nb_5Ta_5$ HEA material to study the deformation-induced phase transformation at room temperature and a strain rate of ~$10^{-3}\ s^{-1}$ up to a strain of ~11.5% using an MTS universal mechanical testing machine. The studied specimens have dimensions of 3 mm×3 mm×5 mm.

2.5.4 Micropillar Compression Test

The local mechanical properties were investigated by micropillar compression tests for the nanocrystalline $Co_{20}Cr_{20}Fe_{20}Mn_{20}Ni_{20}$ HEA. Micropillar compression is an excellent technique to characterize the plastic properties at small scales [113–115]. In our investigations, micropillars were fabricated in the regions with different chemical compositions by focused ion beam (FIB) installed on Quanta FEI 3D SEM. The compression experiments were carried out by a home-made indenter device using a flat-ended cylindrical punch. A schematic of the device is shown in Fig. 2.8. The sample movement in directions *x* and *y* is controlled by two linear ultrasonic motors. In the *z*-direction, two stages are used (a fine and a coarse as shown in Fig. 2.8). One is a linear step-motor stage for coarse movement which used to move the compressing tip closer to the sample. The second stage for fine movement, mounted on the linear step-motor stage, is a piezoelectric positioning stage with a resolution of ~0.1 nm. It is important to note that during the compression test, only this stage is moved. A spring is used to measure the external force. The elongation of the spring is measured by a capacitive sensor with 0.1 nm resolution [123].

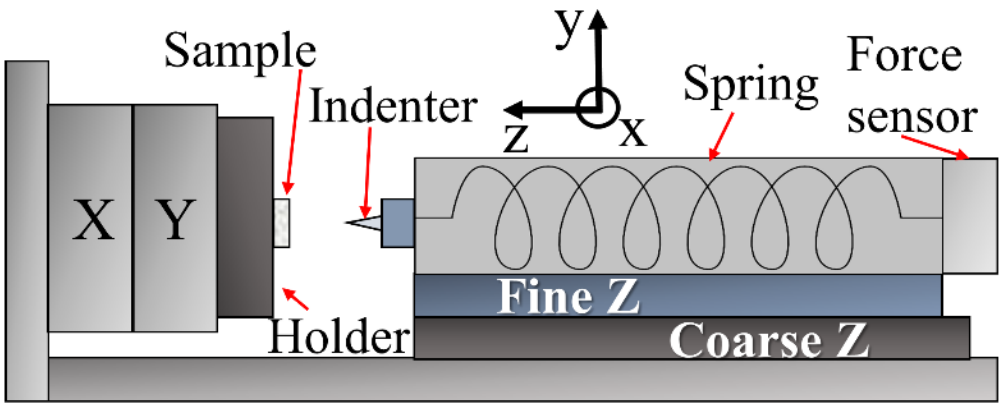

Fig. 2.8: Schematic of the *in-situ* compression device.

To ensure the reproducibility of the micro-compression data, at least three micropillars were fabricated and compressed in each characteristic region. Before the micropillar fabrication by FIB, an amorphous Pt layer with a thickness of 100 nm was deposited on the surface of the $Co_{20}Cr_{20}Fe_{20}Mn_{20}Ni_{20}$ HEA specimen.

Micropillars with square cross-sections were fabricated, and the width and the height of the pillars were 1 and 2 μm, respectively (see Fig.2.9).

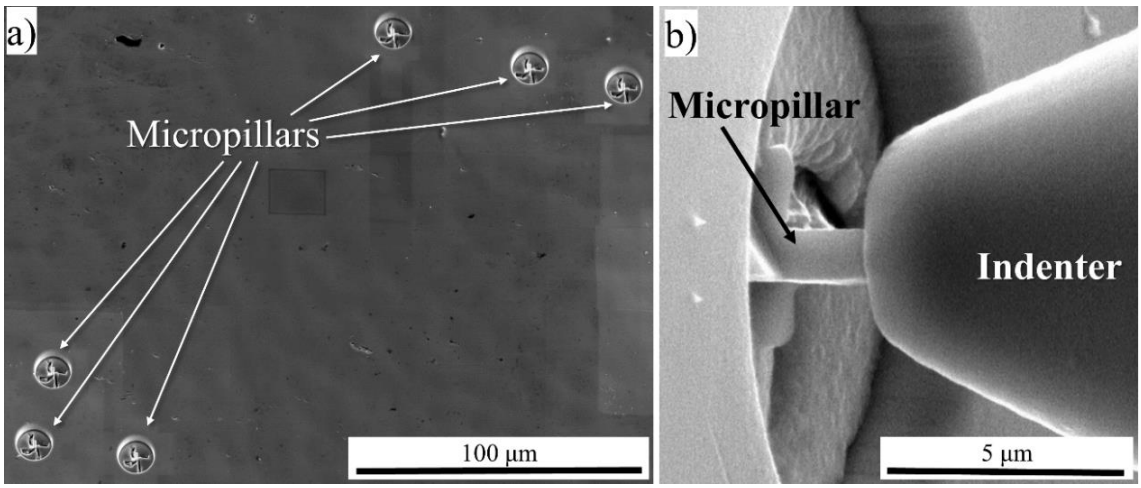

Fig. 2.9: a) SEM backscattered electron image of the micropillars, and b) a frame taken from a video recorded by SEM during the compression test of a micropillar for the $Co_{20}Cr_{20}Fe_{20}Mn_{20}Ni_{20}$ HEA disk processed by 2 turns of HPT.

3 Results and Discussion

3.1 Microstructure and Mechanical Behavior of Refractory $Ti_{20}Zr_{20}Hf_{20}Nb_{20}Ta_{20}$ High-entropy Alloy [R1, R2]

In this chapter, the microstructure and the mechanical behavior of an equimolar $Ti_{20}Zr_{20}Hf_{20}Nb_{20}Ta_{20}$ HEA are studied. The initial HEA material was compressed at room temperature for the strain of 3, 10 and 20%. Additionally, two samples were impacted using a Hopkinson pressure bar at the initial impact velocities of 10 and 20 m/s up to the equivalent strains of 50 % and 130 %, respectively. The microstructure evolution in this HEA during compression test was studied by XLPA and electron microscopy (TEM, SEM). The elastic anisotropy factor required for the XLPA evaluation was determined by nanoindentation.

3.1.1 As-cast Microstructure and Mechanical Behavior

A refractory HEA with equiatomic composition ($Ti_{20}Zr_{20}Hf_{20}Nb_{20}Ta_{20}$) was processed by arc melting and induction processes under argon atmosphere. Two master alloys, Nb–Ta and Ti–Zr–Hf, were first melted from high purity metals (exceeding 99.9% purity) in the form of slugs and wires. Both alloys were remelted twice in order to improve the homogeneity, and then were mixed together. A titanium getter was used prior to each arc-melting fusion in order to capture the residual oxygen in the chamber. Homogenization of the alloy was then assessed by high-frequency induction melting in the sectorized cooled copper crucible under helium atmosphere. Finally, the homogenized refractory alloy was obtained by arc

melting in the form of an ingot with 60 mm in length and approximately 10 mm in diameter.

Fig. 3.1 is a typical orientation map for the initial undeformed microstructure. There is no preferred crystallographic orientation of the grains. The grain shape is irregular and the grain size distribution is broad, ranging between 10 and 350 μm with an average value of ~200 μm.

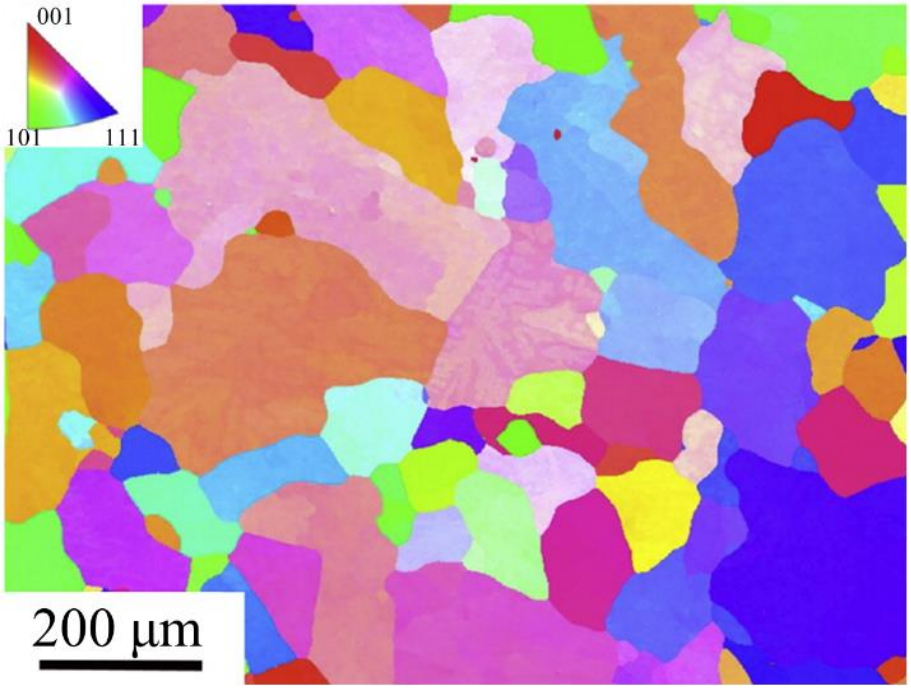

Fig. 3.1: EBSD orientation map showing the microstructure in the initial $Ti_{20}Zr_{20}Hf_{20}Nb_{20}Ta_{20}$ sample (The picture was taken at University of Paris 13).

Fig. 3.2 shows a true stress versus the true strain curve obtained by compression for the as-processed HEA. Compression tests were carried out at room temperature at a strain rate of 1.5×10^{-3} s^{-1} on a cylindrical specimen with 5 mm in diameter and 7 mm in length. The yield strength was about 890 MPa. The bcc-structured HEAs usually have very high yield strength [5]. For instance, $Nb_{25}Mo_{25}Ta_{25}W_{25}$ and $V_{20}Nb_{20}Mo_{20}Ta_{20}$ refractory HEAs have yield strength values of about ~1000 MPa and ~1200 MPa, respectively [27].

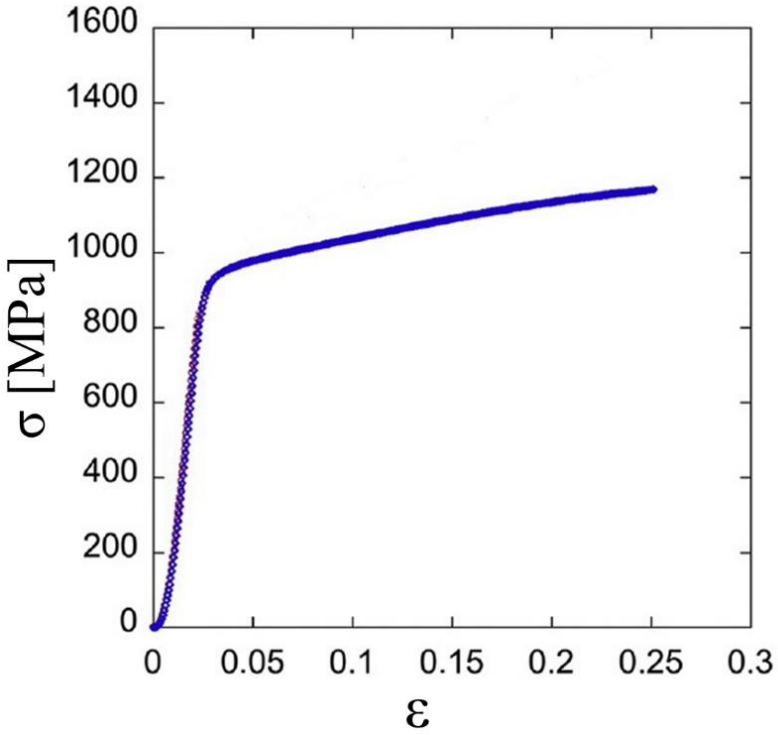

Fig. 3.2: True stress vs. true strain plots of the as-processed $Ti_{20}Zr_{20}Hf_{20}Nb_{20}Ta_{20}$ HEA during room temperature compression at a strain rate of 1.5×10^{-3} s^{-1}.

3.1.2 Microstructure of the Compressed Samples from X-ray Line Profile Analysis

The initial $Ti_{20}Zr_{20}Hf_{20}Nb_{20}Ta_{20}$ HEA material was compressed at room temperature up to the plastic strains of 3, 10 and 20%. Additionally, two samples were impacted using Hopkinson pressure bar technique at the initial impact velocities of 10 and 20 m/s up to the equivalent strains of 50 % and 130 %, respectively.

The average lattice parameter was determined by the Nelson–Riley method [114]. The microstructure of the specimens was studied by XLPA. It should be noted that the Debye-Scherrer diffraction rings were fragmented into spots with slightly different diffraction angles. As an example, Fig. 3.3 shows the Debye-Scherrer ring of reflection *211* for the sample compressed up to the strain of 20%.

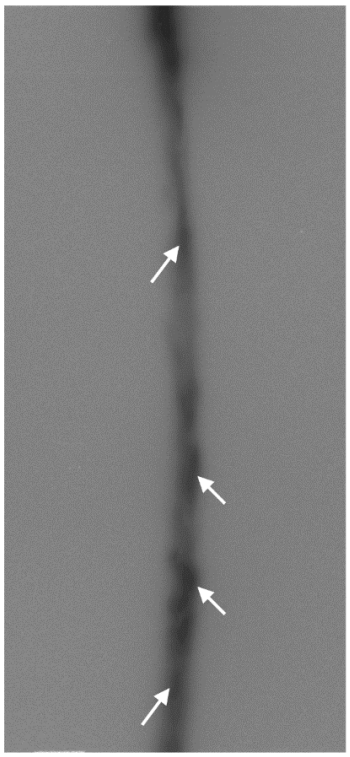

Fig. 3.3: The Debye-Scherrer ring of reflection *211* for the $Ti_{20}Zr_{20}Hf_{20}Nb_{20}Ta_{20}$ sample compressed up to 20%. The white arrows show some diffraction spots reflected by individual grains.

The variation of the 2Θ values (i.e., the horizontal position) of the high intensity spots in the ring is most probably caused by the slightly different chemical composition in the various reflecting grains, resulting in a variation of the lattice parameter. The peak breadths determined from the different spots along a Debye-Scherrer ring were very close to each other, therefore the peak with the lowest noise was selected from each ring. These individual line profiles were put together into a single diffraction pattern and evaluated by the CMWP analysis [87,106]. As an example, Fig. 3.4 shows the fitting for the sample compressed up to 20%. Reflection *222* was omitted from the pattern due to its weak intensity.

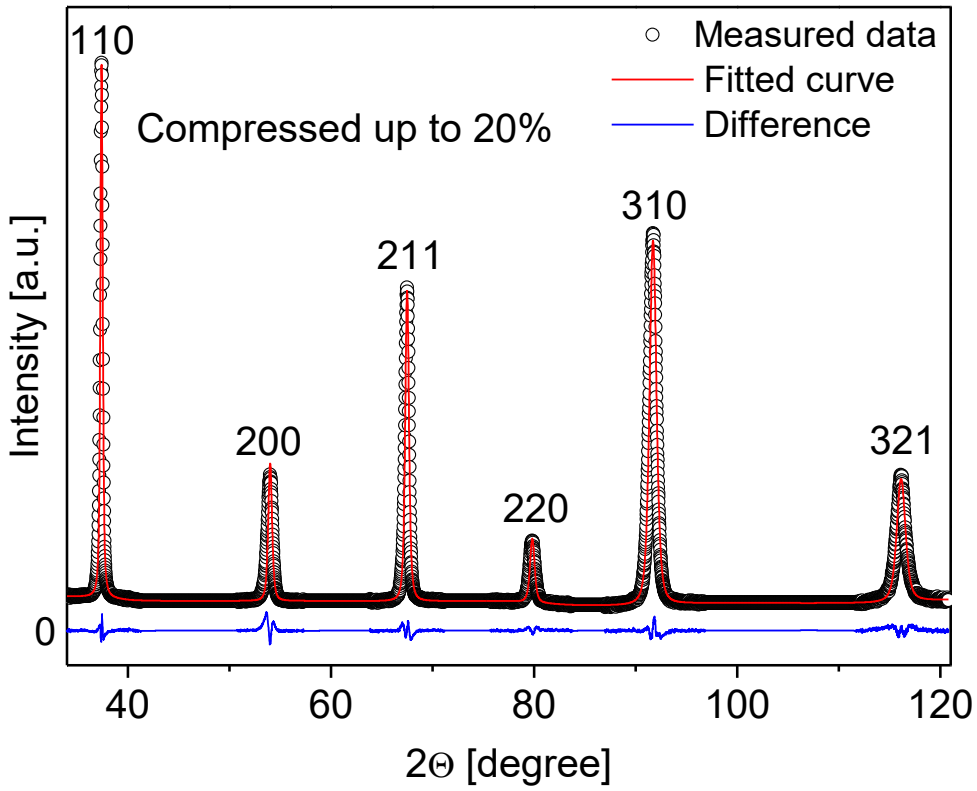

Fig. 3.4: The CMWP fitting for the sample compressed up to the strain of 20%.

The initial and the deformed samples have a bcc structure with a lattice constant of 0.3405±0.0008 nm. This value is in good agreement with the lattice constant calculated for this alloy in Ref. [124]. For the compressed samples, the lattice parameter remains unchanged within the experimental error. EDS analysis was performed on 1 mm x 1 mm surface area of the initial sample. The analysis revealed that the elemental fractions deviate slightly from the equimolar chemical composition Namely, the atomic concentrations for Ti, Zr, Hf, Nb, and Ta are 18.2 ± 1.8, 19.7 ± 2.0, 19.2 ± 1.9, 22.3 ± 2.2 and 20.6 ± 2.1 at.%, respectively. This is in a good agreement with the study presented in [125] where the chemical difference was investigated between the interdendritic and dendritic structures by coupled energy and wavelength dispersive spectrometry (EDS/WDS).

The average diffraction domain size and dislocation density were determined by XLPA in samples compressed up to true plastic strains of 3, 10 and

20%. As an example, Fig. 3.4 shows the X-ray diffraction pattern for the sample compressed up to 20%. Reflection *222* was omitted from the pattern due to its weak intensity. The dependence of the peak breadths on the diffraction order (i.e., on the indices *hkl*) can be visualized by plotting the full width at half maximum (FWHM) as a function of the modulus of the diffraction vector, g (classical Williamson–Hall plot) [108]. FWHM and g can be calculated as:

$$FWHM = \frac{\Delta(2\Theta)\cos\Theta}{\lambda} \text{ and } g = \frac{2\sin\Theta}{\lambda} \tag{3.1}$$

where Θ is the Bragg angle of the peak, $\Delta(2\Theta)$ is the breadth of the line profiles in radians and λ is the wavelength of X-rays. The classical Williamson–Hall plot for the sample compressed up to 20% is shown in Fig. 3.5a. The non-monotonous variation of FWHM as a function of g for plastically deformed metallic materials is usually caused by the anisotropic strain field of dislocations, and this phenomenon is referred to as strain anisotropy [108]. The contrast effect of dislocations on the line broadening can be taken into account by the average contrast (or orientation) factor of dislocations. Therefore, for a dislocated polycrystalline cubic material the FWHM values fit to a smooth curve, when they are plotted as a function of $g^2\overline{C}_{hkl}$, where $\overline{C}_{hkl}$ is the average contrast factor given as (modified Williamson-Hall plot):

$$\overline{C}_{hkl} = \overline{C}_{h00}\left(1 - q\frac{h^2k^2 + k^2l^2 + h^2l^2}{\left(h^2 + k^2 + l^2\right)^2}\right). \tag{3.2}$$

Figures 3.5a and b show the classical and the modified Williamson-Hall plots for the sample compressed up to 20%. The datum points follow a smooth curve, if q=2.4 is selected.

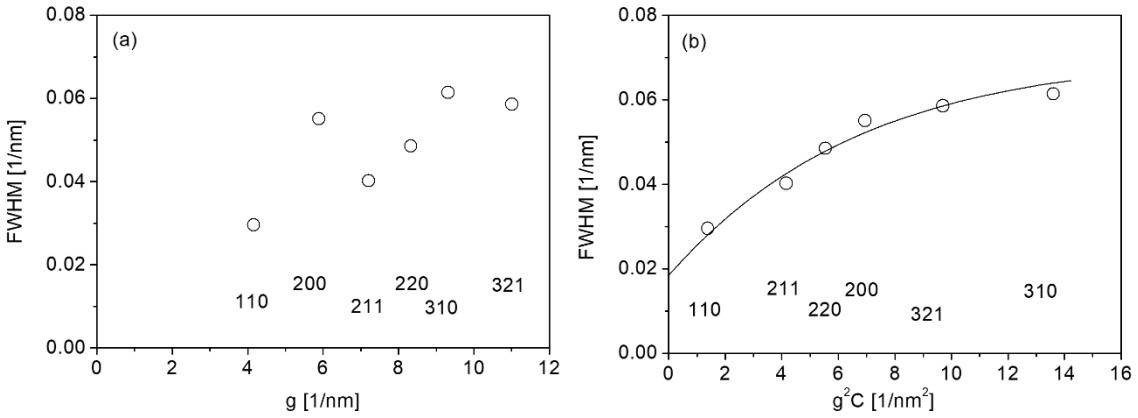

Fig. 3.5: The classical (a) and the modified (b) Williamson-Hall plots for the sample compressed up to 20%.

It is noted that the fitting of the measured diffraction pattern by the CMWP procedure also gives the value of q, which was the same within the experimental error as the value obtained by the modified Williamson–Hall plot. The values of q for all deformed samples determined by CMWP fitting are listed in Table 3.1.

Table 3.1: The average lattice constant and the parameters of the microstructure obtained by XLPA. $\langle x \rangle_{area}$ is the area-weighted mean diffraction domain size, ρ is the dislocation density and q is a parameter describing the edge/screw character of dislocations.

Sample	$\langle x \rangle_{area}$ [nm]	ρ [10^{14} m^{-2}]	q
Initial	–	–	–
compressed, 3%	151 ± 16	2.0 ± 0.6	1.0 ± 0.1
compressed, 10%	123 ± 14	10 ± 2	2.1 ± 0.1
compressed, 20%	39 ± 5	15 ± 2	2.4 ± 0.1
impacted, 10 m/s, center	43 ± 6	47 ± 7	2.3 ± 0.1
impacted, 20 m/s, center	36 ± 5	32 ± 5	2.7 ± 0.1

3.1.3 Evaluation of the Edge/Screw Character of Dislocations

The comparison of the experimentally obtained q with the theoretical values calculated for pure edge and screw dislocations enables the determination of the edge/screw character of the dislocation structure. The theoretical values of q for pure edge and screw dislocations depend on the anisotropic elastic constants of the studied material. The dependence of parameter q on the elastic constants for bcc polycrystals can be given using the ratio of the elastic constant c_{12}/c_{44} and the elastic anisotropy factor ($A = \frac{2c_{44}}{c_{11} - c_{12}}$) [126]. Fig. 3.6 shows parameter q for edge and screw dislocations in bcc crystals as a function of A for three different usual values of c_{12}/c_{44} (0.5, 1 and 2). The data were taken from Ref. [108].

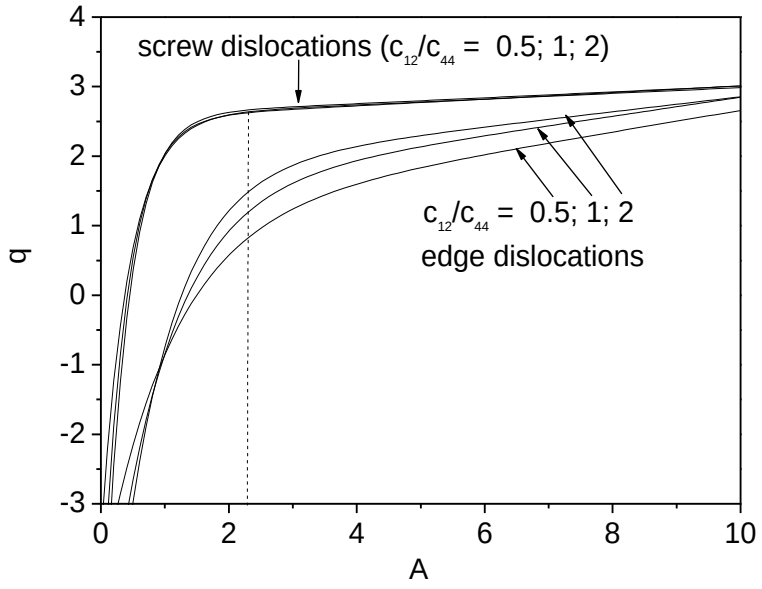

Fig. 3.6: The variation of parameter q for edge and screw dislocations in bcc crystals as a function of A for three different usual values of c_{12}/c_{44}.

As the single crystal anisotropic elastic constants are not known for the present HEA material, therefore the exact value of parameter q for pure edge and screw dislocations cannot be determined. However, depth-sensing indentation technique

may provide the anisotropy factor, as described in the next section. Then, this factor may be used to estimate the edge/screw character of dislocations from the experimental value of parameter q. In addition, in the CMWP evaluation of the diffraction patterns one fitting parameter is $\overline{C}_{h00}\, b^2\rho$, where b is the modulus of the Burgers vector of dislocations. Assuming the usual Burgers vector in bcc structures (a/2<111>{110}), b equals 0.2944 nm in the present HEA material. Since $\overline{C}_{h00}$ depends on the anisotropic elastic constants, without the knowledge of their values the dislocation density cannot be determined.

For a polycrystalline material, the single crystal elastic anisotropy factor can be determined by depth-sensing indentation technique, as shown by Vlassak and Nix [127]. Then, this factor may be used for the estimation of the edge/screw character of dislocations from the experimental value of parameter q and for the determination of the dislocation density from CMWP fitting. The analysis of the load-penetration depth curve obtained by depth-sensing indentation provides the indentation modulus of the material defined as:

$$M = \frac{E}{1-\nu^2}\,, \tag{3.3}$$

where E and ν are the Young's modulus and the Poisson's ratio of the material. If the size of the indentation is much smaller than the grain size, the value of M depends on the orientation of the indented grain due to the elastic anisotropy of the crystal. Vlassak and Nix [127] showed that the indentation modulus M_{hkl} measured on the (hkl) surface by a Berkovich indenter can be expressed as the product of the isotropic indentation modulus, M_{iso}, a correction factor β_{hkl} due to the elastic anisotropy, and another factor α_{hkl} owing to the anisotropic (triangular) shape of the Berkovich punch:

$$M_{hkl} = \alpha_{hkl}\beta_{hkl}M_{iso}\,, \tag{3.4}$$

where M_{iso} is the indentation modulus measured on a randomly oriented, polycrystalline aggregate consisting of small crystals, which are much smaller than the indent (i.e., this is the average indentation modulus). The dependence of factor

α_{hkl} on the orientation of the triangular indent on the surfaces (001), (101) and (111) is plotted in Fig. 3.8 of Ref. [127]. For the surface (001), this factor equals 1.058 independently of the indent orientation. For surfaces (101) and (111), the value of factor α_{hkl} varies with the angle between one of the sides of the indenter and directions $[10\bar{1}]$ and $[11\bar{2}]$, respectively. In the presented experiments α_{101} and α_{111} are 1.057 and 1.051, respectively.

For grains with cubic crystal structure, the correction factor β_{hkl} is a function of the Poisson's ratio in the cube directions (ν_{100}) and the anisotropy factor (A) [127]. Thus, β_{hkl} can be given by the following formula:

$$\beta_{hkl} = a + c\left(A - A_0\right)^B, \tag{3.5}$$

where a, c, A_0 and B depend on ν_{100}. The parameters in eq. (3.5) for β_{001}, β_{101} and β_{111} are listed in Table 3.1 of Ref. [127] for six different values of ν_{100}, namely for 0.2, 0.25, 0.3, 0.35, 0.4 and 0.45. Due to the very large average grain size of the present HEA material (several hundreds of microns as shown in the EBSD image of Fig. 3.7), M_{iso} cannot be determined. However, M_{iso} can be eliminated by expressing the ratios of M_{001}, M_{101} and M_{111} using equation (3.4):

$$\frac{M_{001}}{M_{101}} = \frac{\alpha_{001}\beta_{001}}{\alpha_{101}\beta_{101}} \text{ and } \frac{M_{001}}{M_{111}} = \frac{\alpha_{001}\beta_{001}}{\alpha_{111}\beta_{111}}. \tag{3.6}$$

The left sides in the formulas of eq. (3.6) can be determined experimentally from the measured indentation moduli measured on the surfaces (001), (101) and (111). The right sides can be calculated as a function of A and ν_{100}, therefore, if the ratio of the experimentally determined indentation moduli and the theoretically calculated ratio of the correction factors are made equal, the values of A and ν_{100} can be obtained.

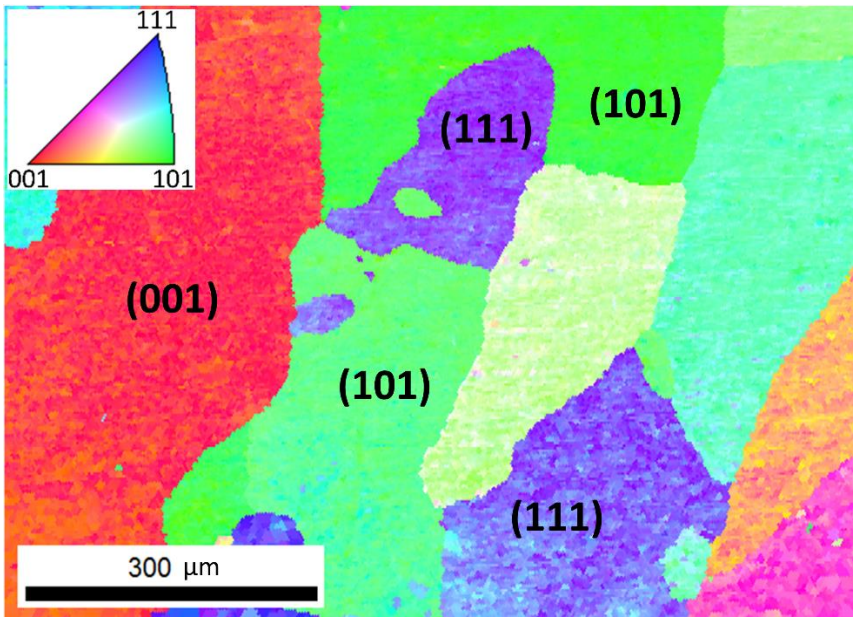

Fig. 3.7: EBSD image showing the area investigated by nanoindentation. The numbers in some grains indicate the indices of the lattice planes parallel to the surface. The indentation moduli obtained for these grains were used to calculate the elastic anisotropy factor.

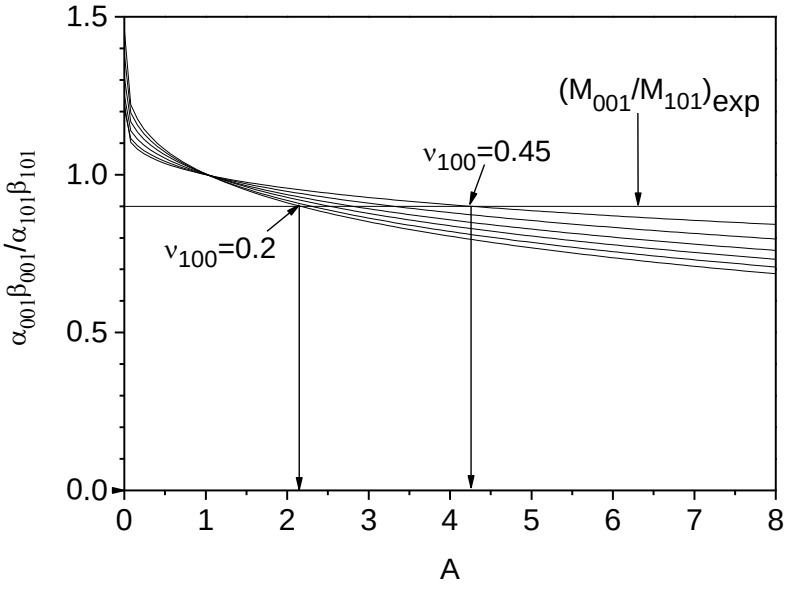

Fig. 3.8: The ratio of the correction factors for the indentation moduli with orientations 001 and 101. The curves correspond to the Poisson ratio (ν_{100}) values of 0.2, 0.25, 0.3, 0.35, 0.4 and 0.45. $(M_{001}/M_{101})_{exp}$ is the experimental value of the ratio of the indentation moduli measured in directions 001 and 101.

In the present experiment, the indentation moduli were determined on the area shown in Fig. 3.7 by nanoindentation using a Berkovich indenter with the maximum load of 100 mN, and the following values were obtained: M_{001}=88 GPa, M_{101}=97 and M_{111}=99 GPa. Figures 3.8 and 3.9 show the calculated ratio of the correction factors for the surface pairs (001)-(101) and (001)-(111), respectively, as a function of the anisotropy factor A for six values of ν_{100} between 0.2 and 0.45.

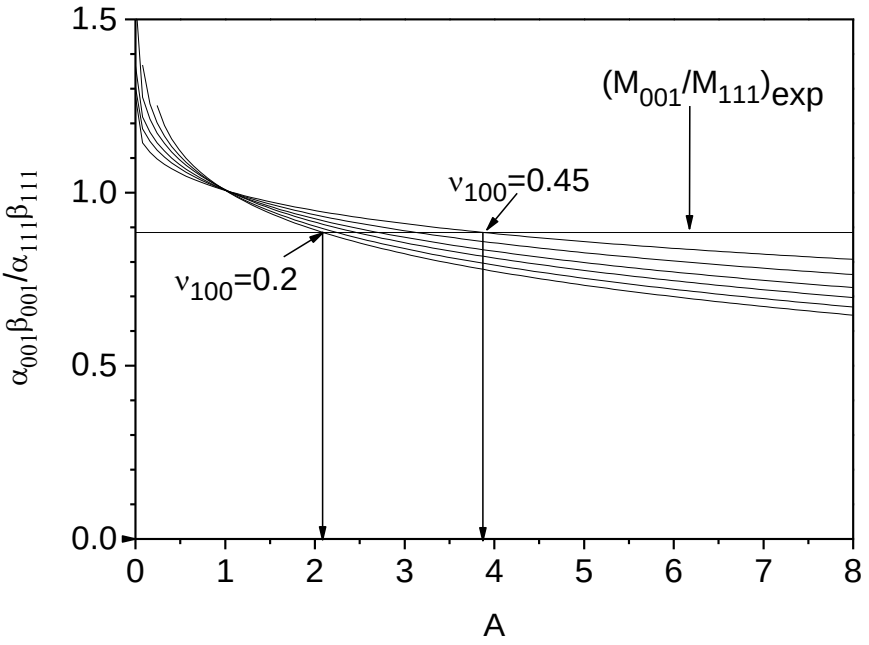

Fig. 3.9: The ratio of the correction factors for the indentation moduli with orientations 001 and 111. The curves correspond to the Poisson ratio (ν_{100}) values of 0.2, 0.25, 0.3, 0.35, 0.4 and 0.45. $(M_{001}/M_{111})_{exp}$ is the experimental value of the ratio of the indentation moduli measured in directions 001 and 111.

The intersection of each curve with the experimental ratio of the indentation moduli gives a possible value of A for a given value of ν_{100}. Then, for (001)-(101) and (001)-(111) surface pairs the functions of the anisotropy factor A versus the Poisson ratio ν_{100} are plotted in Fig. 3.10. From the coincidence of the two curves, 2.3 ± 0.2 and 0.25 ± 0.05 are obtained for A and ν_{100}, respectively. With the help of this anisotropy factor, the values of parameter q for pure screw and edge

dislocations can be estimated from Fig. 3.6 (see the vertical dashed line) as 2.65 ± 0.05 and 1.1 ± 0.5, respectively.

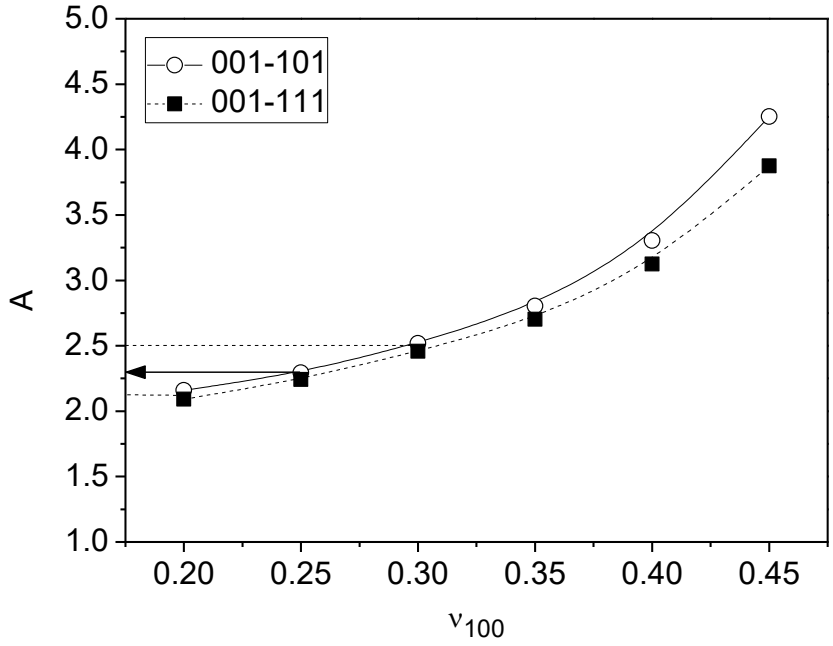

Fig. 3.10: The anisotropy factor A versus the Poisson ratio ν_{100} determined from the indentation moduli ratios for 001-101 and 001-111 orientation pairs. The two curves coincide at the anisotropy factor of 2.3 ± 0.2.

3.1.4 Discussion of the X-ray Line Profile Analysis Results obtained for the Compressed Samples

The comparison of the theoretically calculated and the experimentally obtained q values (see Table 3.1) suggests that with increasing strain the dislocation character became more screw. This can be explained by the reduced mobility of screw dislocations compared to edge dislocations in bcc structures. This difficulty in motion of screw dislocations is due to the fact that the dislocation core of screw dislocations is dissociated into a non-planar configuration, while edge dislocations

are splitted into partials only in their glide planes [128]. As a consequence, during plastic deformation edge dislocation segments can annihilate more easily than the screw ones, thereby the remaining dislocations have more screw character. It should be noted that the value of $\overline{C}_{h00}$ also depends on the anisotropy factor, as shown in [108]. For $A = 2.3 \pm 0.2$ and $0.5 < c_{12}/c_{44} < 2$, the values of $\overline{C}_{h00}$ are 0.305 ± 0.015 and 0.260 ± 0.045 in the cases of screw and edge dislocations, respectively [108]. Since $\overline{C}_{h00}$ only slightly depends on the edge/screw character of dislocations, the average of the values obtained for pure screw and edge cases (0.28) was used in each X-ray diffraction pattern fitting procedure for the determination of the dislocation density.

The area-weighted mean diffraction domain size and the dislocation density determined from the diffraction peak profile analysis for the compressed samples are listed in Table 3.1. For the initial material, the diffraction peaks were as narrow as the instrumental profiles ($\Delta(2\Theta)$=0.02°), therefore these lines were not evaluated for the microstructure. It is noted that the peak breadths obtained for the initial sample reflect the diffraction line broadening caused by the distortion of the lattice due to different-sized atoms in the present HEA. Therefore, with the application of the instrumental correction, this distortion effect was eliminated during the evaluation of line profiles. In the sample compressed at 3%, the diffraction domain size and the dislocation density were 151 nm and 2.0×10^{14} m^{-2}, respectively. It is noted that in plastically deformed metallic materials the diffraction domain size obtained by X-ray line profile analysis is usually smaller than the grain size determined by electron microscopy. This difference can be explained by the fact the diffraction domain is equivalent to the volume scattering X-rays coherently which often corresponds rather to the subgrains in deformed materials. It was found that the diffraction domain size decreased while the dislocation density increased with increasing strain during compression of the present HEA material, and their values reached about 123 nm and 10×10^{14} m^{-2}, respectively, at the strain of 10%. After compression up to 20%, the diffraction domain size was reduced to 39 nm, while the dislocation density increased to 15×10^{14} m^{-2}. Similar high dislocation

density in conventional alloys can be obtained only by severe plastic deformation at an equivalent strain of about 100% [129].

In the center of the impacted samples the dislocation density was even higher with the values of about 47×10^{14} m^{-2} and 32×10^{14} m^{-2} for the velocities of 10 and 20 m/s, respectively, due to the very large imposed strain (50 and 130 %, respectively). The smaller dislocation density for the sample impacted at 20 m/s compared to that deformed at 10 m/s can be explained by a possible recovery of the microstructure due to the annealing of the material at high strain rates, as shown in previous works, e.g. in [130]. This annealing is a consequence of the temperature rise caused by the fast conversion of plastic work into heat during impact test.

3.1.5 TEM and SEM Investigations of the Deformed Microstructures

Fig. 3.11 shows TEM micrographs for $Ti_{20}Zr_{20}Hf_{20}Nb_{20}Ta_{20}$ samples compressed to different plastic strains of 1% (Fig. 3.11a), 3% (Fig. 3.11b) and 10% (Fig. 3.11c). It can be seen that for small strains the deformation localizes within bands that delineate defect free domains inside the grains. Both the number of bands and the dislocation density inside the bands seem to increase with increasing plastic strain. The Burgers vector and the edge/screw character of dislocations within the bands have been studied in details by TEM [131]. Careful inspection of the TEM images using the extinction rule for dislocations showed that the Burgers vector is of $a/2<111>$ type and the dislocations at higher strains are mainly of screw character, which is in line with the XLPA results described above. Although TEM investigates a much smaller volume than that in XLPA, the images reflect relatively well the order of magnitude of the average dislocation density determined by the latter method. For instance, the average dislocation spacing at a strain of 10% is 32 nm determined as the inverse square root of the dislocation density obtained by XLPA. This value is in accordance with the visual observation of the dislocation spacing in Fig. 3.11c. The comparison of the TEM images obtained at different strains (see Fig. 3.11)

reveals a high rate of the increase of dislocation density during plastic deformation which is also in accordance with the results of XLPA. This observation can be explained by the difficult annihilation of dislocations due to the high stress required for dislocation motion in HEA materials. The magnitude of attractive force between dislocations with opposite signs in HEAs is not very different from that in other bcc metals since the elastic constants and Burgers vector magnitude are similar. At the same time, the stress required for dislocation motion (i.e., the Peierls stress) is expected to reach a much higher value in HEAs than in other bcc metals, therefore dislocations with opposite signs can exist closer to each other without annihilation. Due to the hindered annihilation, the dislocation density will be larger for a given strain.

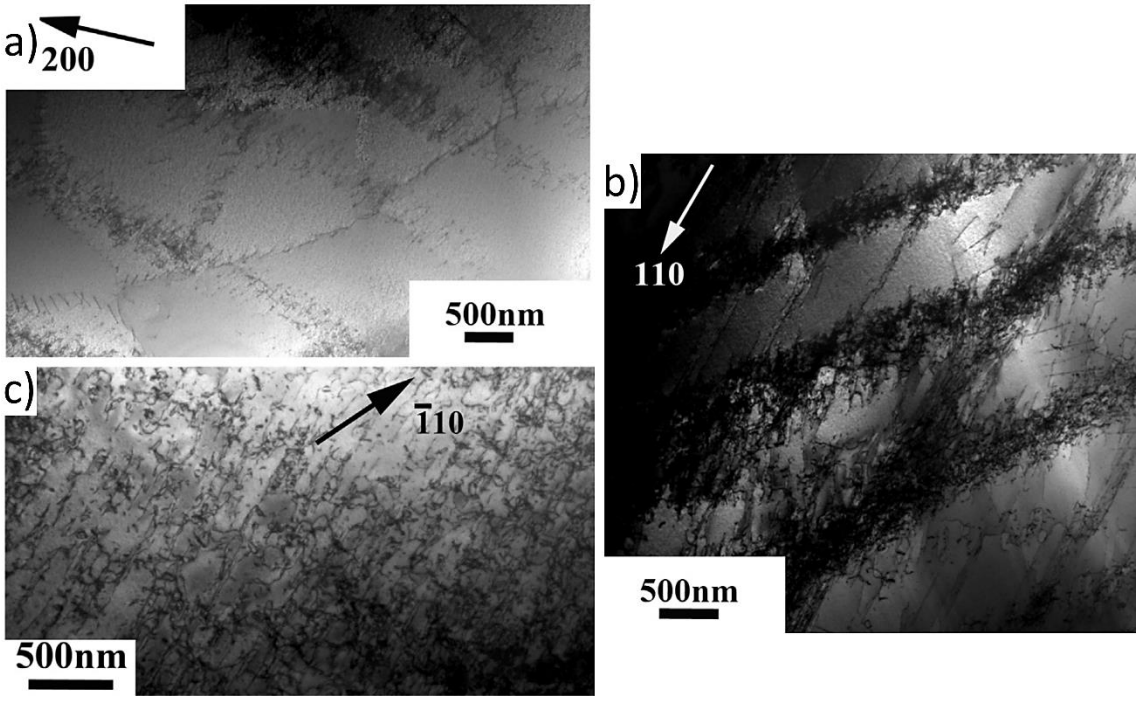

Fig. 3.11: TEM micrographs showing the dislocation patterning after compression test at room temperature for different plastic strains: (a) ε ~ 1%; (b) ε ~ 3%; (c) ε ~ 10% (The TEM images was taken at University of Paris 13).

The EBSD image in Fig. 3.12 shows the microstructure after impact at a velocity of 10 m/s. Fig. 3.12 reveals a strong deformation heterogeneity during impact test, since a macroscopic band can be seen which crosses many grains and

subdivides the image into two parts. The right bottom part seems to be much more deformed than the upper left part in the image.

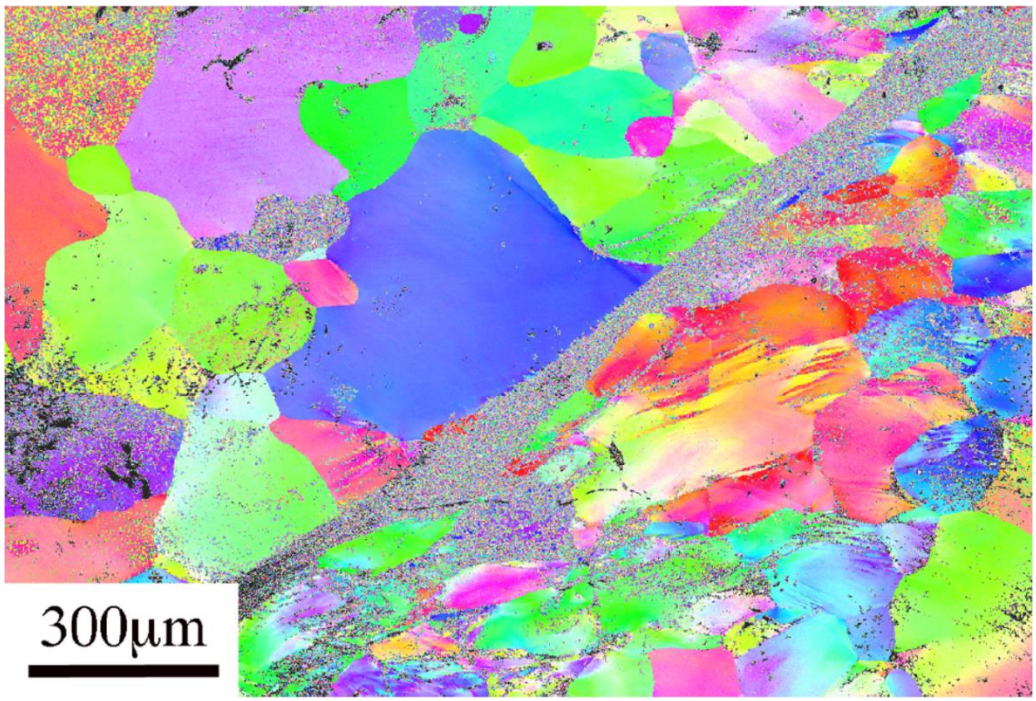

Fig. 3.12: EBSD images showing the microstructure after impact deformation up to a true strain of ~50% at a velocity of 10 m/s (The EBSD image was taken at University of Paris 13).

3.1.6 Correlation Between the Yield Strength and the Dislocation Density

The yield strength of the HEA samples compressed to the strains of 3, 10 and 20% were 980±10, 1035±10 and 1050±11 MPa, respectively. In the cases of the impacted samples, the yield strength was estimated as one third of the hardness determined at the load of 10 N. For the specimens deformed at 10 and 20 m/s, the calculated yield strength values were 1228±12 and 1203±12 MPa, respectively. It is noted that a flow stress value was also determined from the force-displacement data measured in-situ during impact test at 10 m/s, however this value (1450 MPa) measured under dynamic conditions is slightly larger than that obtained for static

loading in hardness test. The yield strength (σ_Y) of plastically deformed metallic materials is usually related to the dislocation density through the Taylor-equation [132]:

$$\sigma_Y = \sigma_0 + \alpha M^T G b \sqrt{\rho}\,, \tag{3.7}$$

where σ_0 is the friction stress, α is a constant, G is the shear modulus, b is the modulus of the Burgers vector (0.2944 nm for the present HEA) and M^T is the Taylor factor. Fig. 3.13 shows the yield strength as a function of the product of the modulus of the Burgers vector and the square-root of the dislocation density for the deformed HEA samples. The datum points well fitted by a straight line according to eq. (3.7). The value of σ_0 obtained from the fitting is 890 $\pm$ 32 MPa, indicating a very large friction stress. The slope of the fitted straight line is 13.6 $\pm$ 1.9 GPa, which can be used for the determination of α. As strong texture was not observed in the samples, M^T was selected to be 3.06. In addition, the average shear modulus was determined from the average Young's modulus (E = 87 GPa) obtained from the indentation measurements and the Poisson's ratio (ν = 0.25) as $G = \frac{E}{2(1+\nu)} = 35\ GPa$, which is close to the theoretically calculated value given in Ref. [124]. Then, α = 0.16 $\pm$ 0.04 was calculated from eq. (3.7), which corresponds to the lower bound of the regime obtained experimentally for different bcc metallic materials (between 0.17 and 0.6, see [139–142]). This observation indicates a relatively low dislocation-induced hardening (i.e., strength increment per unit dislocation density) in the present HEA material. The relatively low value of α for the present HEA material is in line with the low strain hardening observed on the true stress – true strain curve (see Fig. 3.2). It seems that the main component in the compression flow stress is the Peierls stress and dislocation hardening has a lower contribution.

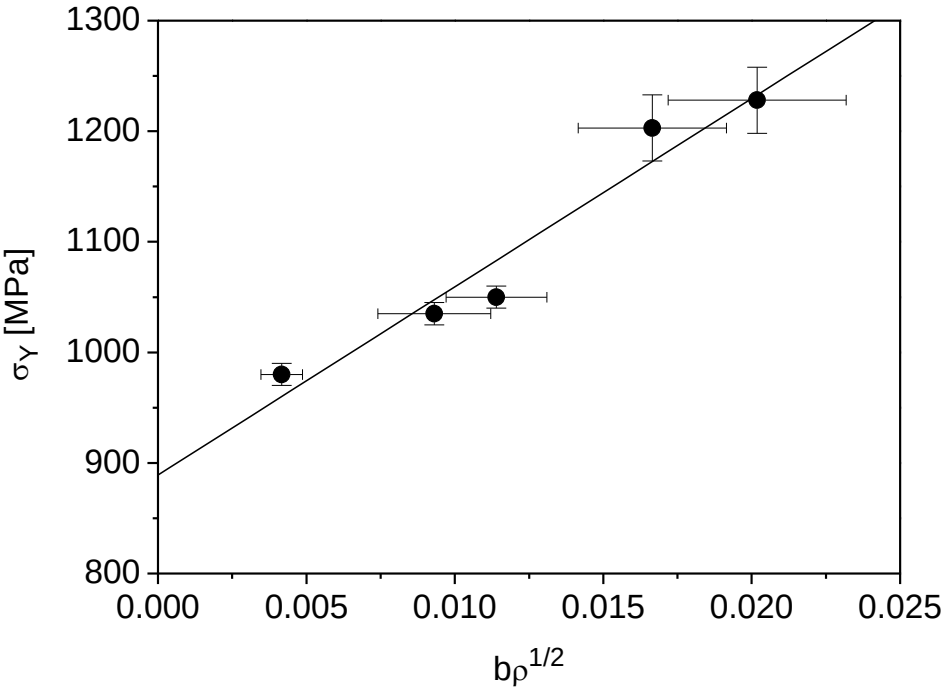

Fig. 3.13: The yield strength as a function of the product of the modulus of the Burgers vector and the square-root of the dislocation density for the deformed HEA samples.

3.1.7 Summary

In summary, the initial $Ti_{20}Zr_{20}Hf_{20}Nb_{20}Ta_{20}$ HEA material was compressed at room temperature to the plastic strains of 3, 10 and 20%. Additionally, two samples were impacted using a Hopkinson pressure bar at the initial impact velocities of 10 and 20 m/s up to the equivalent strains of 50 % and 130 %, respectively. In the initial sample the grain size distribution was broad, ranging between 10 and 350 μm. A high density of dislocations (10-15 × 10^{14} m^{-2}) was developed during compression even at moderate plastic strains (10-20%). In the center of the impacted samples the dislocation density was even higher with the values of about 47 × 10^{14} m^{-2} and 32 × 10^{14} m^{-2} for the velocities of 10 and 20 m/s, respectively. The smaller

dislocation density for the sample impacted at 20 m/s compared to that for 10 m/s can be explained by a possible recovery of the microstructure due to the annealing of the material at high strain rates. The dislocation density obtained by XLPA was in accordance with the dislocation spacing observed in the TEM images.

The single crystal elastic anisotropy factor was determined as 2.3 ± 0.2 by indentation technique which was required for the determination of the edge/screw character and the density of dislocations by XLPA. This method of the determination of the elastic anisotropy factor was developed in my PhD work. Using the obtained elastic anisotropy factor, the theoretical values of the parameter describing the dislocation character were determined for pure edge and screw dislocations. Comparing these values with the experimentally determined parameters, it was found that the screw character of dislocations became stronger with increasing strain. This observation was supported by TEM analysis.

The present HEA material has a high yield strength of about 890 MPa. The strain hardening during compression was caused by the increase of the dislocation density. The dislocation hardening parameter (α) has a relatively low value but it is still in the range determined for other bcc non-HEA metallic materials. The Peierls stress has the main component in the flow stress, and dislocation hardening has a lower contribution even for high dislocation densities.

3.2 Microstructure Development During Plastic Deformation of a Ti-rich $Ti_{35}Zr_{27.5}Hf_{27.5}Nb_5Ta_5$ High-entropy Alloy [R3,R4]

In this chapter, I am going to show the influence of HPT on the microstructure and hardness of a Ti-rich ($Ti_{35}Zr_{27.5}Hf_{27.5}Nb_5Ta_5$) HEA. The HEA was processed by 1 turn of HPT. The evolution of the grain size and the dislocation density was studied by electron microscopy and XLPA. Besides the refinement of the microstructure, a phase transition also occurred during deformation. The initial bcc structure transformed into orthorhombic structure in the whole material. The features of this phase transformation were studied on samples compressed to low strain values.

3.2.1 Microstructure Evolution During HPT

A Ti-rich HEA with a composition of $Ti_{35}Zr_{27.5}Hf_{27.5}Nb_5Ta_5$ was prepared by arc melting under argon atmosphere [137]. The as-cast material was thermo-mechanically treated in order to achieve a recrystallized microstructure using two steps of cold-rolling and annealing at 1200 °C for 24 h. A disk with a diameter of 9.85 mm and a thickness of ~0.85 mm was fabricated from the recrystallized alloy and processed by HPT for 1 turn. The HPT facility operated under quasi-constrained conditions with an applied pressure of 6.0 GPa and a rate of 1 rpm at room temperature [138].

The optical micrograph in Fig. 3.14a shows the microstructure of the initial sample before HPT deformation. The average grain size was determined as ~800 μm. The size and morphology of grains in the HPT-processed sample was investigated using an Automated Crystallographic Orientation Mapping (ACOM) tool attached to a CM20FEG transmission electron microscope (TEM) operating at

200 kV. This method using TEM spot diffraction patterns is an effective technique for mapping phase distribution and crystal orientation. The microstructure at the half-radius of the disk processed by 1 turn of HPT was studied by ACOM-TEM and is shown in Fig. 3.14b. In the HPT-processed sample, many grains are elongated with a broad size distribution. The average thickness and length of the grains are ~200 and ~1000 nm, respectively

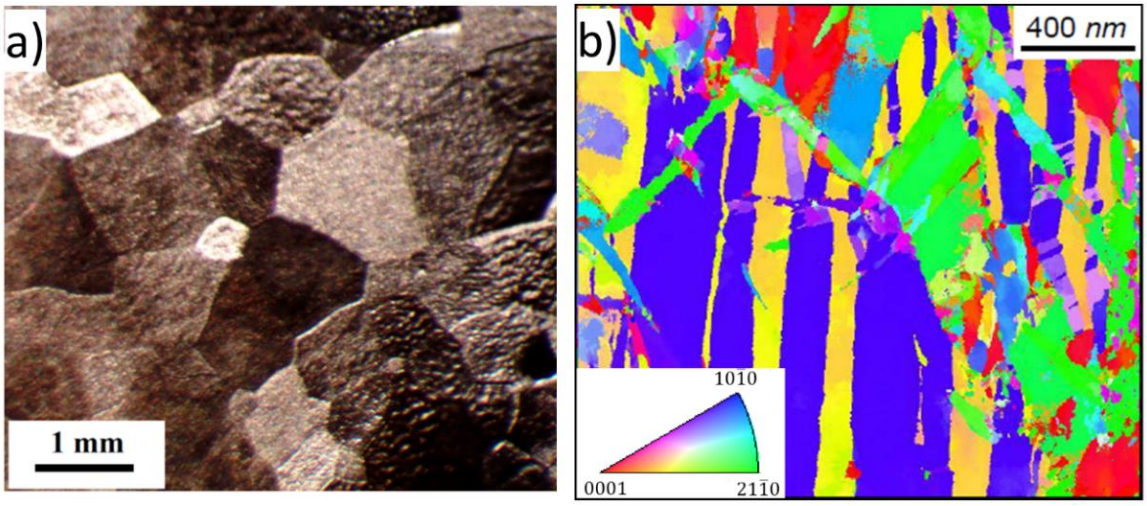

Fig. 3.14: Microstructure evolution in $Ti_{35}Zr_{27.5}Hf_{27.5}Nb_5Ta_5$ HEA during HPT deformation: a) Optical microscopy image of the initial sample, b) ACOM-TEM image showing the microstructure with orthorombic structure at the half-radius of the disk after 1 HPT turn.

3.2.2 Phase Transformation During Plastic Deformation Studied by X-ray Diffraction

The phase composition and the average lattice parameters for the initial and HPT-processed samples were investigated by X-ray diffraction. The lattice parameter was determined by the Nelson–Riley method [114]. The microstructure of the HPT-processed sample was examined by XLPA. In the case of the HPT sample the analysis was carried out at the center, half-radius and periphery of the disk. The diffraction patterns were evaluated by the CMWP fitting method. Fig. 3.15a shows the X-ray

diffraction pattern obtained for the initial undeformed Ti-rich HEA sample. The initial material has a bcc structure with a lattice parameter of ~0.345 nm.

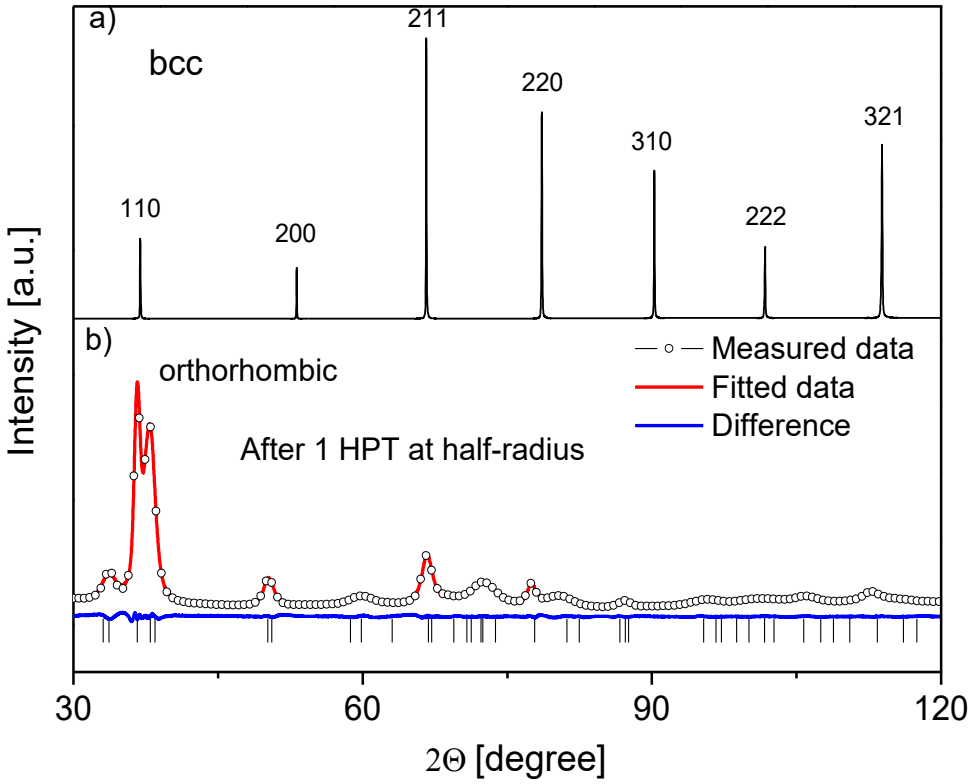

Fig. 3.15: XRD patterns for (a) the initial $Ti_{35}Zr_{27.5}Hf_{27.5}Nb_5Ta_5$ HEA sample and (b) the half-radius of the disk processed by 1 turn of HPT. The orthorhombic peak positions are indicated by small vertical lines. In (b) the experimental diffractogram and the theoretical pattern fitted by the CMWP method are shown by open symbols and a solid line, respectively.

During HPT deformation, the whole material was transformed into an orthorhombic structure, as revealed by the XRD pattern recorded at the half-radius of the HPT-processed disk (see Fig. 3.15b). The new phase was indexed as an orthorhombic structure with the lattice parameters of $a = 0.314$ nm, $b = 0.531$ nm and $c = 0.490$ nm, which shows very good agreement with a former study presented in Ref. [145]. It should be noted that a similar XRD diffractogram was obtained for the as-cast state (before recrystallization) for which the structure was also

determined as orthorhombic with an orthorhombicity of 98% [143]. The orthorhombicity is defined as $b/1.73a$ where a and b are two lattice constants of the orthorhombic phase. An orthorhombicity value of 98% means that the structure was almost hexagonal close-packed (hcp).

The microstructure of the orthorhombic phase after 1 turn of HPT was examined by XLPA. For the determination of the dislocation density, the values of the Burgers vector and the dislocation contrast factors have to be known. The values of the contrast factors depend on the anisotropic elastic constants of the studied crystal. These elastic constants are not known for the present HEA material and cannot be determined by the indentation method presented in the previous section. The main component in this material was Ti and the orthorhombicity value was 98% which means that the structure was almost hcp. Therefore, the dislocation contrast factors in this HEA were approximated by the values determined for Ti [139]. Thus, the dislocation density determined by XLPA is only an estimated value. The XLPA evaluation revealed that there is no significant difference between the diffraction domain size values observed at the center, half-radius and periphery of the disk. The average diffraction domain size was in the range of 11-16 nm. It is noted that the diffraction domain size is much smaller than the grain size obtained by TEM. This difference can be explained by the fact that XLPA measures the size of sub-grains or dislocation cells rather than the true grain size. At the same time, the dislocation density increased with increasing the distance from the disk center. Its values were $\sim 43 \times 10^{14}$ m^{-2} and $\sim 103 \times 10^{14}$ m^{-2} at the disk center and periphery, respectively (see Table 3.2). The very high dislocation density even after one turn of HPT can be explained by a reduced annihilation rate of dislocations during deformation which can be caused by the high stress required for dislocation motion in highly alloyed HEA materials [R1].

The large deformation applied during HPT resulted in a full transformation of the initial bcc structure into an orthorhombic phase. Therefore, for the study of this phase transformation an additional compression investigation was carried out by compression. The results of this mechanical test are shown in the next section.

Table 3.2: The parameters of the microstructure obtained by XLPA. $\langle x \rangle_{area}$ is the area-weighted mean diffraction domain size and ρ is the dislocation density.

Location in the HPT disk	$\langle x \rangle_{area}$ [nm]	ρ [10^{14} m^{-2}]
Center	13 ± 2	43 ± 10
Half-radius	11 ± 2	79 ± 10
Periphery	16 ± 2	103 ± 10

3.2.3 Study of the Phase Transformation by Compression Test

For the study of the onset of phase transformation occurred during HPT, a complementary compression test was carried out on the initial HEA material at room temperature and a strain rate of ~10^{-3} s^{-1} up to the plastic strain of ~11.5% using an MTS universal mechanical testing machine. The measured stress-strain curve is shown in Fig. 3.16. The yield strength of the initial sample was about 277 MPa which is much smaller than the value obtained for the equimolar $Ti_{20}Zr_{20}Hf_{20}Nb_{20}Ta_{20}$ HEA (~890 MPa). This difference can be explained by the much larger average grain size of the Ti-rich HEA (~800 μm) compared to the equimolar sample (~200 μm) and the different chemical composition. The Ti-rich HEA showed a much higher strain hardening than the equimolar material. Namely, between the plastic strains of zero and 11.5%, the stress increased with ~600 MPa and ~200 MPa for the Ti-rich and equimolar HEAs, respectively.

The deformation was interrupted at the plastic strains of 3.7% and 6.9 %, and after unloading the phase composition and the microstructure were investigated. The comparison of the XRD pattern in Fig. 3.17a with Fig. 3.15a reveals that a significant fraction of the material was transformed from bcc to orthorhombic structure even at the strain of 3.7%, and with increasing the strain to 11.5% the

diffraction pattern shows that the orthorhombic phase became more significant (see Fig. 3.17b).

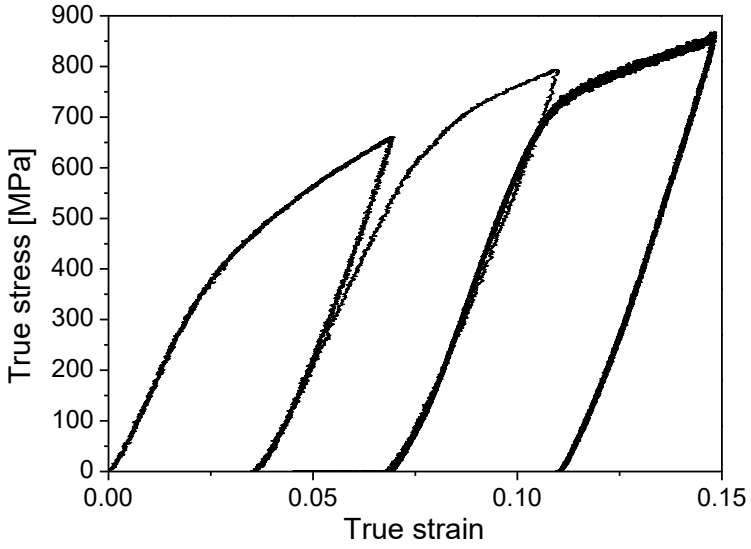

Fig. 3.16: True stress versus true strain curves obtained in compression test. The deformation was interrupted at the plastic strain of ~3.7% in order to investigate the microstructure, then the test was continued up to ~6.9% and ~11.5%.

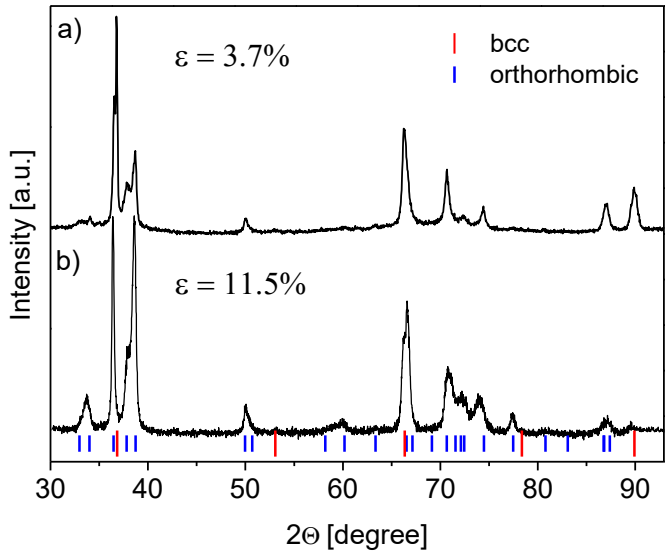

Fig. 3.17: XRD patterns for (a) the sample deformed by compression to the plastic strain of ~3.7%, and (b) to the plastic strain ~11.5%. The peak positions are indicated by small vertical lines.

The microstructure of the compressed specimen was studied by EBSD with a step size of 30 nm using a FEI Quanta 3D SEM. The investigated area was prepared by ion milling for 7 min using an Ar ion beam with an energy of 10 keV and an angle of incidence of ~7°. The surface preparation was carried out by a SEMPrep (SC-1000) device from Technoorg Linda. The EBSD image in Fig. 3.18a shows that the orthorhombic phase formed as lamellae in the bcc grains. This lamellar grain morphology was inherited in the elongated form of the grains in the HPT-processed sample (see Fig. 3.14b) where the whole material has already been transformed into orthorhombic structure. Compositional differences between the bcc and orthorhombic phases were not observed by EDS, which suggests that the bcc→orthorhombic transition is a martensitic phase transformation without diffusion. After compression to the plastic strain of 6.9% (see Fig. 3.18) only a minor fraction of the material remained in bcc structure which indicates that the phase transformation during HPT most probably occurred already at the beginning of deformation.

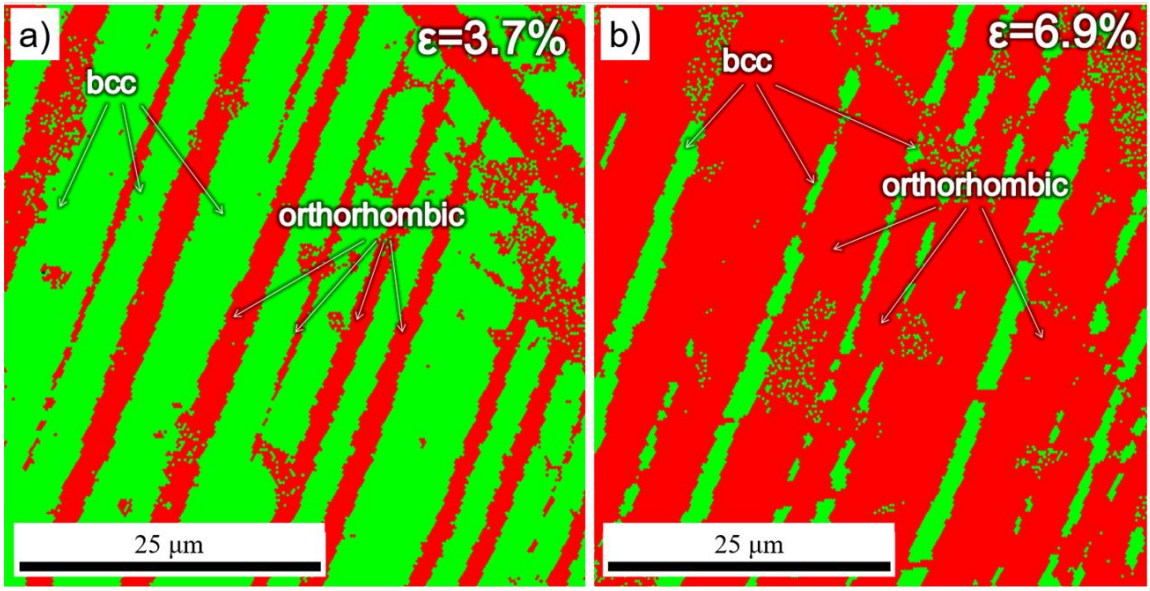

Fig. 3.18: EBSD images showing the bcc and orthorhombic phases after compression at the plastic strain of 3.7% (a) and 6.9% (b) (the green and the red regions represent the lamellae of bcc and orthorhombic phases, respectively).

After compression up to the plastic strain of 11.5 %, the material still has not been transformed completely into orthorhombic phase (see Fig 3.19b). The SEM image in Fig. 3.19a reveals a lamellar microstructure inside the coarse grains at the plastic strain of 11.5%. Lilensten et al. [140] also studied the phase transformation in this HEA during tension up to the plastic strain of 17%, but the complete phase transformation was not observed.

Table 3.3 shows the phase composition determined by X-ray diffraction and EBSD. The volume fraction of bcc and orthorhombic phases were characterized by the ratio of the summed intensity under all peaks in the diffractograms. As shown in Table 3.3, the volume fraction of the orthorhombic phase increased with increasing strain during compression test. The EBSD images (see Fig. 3.18 and 3.19b) were used to calculate the volume fractions of the two phases. The EBSD analysis also revealed a high volume fraction (87%) of the orthorhombic phase after compression at a plastic strain of 11.5%.

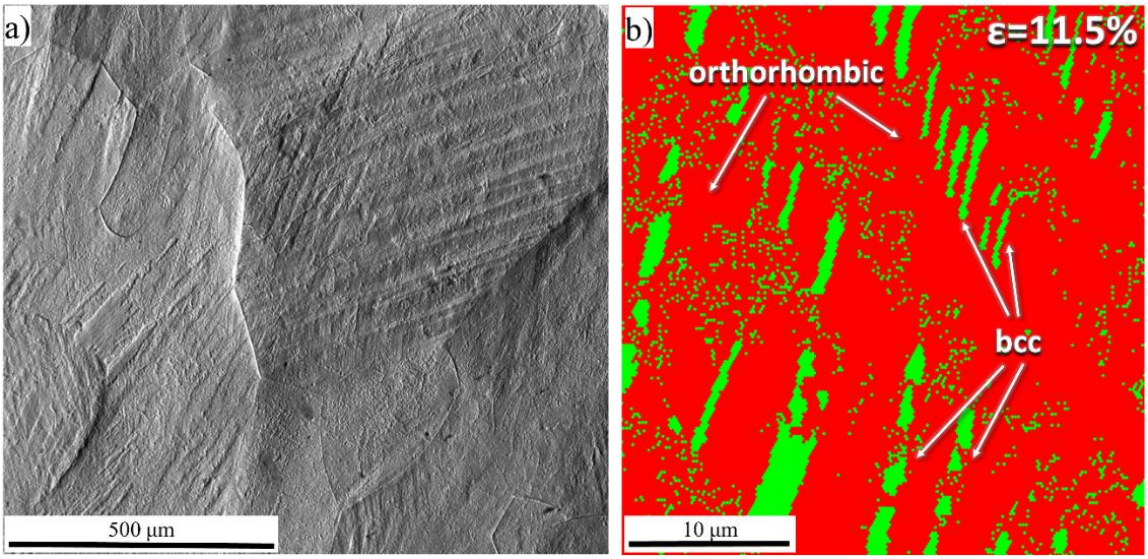

Fig. 3.19: (a) SEM image showing the lamellar structure after compression at a plastic strain of 11.5% and (b) EBSD image showing the bcc and orthorhombic phases (the green and the red regions represent the bcc and orthorhombic phases, respectively).

Table 3.3: The phase composition determined by X-ray diffraction and by electron microscopy (EBSD).

	XRD		EBSD	
Sample	**bcc [%]**	**orthorhombic [%]**	**bcc [%]**	**orthorhombic [%]**
3.7%	36±5	64±10	61±9	39±6
6.9%	22±3	78±12	19±3	81±12
11.5%	11±2	89±13	13±2	87±13

It can be seen in Table 3.3 that the bcc phase fraction obtained from EBSD after compression at the plastic strain of 3.7% was significantly higher than the value measured by XRD. This can be explained by the fact that EBSD investigates only a small area on the sample surface compared to XRD, i.e., the latter method characterizes the phase composition with a better statistics. However, after compression at the plastic strains of 6.9% and 11.5%, the phase fractions determined by EBSD and XRD show a very good agreement. It can be concluded that the bcc structure transforms into orthorombic at very small strains, and at a strain of about 12% almost the whole material has an orthorombic structure.

The lattice defect structure in the compressed specimens was studied by XLPA. Fig. 3.20 shows the Debye-Scherrer rings for the first 5 reflections after the compression test. The rings detected for the plastic strains of 3.7% and 6.9% contain high intensity spots which are caused by the large grains with very low dislocation density. These rings cannot be evaluated as the breadth of the spots was close to the instrumental broadening. For these samples, the diffraction domain size was larger while the dislocation density was lower than the detection limits of the present diffraction configuration (~1 μm and ~10^{13} m^{-2}, respectively). Another difficulty in the XLPA evaluation for the Ti-rich HEA was caused by the strong overlapping of the diffraction peaks of the two phases. However, after compression at a plastic strain of 11.5% the rings were sufficiently homogeneous for the evaluation and the sample was nearly a single phase material with an orthorhombic structure.

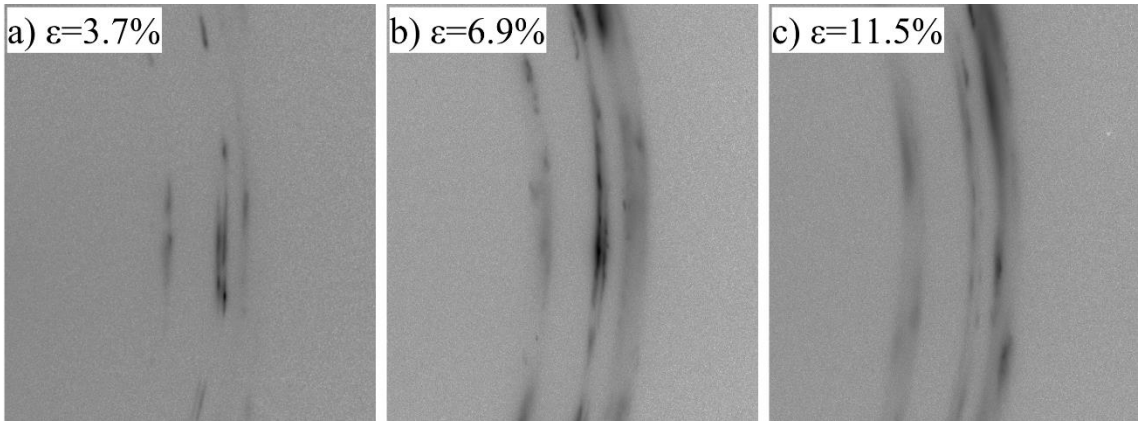

Fig. 3.20: The Debye–Scherrer rings for the first five reflections after compression test at different strains.

After compression at a plastic strain of 11.5%, ~90% of the Ti-rich HEA was transformed into an orthorhombic structure. Therefore, the XLPA was performed on the orthorhombic phase. After compression up to the plastic strain of 11.5% the diffraction domain size and the dislocation density were 25 nm and 11×10^{14} m^{-2}, respectively. It is noted that the diffraction domain size obtained by XLPA was much smaller than the grain size in Fig. 3.19. This difference can be explained by the fact that the diffraction domain is equivalent to the volume scattering X-rays coherently and the dislocation pattern inside the grains may break the coherency of X-rays. It should be noted that the dislocation density obtained in the Ti-rich HEA after compression up to the strain of 11.5% was close to the value determined for the equimolar $Ti_{20}Zr_{20}Hf_{20}Nb_{20}Ta_{20}$ HEA compressed to a similar strain (see Table 3.1). This is an interesting observation as both the chemical and the phase compositions were different in the two HEAs.

3.2.4 Microhardness of the HPT processed Ti-rich HEA

The hardness distribution along the radius of the HPT-processed disk is shown in Fig. 3.21. The hardness in the disk center is ~3500 MPa, which increased slightly towards the disk edge. At the periphery of the sample the hardness was ~3900 MPa.

The small difference between the hardness values measured at the center and the periphery is in accordance with the slight variation of the microstructural parameters along the disk radius (see Table 3.2). The hardness of the initial sample is ~3000 MPa, which suggests that 1 turn of HPT resulted in only a 20-30% increment in hardness despite the strong reduction in grain size and the large increment in dislocation density. However, if we determine the hardness as three times the yield strength (σ_y = 277 MPa), ~831 MPa is obtained (see Fig. 3.21) which is much smaller than the experimental value of the hardness (~3000 MPa). The difference can be explained by the strong hardening in the beginning of deformation as revealed by the compression data in Fig. 3.16.

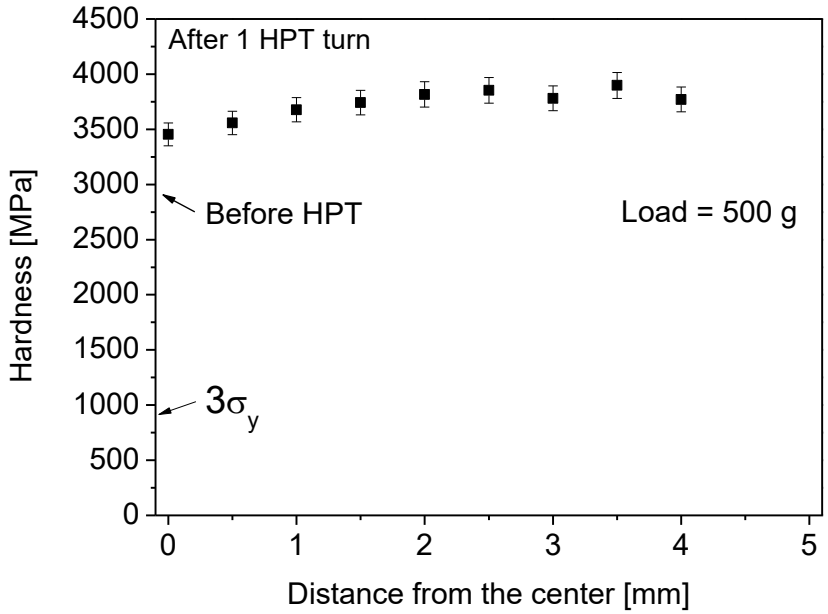

Fig. 3.21: The average Vickers microhardness versus the distance from the center for the disk processed by 1 turn of HPT. The hardness obtained before HPT is also indicated which is much larger than three times the yield strength which is also shown in the figure as $3\sigma_y$.

The hardness corresponds to the flow stress at a plastic strain of ~8% [141], therefore its value may be much larger than three times the yield strength due to strain hardening. In our case, the second loading cycle in the compression test was finished at a plastic strain of ~7%. The corresponding flow stress is ~800 MPa, which is close to the value determined as one-third of the hardness measured on the

initial sample (~1000 MPa). Therefore, the strengthening caused by 1 turn of HPT is much larger than that estimated from the hardness increment due to the large strain hardening in the beginning of deformation.

3.2.5 Summary

Summarizing this chapter, the evolutions of the phase composition, microstructure and hardness during plastic deformation of a Ti-rich HEA with the composition of $Ti_{35}Zr_{27.5}Hf_{27.5}Nb_5Ta_5$ were presented. Due to HPT-processing, the initial grain size (~800 μm) was refined to ~200-1000 nm irrespective of the location along the disk radius. In this Ti-rich HEA material, besides the refinement of the microstructure, a phase transition also occurred during HPT. The initial bcc phase was transformed into a martensitic structure throughout the disk. The martensitic phase was identified as orthorhombic structure. The dislocation density in the orthorhombic phase increased to a very high value of $\sim 10^{16}$ m^{-2} at the periphery of the disk processed by 1 turn of HPT. A very high hardness with values between 3500-3900 MPa was measured on the HPT-processed sample, which changed only slightly along the disk radius in accordance with the microstructure observations. These results indicate a very early saturation of the microstructure and the hardness with increasing strain imposed in HPT-processing.

Complementary compression test revealed that the phase transformation during deformation starts with the formation of orthorhombic lamellae in the initial bcc grains. This grain morphology was inherited in the elongated grain shape in the HPT-processed disk. The phase transformation was nearly completed even at a strain of about 11.5%. The yield strength of the initial material was ~277 MPa, which is much smaller than one-third of the hardness (~1000 MPa) measured on the initial sample due to the strong strain hardening in the beginning of compression. The yield strength and the strain hardening were lower and higher, respectively, for the Ti-rich HEA than in the case of the equimolar $Ti_{20}Zr_{20}Hf_{20}Nb_{20}Ta_{20}$ material.

3.3 Microstructure and Hardness of Equiatomic $Co_{20}Cr_{20}Fe_{20}Mn_{20}Ni_{20}$ High-entropy Alloy Processed by HPT [R5,R6]

In this chapter, I show the evolution of the lattice defect structure (such as dislocations or twin-faults) during HPT deformation, and their influence on the mechanical behavior of $Co_{20}Cr_{20}Fe_{20}Mn_{20}Ni_{20}$ HEA. The evolution of the grain size, the dislocation density and the twin-fault probability was determined at the center and the periphery of the disks processed by HPT up to 2 turns. The detailed characterization of the lattice defect structure was carried out with a combination of XLPA, EBSD and TEM. The local mechanical behavior was studied by micropillar compression test

3.3.1 Microstructure and Elemental Distribution in the As-cast Material

A HEA material with the composition of $Co_{20}Cr_{20}Fe_{20}Mn_{20}Ni_{20}$ (in at. %) was prepared by arc-melting of a mixture of pure metals (purity > 99 wt.%) in a Ti-gettered high-purity Ar atmosphere. The ingots were remelted at least four times to promote chemical homogeneity. The melted alloys were then drop-cast into a mold with dimensions of 10 mm × 10 mm × 60 mm. The as-cast samples (disks having a diameter of ~10 mm and a thickness of ~0.8 mm) were subjected to HPT at room temperature (RT) under quasi-constrained conditions [138] using a rate of 1 rpm under a pressure of 3.0 GPa. The applied numbers of turns were 1/4, 1/2, 1 and 2.

The measured X-ray diffractograms indicated that the initial material was a single phase face-centered cubic (fcc) structure with a lattice parameter of $a = 0.3599 \pm 0.0001$ nm. Neither the structure nor the lattice parameter changed during HPT. Figs. 3.22a and b show EBSD and backscattered electron (BSE) SEM images of

the as-cast microstructure, respectively. In the EBSD image, preferred crystallographic orientation of the grains was not observed (see Fig. 3.22a).

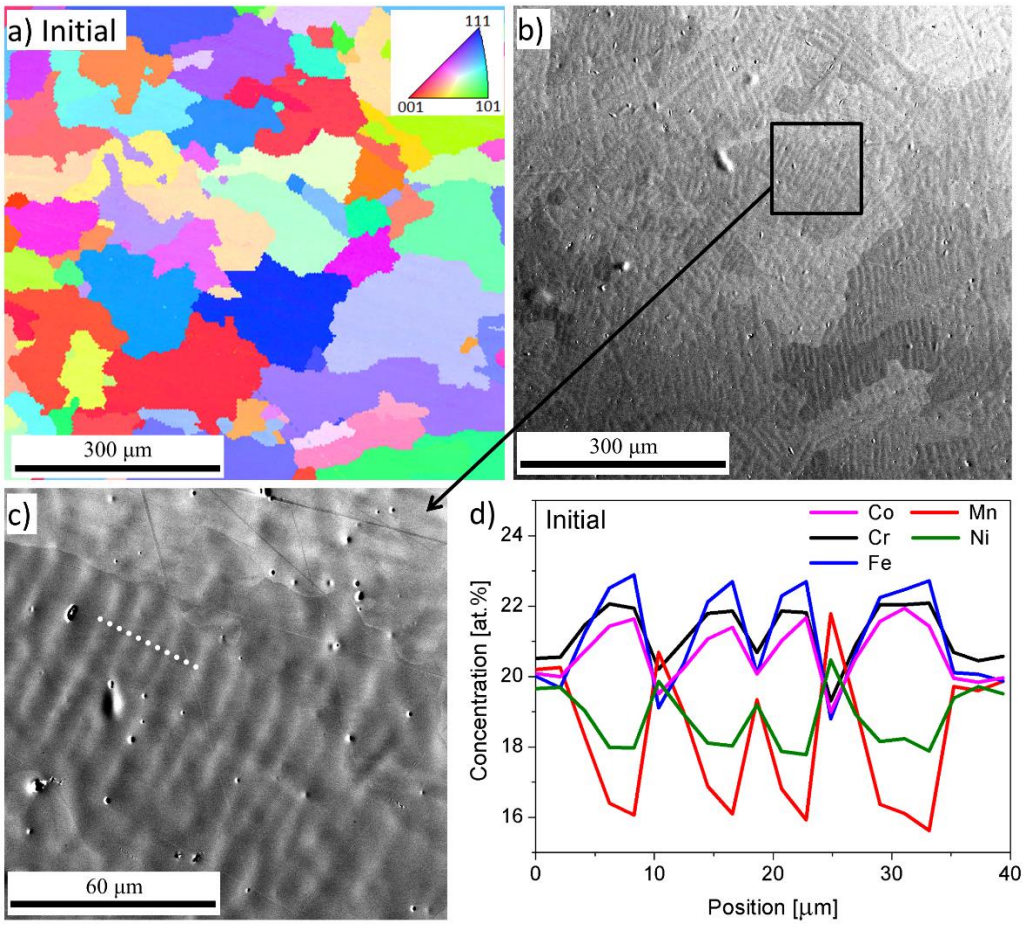

Fig. 3.22: (a) EBSD image and (b) SEM-BSE picture for the initial as-cast sample. A part of (b) is shown in a higher magnification in (c). The chemical composition was investigated by EDS along the white dotted line in (c). The fractions of the five constituents versus the position along the dotted line are shown in (d).

The grains were considered as the regions in the EBSD images bounded by high-angle grain boundaries (HAGBs) with misorientations larger than 15°. In the initial sample, the grain size values have a broad distribution between 10-250 µm with a number-weighted average value of ~60 µm. The EDS analysis performed in different areas revealed that the elemental fractions deviate slightly from the nominal equimolar chemical composition. Namely, the atomic concentrations for Co, Cr, Fe, Mn and Ni were 20.1 ± 1.3, 20.9 ± 3.7, 20.4 ± 3.0, 19.4 ± 4.5 and 19.3 ± 3.3 at. %, respectively, as measured at twenty-five randomly selected areas in the initial

sample. The uncertainties of the values were calculated from the differences in the concentrations obtained in the various areas. The BSE images in Figs. 3.22b and c reveal a dendritic-like microstructure in the initial sample. The fractions of the five constituents in the as-cast CoCrFeMnNi HEA were determined along the white dotted line (perpendicular to the dendritic arms) in Fig. 3.22c by EDS and the results are shown in Fig. 3.22d. An inhomogeneous spatial distribution of the five chemical elements with a periodicity of ~8 μm is revealed. The atomic concentrations of Co, Cr and Fe vary in a complementary manner with the Ni and Mn contents, i.e., where Co, Cr and Fe concentrations increase to 22-23 at.%, Ni and Mn fractions decrease to 16-18 at.%. The largest concentration fluctuations were observed for Fe and Mn. This result is in accordance with former studies (e.g., [142]) which showed that the dendritic areas in an as-cast CoCrFeMnNi HEA are enriched in Co, Cr and Fe and depleted of Ni and Mn.

3.3.2 Evolution of the Microstructure and the Elemental Distribution During HPT

Figs. 3.23a, b and c show the microstructures at the center, half radius and periphery of the HPT disk processed for 1/4 revolution. The number-weighted average grain size was measured as ~33 μm in the center of the disk, which is smaller by a factor of two than in the as-cast specimen (see Fig. 3.23a). The microstructure at the half-radius was studied only for this sample as previous investigations on CoCrFeMnNi HEA suggested that significant twinning occurs in this material even at small shear strains (above the shear strain of 0.5 [143]). Indeed, Fig. 3.23b reveals considerable twinning at the half-radius of the sample processed for 1/4 turn. The twins are indicated by white arrows in the figure. The average twin boundary spacing is about 1 μm. It is noted that the shear strain for the location shown in Fig. 3.23b is about 5.6, which is much higher than the above mentioned critical shear strain for twinning in CoCrFeMnNi HEA. Fig. 3.23c shows that the number-weighted average grain size was reduced to ~233 nm at the periphery of the disk. The two orders of

magnitude smaller grain size at the periphery compared to the center in the disk processed by 1/4 turn indicates a very rapid grain refinement in this HEA with increasing shear strain during HPT processing. The grain size values obtained by microscopic methods are listed in Table 3.4.

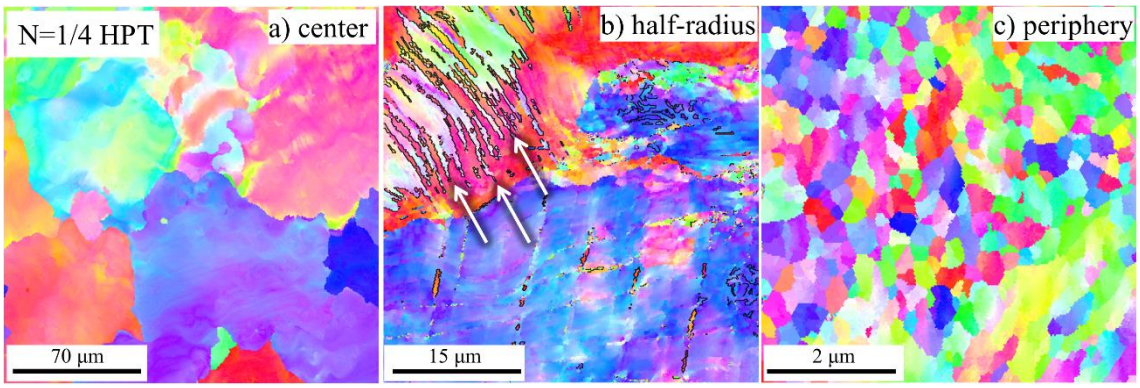

Fig. 3.23: EBSD images showing the microstructures at (a) the center, (b) the half-radius and (c) the periphery of the HEA disk processed by 1/4 turn of HPT. The white arrows in (b) indicate twins formed due to HPT deformation. The color code for the maps is shown in the inset in Fig. 3.22a.

Table 3.4: The grain size (d) determined by electron microscopy (EBSD or TEM), the area-weighted mean diffraction domain size ($\langle x \rangle_{area}$), the dislocation density (ρ) and the twin-fault probability (β) obtained by XLPA. The corresponding shear strain values are also shown.

Number of turns	location	γ	d	$\langle x \rangle_{area}$ [nm]	ρ [10^{14} m^{-2}]	β [%]
1/4	center	0.55	33 ± 5 µm	51 ± 6	43 ± 5	< 0.1
	periphery	8.7	233 ± 20 nm	34 ± 5	91 ± 9	< 0.1
1/2	center	1.4	19 ± 2 µm	61 ± 8	66 ± 8	< 0.1
	periphery	22.1	37 ± 6 nm	28 ± 4	120 ± 14	< 0.1
1	center	2.3	4.8 ± 0.8 µm	20 ± 3	113 ± 12	< 0.1
	periphery	36.4	34 ± 7 nm	29 ± 5	185 ± 21	2.2 ± 0.1
2	center	4.6	3.7 ± 0.7 µm	22 ± 4	126 ± 14	< 0.1
	periphery	73.9	27 ± 5 nm	22 ± 3	194 ± 20	2.7 ± 0.2

Figs. 3.24a-c show EBSD images taken at the centers of the disks processed by HPT for 1/2, 1 and 2 turns, respectively. Table 3.4 reveals that between 1/4 and 1/2 turns the number-weighted average grain size in the disk center decreased to about 19 μm. Between 1/2 and 1 turns, the grain size was refined from ~19 to ~4.8 μm in the center of the HPT-processed disks. After 2 turns, the number-weighted average grain size decreased to ~3.7 μm in the disk center. In addition to the grain refinement, twins were also formed inside the grains as illustrated for 1 turn in Fig. 3.24d, which was obtained by magnifying a part of Fig. 3.24b. The Σ3 boundaries in Fig. 3.24d are represented by thick black lines and some twinned regions are indicated by white arrows. The mean spacing between the twin boundaries is ~3 μm, as estimated from the EBSD images.

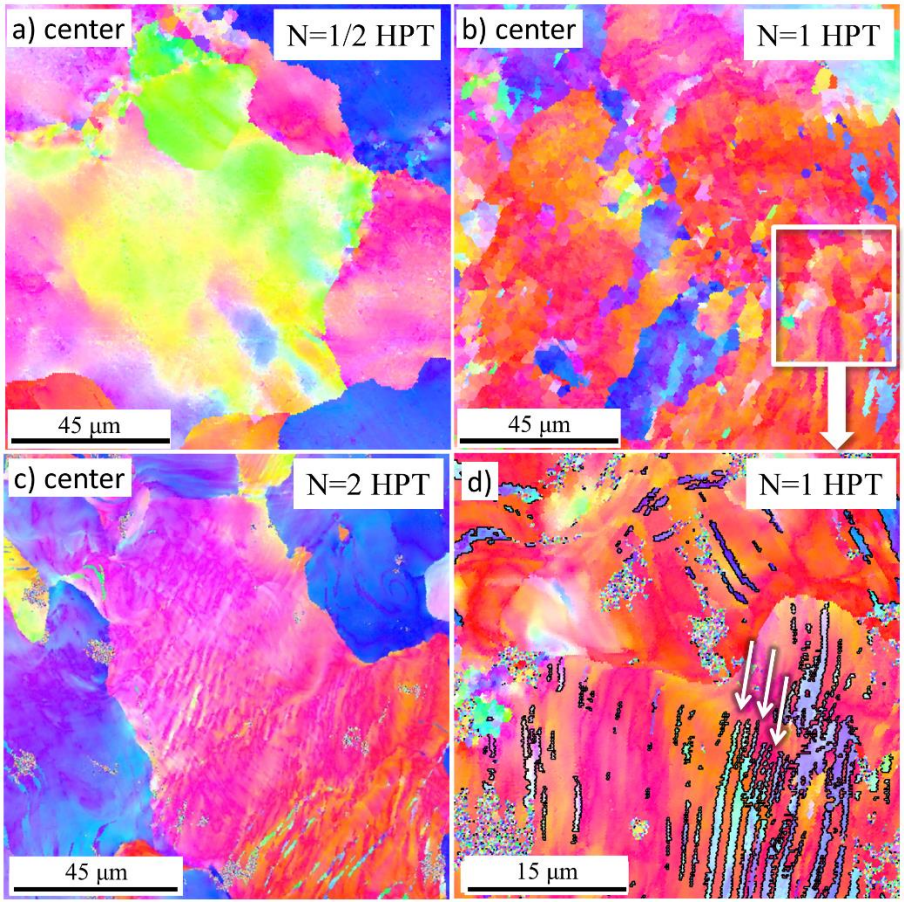

Fig. 3.24: EBSD images showing the center of the disks in the HEA sample after (a) 1/2, (b) 1 and (c) 2 turns of HPT. The thick black lines in (d) represent Σ3 boundaries and some twin crystals are indicated by white arrows. The color code for the maps is shown in the inset in Fig. 3.22a.

As already mentioned, due to the heavily distorted microstructure at the disk peripheries for 1/2, 1 and 2 turns, the microstructures at these locations were investigated by TEM. Figs. 3.25a, b and c show representative dark-field (DF) TEM images for the samples processed by 1/2, 1 and 2 turns. The average grain sizes determined from the TEM images were ~37, ~34 and ~27 nm for 1/2, 1 and 2 turns, respectively. About one hundred and fifty grains were evaluated for the calculation of the average grain size of each sample.

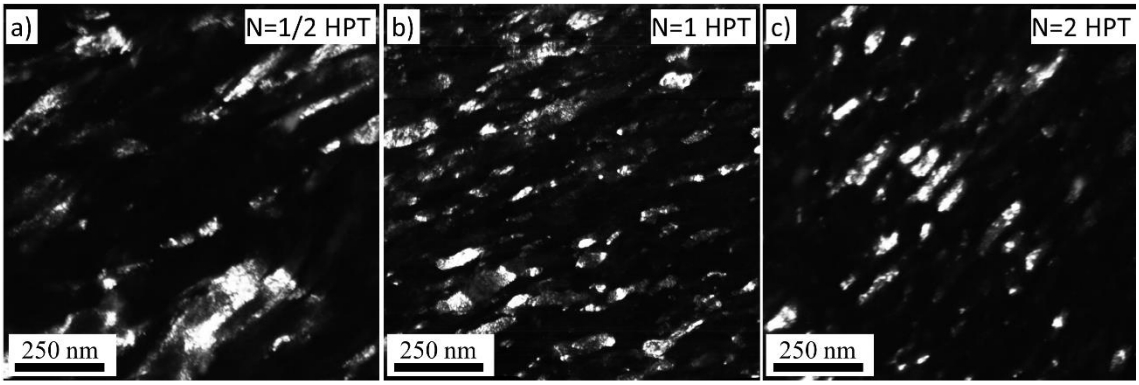

Fig. 3.25: Dark-field TEM images taken at the periphery of the disks processed by (a) 1/2, (b) 1(c) and 2 turns of HPT.

The bright-field TEM images in Fig. 3.26 illustrate that twin faults with a high frequency were formed inside the nanograins at the periphery of the disk processed by 1 turn of HPT. Some nanotwinned lamellae are indicated by black arrows. The twin fault spacing varies between 1 and 10 nm in the nanocrystals shown in Fig. 3.26. By comparison, in the center of the same disk, the twin boundary spacing was about ~3 μm as shown in Fig. 3.24d. This observation suggests that, in addition to the decrease in grain size, the twin fault frequency was enhanced significantly with increasing imposed strain in HPT processing.

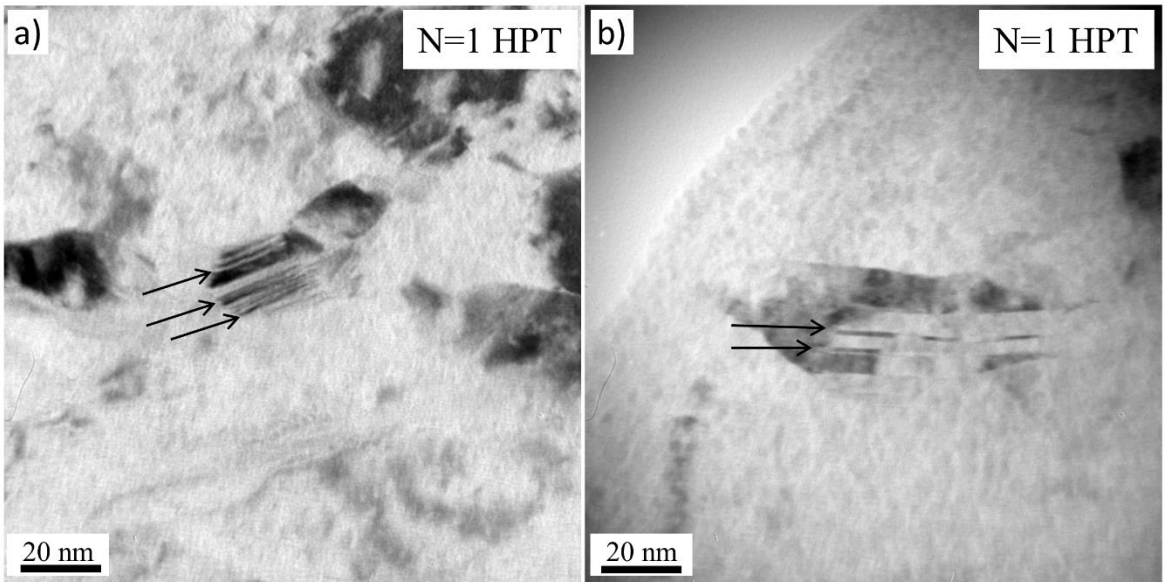

Fig. 3.26: Bright-field TEM images showing twinned grains at the periphery of the disk processed by 1 turn of HPT.

The elemental distributions were also investigated in the center and the periphery of the disks processed by the lowest (1/4) and the highest (2) numbers of HPT turns. The EDS results are shown in Fig. 3.27. The inhomogeneous chemical element distribution in the initial material was inherited into the HPT-processed samples (see Fig. 3.23). Due to HPT processing, although the frequency of concentration oscillations decreased, the concentration differences did not change considerably (compare Figs. 3.22d and 3.27d). Similar to the initial state, the atomic concentrations of Co, Cr and Fe vary in a complementary way with the Ni and Mn contents and the largest concentration fluctuations were observed for Fe and Mn.

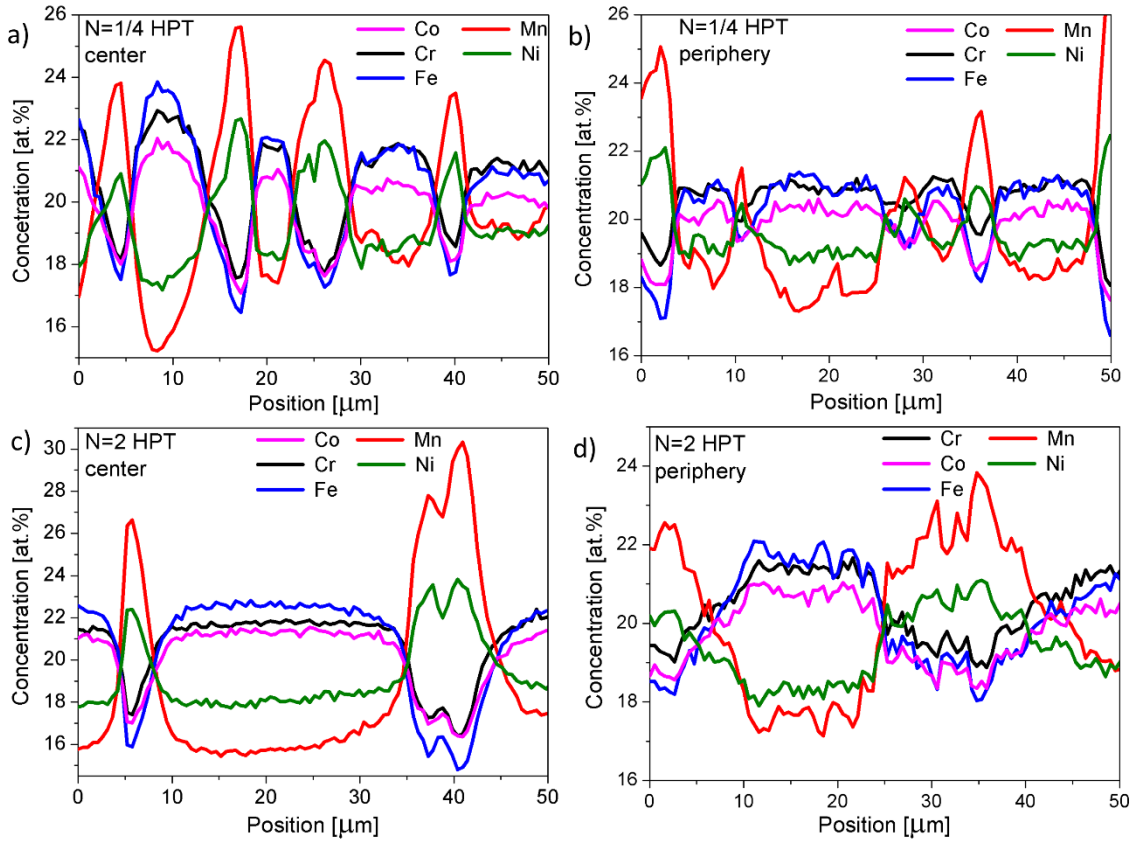

Fig. 3.27: The spatial distribution of the constituents in (a) the center and (b) the periphery of the CoCrFeMnNi HEA disk processed for ¼ turn and in (c) the center and (d) the periphery for 2 turns of HPT.

3.3.3 Defect structure of the HPT-processed HEA Samples from XLPA

The lattice defect structure in the center and the peripheral parts of the HPT-processed disks was studied by XLPA. The diffraction profiles were evaluated by the CMWP method [113]. It is noted that the size of the X-ray beam spot on the sample surface was about 1×0.3 mm^2, as shown in Fig. 3.28. Therefore, the results obtained in the disk center should be considered as an average for distances from the center between -0.5 and 0.5 mm. At the periphery, the XLPA measurement was carried out at 1 mm from the edge, i.e., at a distance of 4 mm from the disk center.

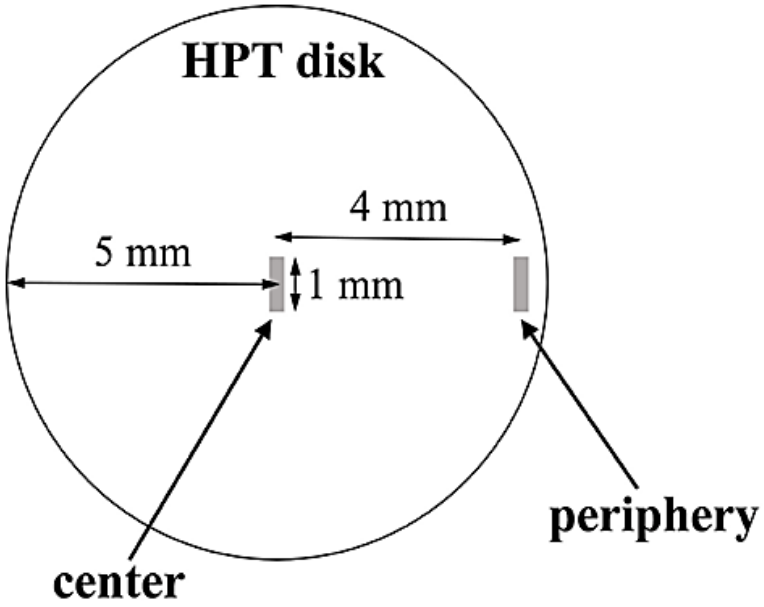

Fig. 3.28: Schematic depiction of the X-ray beam spot on the HPT-processed disks.

The initial as-cast CoCrFeMnNi HEA exhibited broader X-ray diffraction peaks than the profiles measured on a standard LaB_6 material. Most probably, this broadening is caused by the chemical inhomogeneities in the present as-cast HEA sample (see Fig. 3.22d). The heterogeneous chemical composition yields a variation in the lattice spacings which leads to an X-ray diffraction profile broadening even in the as-cast HEA sample before HPT. As the EDS analysis shows, the magnitude of the concentration fluctuations do not decrease during HPT, therefore the chemical inhomogeneities alone would have caused similar diffraction peak broadening for the HPT-processed samples as in the initial state. However, in addition to this effect the peaks measured on the HPT disks was also broadened due to the increase of the lattice defect (e.g., dislocations and twin faults) density and the reduction of the diffraction domain size. The diffraction peak caused by these effects can be referred to as the microstructural profile. Since only moderate chemical heterogeneities were observed in the present HEA samples, therefore it was assumed that the microstructure is not influenced by the slightly different chemical compositions in the various volumes of the material. With this condition, the microstructural X-ray diffraction profile components scattered from the different regions with various concentrations have the same profile shape except that their positions and intensities are different due to the various lattice spacings and volumes.

Fig. 3.29 shows schematically how these profile components build up the measured diffraction peak. Accordingly, the total intensity profile ($I(\kappa)$) can be expressed as:

$$I(\kappa) = \int f(g) I^{ms}(\kappa - g) dg, \tag{3.7}$$

where κ and g are the modulus of the scattering and diffraction vectors, respectively (i.e., $\kappa = 2\sin\Theta/\lambda$ while $g = 2\sin\Theta_B/\lambda$ where Θ and Θ_B are the scattering and Bragg angles, respectively). $I^{ms}(\kappa - g)$ are the subprofiles caused by the microstructure and normalized to a unit peak intensity. $f(g)$ is the density distribution function of the diffraction vector caused by the chemical heterogeneities, which reflects the distribution of the lattice spacings (d) since $g = 1/d$. According to eq. (3.7), the total intensity can be given as:

$$I(\kappa) = f(\kappa) * I^{ms}(\kappa), \tag{3.8}$$

where $*$ represents convolution. If the instrumental effect is also taken into account, the diffraction peak profile can be obtained as:

$$I(\kappa) = I^{i}(\kappa) * f(k) * I^{ms}(\kappa), \tag{3.9}$$

where $I^{i}(\kappa)$ is the instrumental profile. As the lattice defect density in the coarse-grained initial as-cast material is negligible compared to the HPT-processed samples, the profiles measured for the initial specimen ($I^{init}(\kappa)$) gives $I^{i}(\kappa) * f(\kappa)$. Therefore, the total intensity is expressed as:

$$I(\kappa) = I^{init}(\kappa) * I^{ms}(\kappa) = I^{init}(\kappa) * I^{S}(\kappa) * I^{d}(\kappa) * I^{tf}(\kappa), \tag{3.10}$$

where $I^{S}(\kappa)$, $I^{d}(\kappa)$ and $I^{tf}(\kappa)$ are the intensity profiles for diffraction domain size, dislocations and twin faults, respectively. In the XLPA evaluation of the HPT-processed samples, the diffraction peaks were fitted by the convolution of the intensity profile measured on the initial sample and the peak functions calculated theoretically for the effects of the diffraction domain size, dislocations and twin faults. In this evaluation, it is assumed that HPT processing does not produce a considerable reduction in the concentration fluctuations, in accordance with the

EDS measurements, i.e., the profile measured on the initial specimen is a good approximation for $I^i(\kappa) * f(\kappa)$ in the HPT-processed samples as well.

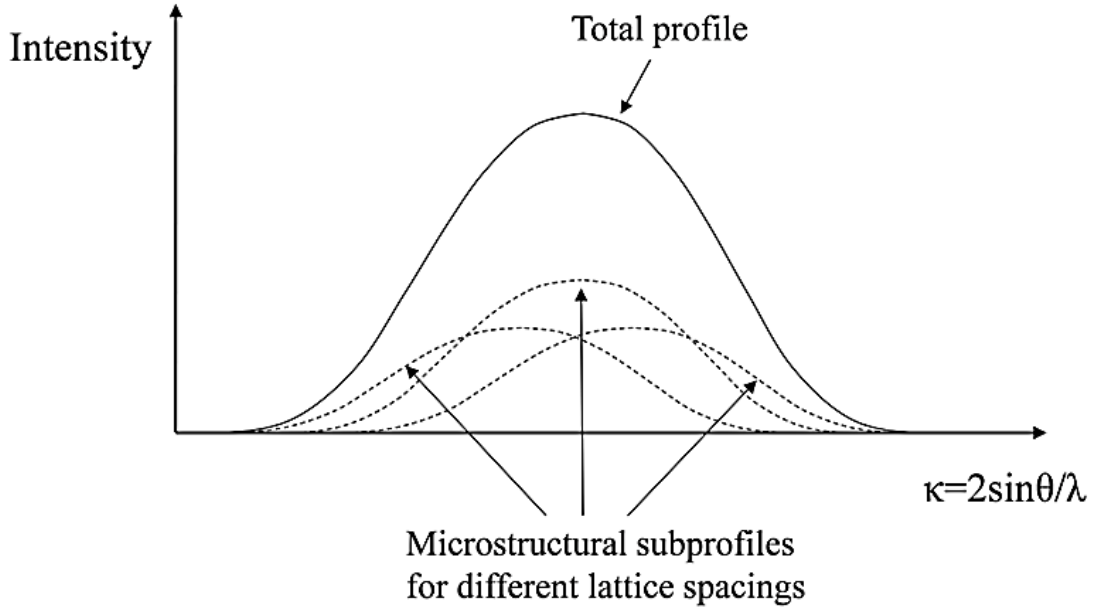

Fig. 3.29: Schematic showing that the total diffraction profile can be visualized as a sum of individual microstructural profiles scattered from regions with different lattice spacings. κ is the modulus of the scattering vector.

Fig. 3.30a shows reflection *200* for the initial material and the two HPT-processed states for the lowest (in the center of the disk processed for 1/4 turn) and the highest (at the periphery of the disk processed for 2 turns) imposed strains. The peak broadening of the initial sample is caused by the instrumental broadening and the chemical heterogeneities, as discussed above. The latter effect yielded a slightly asymmetric peak shape, as revealed in Fig. 3.30a. HPT processing led to a significant increase in the profile breadth even in the center of the disk processed for 1/4 turn. The peak broadening further increased for the periphery after 2 turns due to the much larger deformation. The dependence of the peak breadths on the diffraction order (i.e., on the indices *hkl*) can be visualized by plotting the integral breadth of the profiles (the total area under the peak divided by the peak height) as a function of the modulus of the diffraction vector, g (Williamson-Hall plot) [100,101]. Fig. 3.30b shows Williamson-Hall plots for the initial material, the center of the disk processed for 1/4 turn and the periphery of the disk processed for 2 turns. The

significantly non-monotonous variation of the integral breadth as a function of *g* for the HPT-processed samples is caused by the lattice defects, such as dislocations and twin-faults.

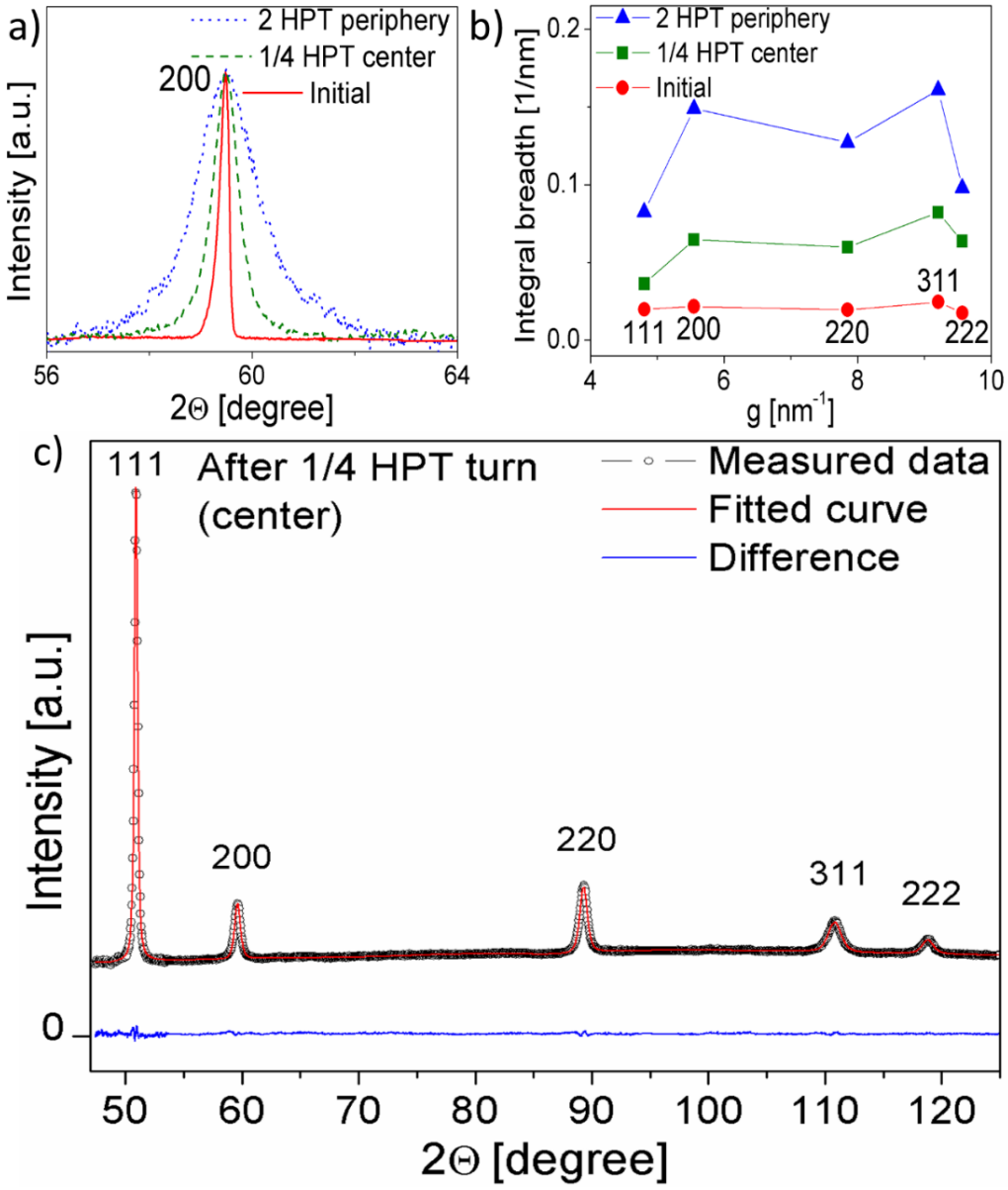

Fig. 3.30: (a) Reflection *200* for the initial material, as well as for the center and the periphery, of the disks processed for 1/4 and 2 turns of HPT, respectively. (b) the integral breadth versus the momentum of the diffraction vector, *g* (Williamson-Hall plot), for the initial material, as well as for the center and the periphery of the disks processed for 1/4 and 2 turns of HPT, respectively. (c) CMWP fitting for the center of the disk processed by 1/4 turn.

For dislocations with mixed edge/screw character, the breadths of *200*, *220* and *222* reflections are close to each other, while the width of *311* reflection is much larger [108]. This can be observed for the measurement obtained at the center of the disk processed for 1/4 turn. At the same time, the relatively large peak breadth of reflection *200* for the periphery of the disk processed for 2 turns suggests considerable twin-fault probability. For dislocations, the dependence of peak broadening on the reflection indices *hkl* can be taken into account by the average contrast factors. The average contrast factors for reflection *hkl*, $\overline{C}_{hkl}$, can be calculated numerically from the anisotropic elastic constants of the crystal [108]. The values of the elastic constants c_{11}, c_{12} and c_{44} are 172, 108 and 92 GPa, respectively, for the present HEA composition [144]. The average contrast factor can be calculated using eq. (3.2). The values of $\overline{C}_{h00}$ for edge and screw dislocations were calculated as 0.278 and 0.283, respectively, using program ANIZC [103]. The values of q for edge and screw dislocations were obtained as 1.5 and 2.3, respectively. Using the average contrast factors, the diffraction domain size, the dislocation density and the twin fault probability can be determined by fitting the calculated theoretical patterns to the experimental diffractograms using the CMWP procedure [99,119]. Fig. 3.30c shows a CMWP fitting for the center of the disk processed by 1/4 turn.

The average diffraction domain size, dislocation density and twin fault probability determined for the center and the periphery of the disks processed by 1/4, 1/2, 1 and 2 turns of HPT are listed in Table 3.4. It can be seen that the dislocation density is very large (~43×10^{14} m^{-2}) even in the center of the disk processed by 1/4 turn, while the grain structure was only slightly refined (the grain size decreased from ~60 μm to ~33 μm as shown by the EBSD study in section 3.3.2). The dislocation density increased with increasing numbers of HPT turns up to 1 revolution in both the center and the periphery of the disks. Between 1 and 2 turns only a slight difference between the dislocation density values was observed. The maximum dislocation densities with the values of ~126×10^{14} m^{-2} and ~194×10^{14} m^{-2} were measured in the center and the periphery of the disk processed for 2 turns, respectively. It can be seen from Table 3.4 that the difference between the

dislocation densities in the center and the periphery remained significant even after 2 turns of HPT, and this is similar to the hardness values presented in the next section.

For the center parts of all disks and also in the peripheries after 1/4 and 1/2 turns, the twin fault probability remained under the detection limit of XLPA (about 0.1% which corresponds to a twin fault spacing of ~200 nm). This observation is not in contradiction with the detection of twin faults in the EBSD images taken in the centers of the disks processed by 1 and 2 turns (for 1 turn see Fig. 3.24d) since the twin fault spacing is ~3 μm which is much larger than the upper limit of detection in XLPA. However, considerable twin fault probability values (β) of ~2.2% and ~2.7% were observed in the peripheral parts of the disks processed by 1 and 2 turns, respectively. These values correspond to a mean twin fault spacing of about 8-10 nm which is in accordance with the twin fault spacing observed by TEM (see section 3.3.2). The twin fault spacing can be calculated from β as $100 \cdot d_{111}/\beta$ where d_{111} is the lattice spacing for planes {*111*}. The deviation of the twin fault spacing determined by TEM from the value obtained by XLPA can be attributed to the much larger volume studied by the latter method. The high twin fault probability at the periphery of the disk processed by 2 turns is in accordance with the relatively large breadth of reflection *200* in the Williamson-Hall plot (see Fig. 3.30b) as discussed above.

The diffraction domain size is very small (~51 nm) in the center of the disk processed by 1/4 turn. This value is about three orders of magnitude smaller than the grain size measured by EBSD. The difference between the diffraction domain size obtained by XLPA and the grain size determined by microscopic methods in SPD-processed materials is a well-known phenomenon. The diffraction domains are equivalent to the volumes scattering X-rays coherently. Dislocation patterns inside the grains may break the coherency of X-rays. Low-angle grain boundaries and dipolar dislocation walls are typical examples which fragment grains into small diffraction domains. The high dislocation density yielded a small diffraction domain size in the center of the HEA sample processed by 1/4 turn. With increasing distance from the center and the numbers of turns, the grain size was strongly reduced, while

only a small decrease in the diffraction domain size was detected. Therefore, the difference between the grain and diffraction domain sizes decreased with increasing strain during HPT. For the peripheries of the disks processed by 1/2, 1 and 2 turns, the grain and diffraction domain sizes agree within the experimental error. The smallest grain and diffraction domain sizes were 20-30 nm, which were achieved after 1/2 turn at the periphery of the HPT disk.

The grain size determined by EBSD or TEM, the diffraction domain size and the dislocation density obtained by XLPA were plotted in Figs. 3.31a, b and c, respectively, as a function of shear strain given as $\gamma = 2\pi rN/h$, where r, h and N are the distance from the center, the thickness of the HPT processed disk and the number of turns, respectively. It should be noted that, due to the 1 mm height of the X-ray spot on the illuminated surface, for the diffraction domain sizes and the dislocation densities determined in the center of the disks the shear strain was obtained by averaging the strain values obtained for distances from the disk center between -0.5 and 0.5 mm. For the dislocation densities and diffraction domain size measured near the periphery, the shear strain was determined at 4 mm from the disk center (see Fig. 3.28). Fig. 3.31 shows that the grain and the diffraction domain sizes saturated even at the shear strain of ~10 while the dislocation density reached its maximum value only at the shear strain of ~40. It is noted that although the nominal value of the shear strain is zero in the center of the disks, the grain size decreased considerably with increasing the number of turns (see Table 3.4). This discrepancy can be explained by the spread of plastic deformation into the center from the neighbouring regions due to the stress field of dislocations developed out of the disk center. This induced plasticity causes grain refinement even in the disk center.

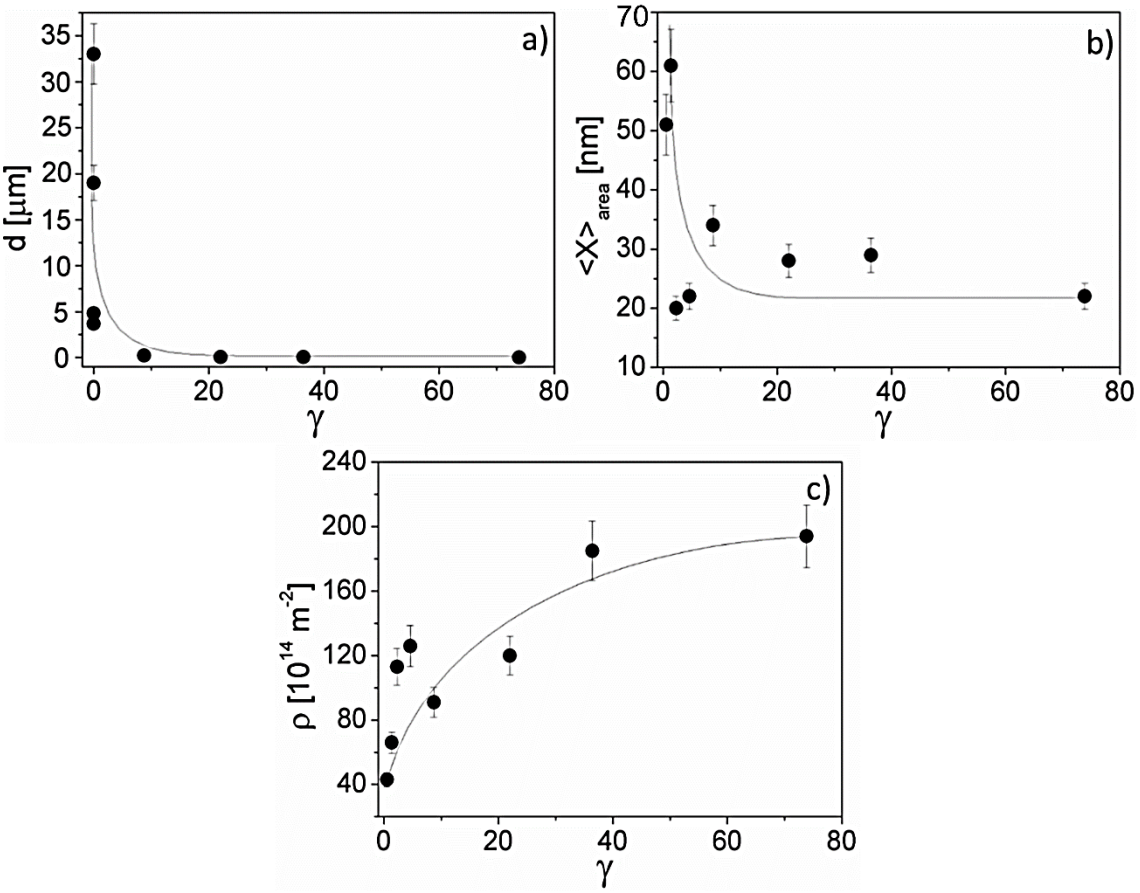

Fig. 3.31: (a) The grain size determined by EBSD or TEM, (b) the diffraction domain size and (c) the dislocation density obtained by XLPA as a function of shear strain imposed by HPT.

3.3.4 Hardness Evolution During HPT

Fig. 3.32a shows the hardness evolution along the disk diameter as a function of the number of rotations. The undeformed specimen has a hardness of about 1440 MPa. After 1/4 turn of HPT, there is a large gradient in the hardness along the disk radius. In the center and the periphery, the hardness values are ~2400 and ~4860 MPa, respectively. Further straining up to 1/2 turn yielded a slight hardening in both the center and the periphery. In addition, the hard regions at the periphery expanded towards the disk center as shown in Fig. 3.32a. Between 1/2 and 1 turn of HPT, the hardness increased from ~2520 MPa to ~3180 MPa in the center of the disks. At the

periphery, the hardness was enhanced to ~5220 MPa. Moreover, the hard regions expanded further towards the disk center. Between 1 and 2 turns of HPT, only a slight increase of the hardness was detected. The maximum value of the hardness was measured at the periphery of the disk processed by 2 turns (~5380 MPa). However, even after 2 turns of HPT a relatively low hardness remained in the disk center. It is probable that higher numbers of turns may yield a complete saturation of hardness with a large value along the disk radius.

Fig. 3.32b shows that the hardness values measured at different distances from the disk centers for various numbers of turns follow a unified trend if they are plotted as a function of the shear strain. Specifically, this trend shows the general hardness evolution associated with strain hardening observed in many commercial purity metals and simple alloys after HPT processing. A recent report summarizes the different models of hardness evolution in various metallic materials processed by HPT [145]. It should be noted that the hardness increased in the disk center with increasing number of turns, although the nominal shear strain is zero there. This can be explained by the spread of plasticity from the neighbouring regions into the disk center (see section 3.3.3).

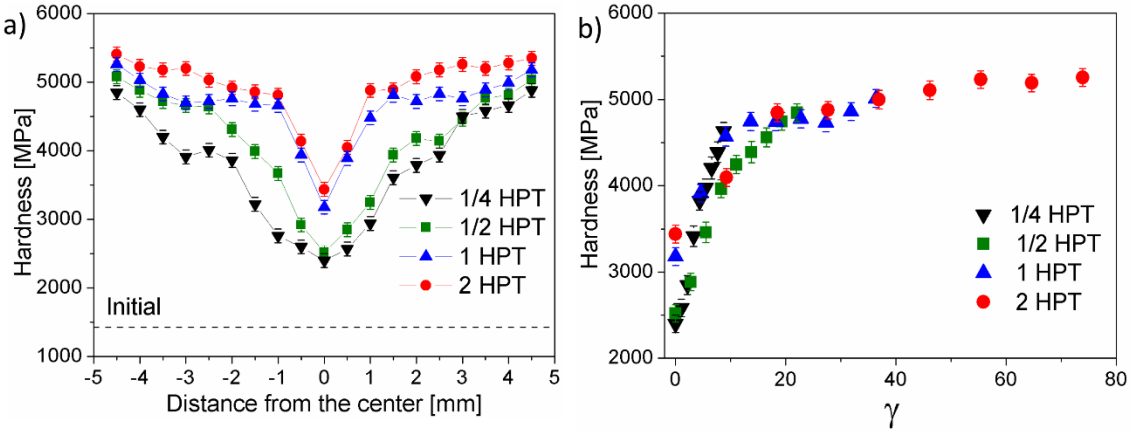

Fig. 3.32: The Vickers microhardness versus the distance from the center (a) and the shear strain (b) for the disks processed by HPT for 1/4, 1/2, 1 and 2 turns. The hardness plotted in (b) was calculated as the average of the two values obtained for the same distance from the center. The dashed line in (a) shows the average hardness for the initial sample without HPT. The error bars indicate the uncertainties in the hardness values.

3.3.5 Discussion of the Evolution of Lattice Defect Structure in CoCrFeMnNi HEA During HPT

It was found for the present CoCrFeMnNi HEA that for low shear strains of HPT (e.g., in the center part of the disk processed by ¼ turn) the dislocation density increased to very high values (10^{15}-10^{16} m^{-2}) while the grain size was only slightly refined. This observation suggests that the rate of increase of the dislocation density is higher than for the grain refinement. A fast increase in the dislocation density without considerable grain refinement was also observed during compression of another HEA with the equimolar composition of TiZrHfNbTa in a earlier work [R1]. The high dislocation densities in plastically deformed HEAs even at low strains can be explained by a reduced annihilation rate of dislocations during plastic deformation which may be caused by the high stress required for dislocation motion in highly-alloyed HEA materials. In addition, for the present CoCrFeMnNi HEA the low stacking fault energy (SFE, 19 mJ/m^2 [146]) also contributed to the very high dislocation density. The low SFE results in a dissociation of dislocations into partials which obstructs the annihilation mechanisms of dislocations (e.g., cross slip and climb) [147]. Therefore, both the high concentrations of the different alloying elements and the low SFE are the reasons of the very high dislocation density ($\sim 194 \times 10^{14}$ m^{-2}) after 2 turns of HPT. In addition, the high twin fault probability inside the nanograins after 1-2 turns (2.2-2.7%) was also caused mainly by the low SFE of this HEA. A similar twin fault probability (about 2%) was also obtained for a HPT processed 4N purity Ag with a similar SFE ($\sim$16 mJ/m^2) [148]. The saturation dislocation density achieved in the Ag sample ($\sim 154 \times 10^{14}$ m^{-2}) was also close to the value measured for the present HEA material ($\sim 194 \times 10^{14}$ m^{-2}). Therefore, it seems that the low SFE of CoCrFeMnNi HEA is a deterministic factor in the evolution of the defect structure during HPT. It is noted that a recently published study [149] showed that in CoCrFeMnNi HEA, the value of SFE may have a spatial dependence

due to the variation of local chemical composition. This effect yields different degree of dislocation dissociation into partials. It was revealed that in CoCrFeMnNi HEA deformed to a plastic strain of 3.7% the splitting distance between partials in dissociated dislocations varies between 1 and 9 nm. The mean and the standard deviation of splitting distance were 5 and 2 nm, respectively. These values are in reasonable agreement with the splitting distances in Ag (~2.5 and ~6.3 nm for screw and edge dislocations, respectively [95]) with similar SFE. It is also noted that the saturation grain size for HPT-processed CoCrFeMnNi HEA (~30 nm) is much smaller than that for Ag (~200 nm) with similar SFE. This indicates that SFE is not a deterministic factor in the development of the minimum grain size during HPT at room temperature. Rather, the higher melting temperature of CoCrFeMnNi HEA (~1660 K) compared to Ag (~1235 K) caused the smaller saturation grain size due to the more hindered recrystallization during SPD-processing.

It should be noted that our results are in accordance with former studies on HPT-processed CoCrFeMnNi HEA. In the investigation performed by Schuh et al. [143] the applied HPT pressure was higher (7.8 GPa), while the rate of deformation was lower (0.2 rpm) than in our experiments (3.0 GPa and 1 rpm). Despite the different HPT conditions, the saturation grain size (~50 nm) and hardness (~5100 MPa) were very close to the values obtained in our study (~30 nm and ~5380 MPa). In addition, the threshold shear strain for hardness saturation was observed as ~50 in Ref. [143] which is very close to the value determined in this study (~45, see Fig. 3.32b). Concerning lattice defects formed during HPT, both the former and the present studies revealed the significance of twinning in plastic deformation of CoCrFeMnNi HEA even for low number of turns (see Fig. 3.23b). Considerable twin formation was also observed in cold rolled and tensile tested CoCrFeMnNi HEA [157,158]. The critical shear strain for twinning was determined as ~0.5 [150,158], therefore the observation of significant twinning even at the half-radius of the disk processed for 1/4 turn (where the shear strain is ~5.6) is in accordance with the results presented in the literature. XLPA was unable to observe twin faults for low number of HPT turns since this method can detect twin boundaries only if their average spacing is lower than ~200 nm. Therefore, XLPA gives considerable twin fault probability only for the periphery of the disks processed by 1 and 2 turns,

despite the significant twinning for lower numbers of turns. It should also be noted that the lower twin fault probability for small numbers of HPT turns does not mean necessarily a lower contribution of twinning to plasticity, as the shear strain caused by twinning is determined by the volume of the twinned regions and not by the amount of twin boundaries.

3.3.6 Strengthening Mechanisms in the HPT-processed CoCrFeMnNi HEA

In order to reveal the underlying strengthening mechanisms in the present HEA processed by HPT, the yield strength was estimated as one-third of the hardness in the center and the periphery and then compared with the values calculated as the sum of the dislocation and grain size hardening contributions. It is noted that the ratio of the hardness and the yield strength depends on the work hardening behavior of the material as the hardness measurement itself causes a plastic strain of 8% in the sample. Therefore, one-third of the hardness gives the flow stress at the plastic strain of 8% instead of the yield strength. However, for severely deformed materials additional straining after SPD usually yields only a slight hardening, thus one-third of the hardness is an acceptable approximation of the yield strength. In the following, the strength contributions of dislocations and grain size will be calculated. The yield strength caused by dislocations can be obtained from the Taylor equation (see eq. (3.7)). According to a previous study on a CoCrFeMnNi HEA [151,160], the value of the shear modulus was chosen as ~80 GPa in the Taylor equation. The influence of the grain size on the yield strength can be described by the Hall–Petch relationship [161,162]:

$$\sigma_{HP} = \frac{k}{\sqrt{d}}, \tag{3.11}$$

where k is a constant depending on the investigated material and d is the average grain size.

Assuming a simple linear additivity of the hardening contributions of dislocations and grain size, the yield strength can be calculated as:

$$\sigma_y = \sigma_0 + \sigma_{Taylor} + \sigma_{HP}, \quad (3.12)$$

where σ_0 is the friction stress describing the resistance of the defect-free lattice against plastic deformation. The value of σ_0 was taken as ~200 MPa in accordance with previous studies on the CoCrFeMnNi HEA [79,151,163]. In eqs. (3.7), (3.11) and (3.12), there are two unknown parameters for the present HEA, namely α and k in the Taylor and Hall-Petch equations, respectively. These values were determined by searching for the best agreement between the estimated yield strength and the values calculated from eq. (3.12) for the center and the periphery of the disks processed by 1/4, 1/2, 1 and 2 turns (thus altogether eight studied locations). It should be noted that, due to the 1 mm height of the X-ray spot on the illuminated surface, the estimated yield strength was obtained by averaging the strength values obtained for distances from the disk center between -0.5 and 0.5 mm. At the periphery, the strength determined at +/- 4 mm from the disk center was taken as the estimated value (see Fig. 3.28). It is also noted that for the periphery of the disks processed for 1 and 2 turns the grains were highly twinned as indicated by the XLPA and TEM observations, therefore the twin boundary spacing was substituted for the grain size in the Hall-Petch relationship. The twin boundary spacing was calculated from the twin fault probability determined by XLPA using the equation given in section 2.3.4 on page 35. In former studies [164,165], it has been shown that the same value of k can be used in the Hall-Petch relationship for both the grain size and the twin boundary spacing. Although, twin boundaries were also observed inside the coarse grains by EBSD (e.g., see Fig. 3.24d), they were included in the HAGBs and therefore their effect was taken into account in the calculation of the average grain size.

The difference between the estimated and calculated yield strength was minimised by varying the values of α and k using the method of least squares. This procedure gave 0.16 ± 0.02 and 21 ± 2 MPa·μm$^{1/2}$ for α and k, respectively. With

these values, a relatively good agreement between the estimated and calculated yield strength values was achieved, as shown in Fig. 3.33.

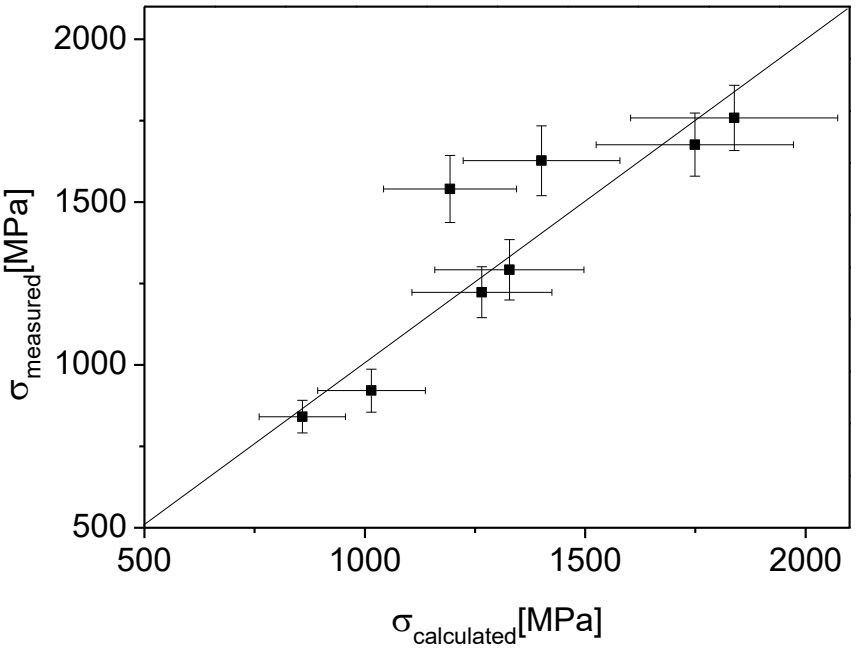

Fig. 3.33: The yield strength estimated as one-third of the hardness versus the values calculated from eq. (3.12) for the center and the periphery of the disks processed by 1/4, 1/2, 1 and 2 turns.

The estimated and the calculated yield strength values are listed in Table 3.5. The contributions of dislocations and grain/twin size to the yield strength are also listed. It can be seen that dislocations have a much higher hardening effect than the grain/twin size. The dislocation hardening parameter α for the present HPT-processed HEA samples has a relatively low value compared to other metals. For example, it was reported that α varies between 0.17 and 0.3 for Cu deformed at different strains [158]. A similar range was observed for SPD-processed fcc metals with different stacking fault energies [159]. The smaller values of α were obtained for materials with lower SFEs. For instance, for ultrafine-grained Ag processed by equal-channel angular pressing the value of α was 0.17 which is very close to the value determined for the CoCrFeMnNi HEA in this study. In addition, the SFE values are also similar: 16 [159] and 19 mJ/m^2 [146] for Ag and the CoCrFeMnNi HEA,

respectively. As discussed earlier [159], the low SFE results in a higher degree of dislocation dissociation, which impedes the clustering of dislocations. It was shown previously [160] that the less clustered the dislocation structure, the lower the value of α. Therefore, the low SFE of the CoCrFeMnNi HEA appears to make a significant contribution to the relatively small value of α.

Table 3.5: The contributions of dislocations (σ_{Taylor}) and grain/twin size (σ_{HP}) to the yield strength calculated from the Taylor and Hall-Petch formulas according to eqs. (3.7) and (3.11), respectively, and the value of the friction stress (σ_0). The calculated yield strength ($\sigma_{calculated}$) was obtained as the sum of σ_0, σ_{Taylor} and σ_{HP}, while the estimated values ($\sigma_{estimated}$) were determined as one-third of the hardness. The corresponding shear strain values (γ) are also shown. The calculation details of the shear strain is given in the last paragraph of section 3.3.3.

Location	γ	σ_{Taylor} [MPa]	σ_{HP} [MPa]	σ_0 [MPa]	$\sigma_{calculated}$ [MPa]	$\sigma_{estimated}$ [MPa]
1/4 turn, center	0.55	654 ± 97	4 ± 1	200	858 ± 98	841 ± 50
1/4 turn, periphery	8.7	949 ± 145	44 ± 6	200	1193 ± 151	1540 ± 103
1/2 turn, center	1.4	810 ± 121	5 ± 1	200	1015 ± 122	921 ± 66
1/2 turn, periphery	22.1	1092 ± 162	109 ± 16	200	1401 ± 178	1627 ± 107
1 turn, center	2.3	1056 ± 158	10 ± 1	200	1266 ± 159	1223 ± 78
1 turn, periphery	36.4	1357 ± 196	192 ± 28	200	1749 ± 224	1676 ± 97
2 turn, center	4.6	1117 ± 167	11 ± 2	200	1328 ± 169	1292 ± 93
2 turn, periphery	73.9	1387 ± 203	251 ± 32	200	1838 ± 235	1758 ± 100

3.3.7 The Influence of Chemical Heterogeneities on the Local Mechanical Behavior

Fig. 3.27 shows that the HPT-processed samples have chemical inhomogeneities. The effect of these heterogeneities on the local mechanical behavior was studied by pillar compression at the periphery of the disk processed by 2 turns of HPT. Fig. 3.34 shows EDS maps for the five constituents at the periphery of the CoCrFeMnNi HEA disk processed by HPT 2 turns. These maps reveal inhomogeneities in the concentrations of the five elements. The bright and dark regions in Fig. 3.34 indicate enrichment and depletion of the constituents, respectively. It can be seen that Co/Cr/Fe and Mn/Ni elements behave in a complementary way. The dashed and solid white circles in Fig. 3.34 indicate Co/Cr/Fe-rich and Mn/Ni-rich regions, respectively. The EDS maps were used to select regions where micropillars were fabricated in order to study the effect of chemical inhomogeneities on the mechanical behavior. The average chemical composition for the Co/Cr/Fe-rich regions studied by pillar compression was 21.0% Co, 21.9% Cr, 22.3% Fe, 16.3% Mn and 18.5% Ni. At the same time, for the Ni/Mn-rich regions the average chemical composition was 16.9% Co, 17.4% Cr, 16.3% Fe, 25.3% Mn and 24.1% Ni.

Micropillars were fabricated in the Co/Cr/Fe-rich and Mn/Ni-rich regions using the FIB technique and then compressed using a flat-end diamond punch under a load-controlled condition. Fig. 3.35a shows a typical micropillar fabricated in a Co/Cr/Fe rich region before compression. In section 3.3.2 it was shown that the HPT-processed disk exhibited a texture-free microstructure with a very fine grain size (~27 nm). The dimensions of the pillars were selected as 1-2 μm, which is larger than the grain size in order to avoid any effect of the crystallographic orientation on the compression results. In addition, the pillar size could not be much higher than the size of the volume studied by EDS (about 1 μm for the constituents of CoCrFeMnNi HEA). After compression, the height of the pillars was reduced from ~2 to ~1.8 μm, which corresponds to a residual strain of about 10% (see Fig. 3.35b).

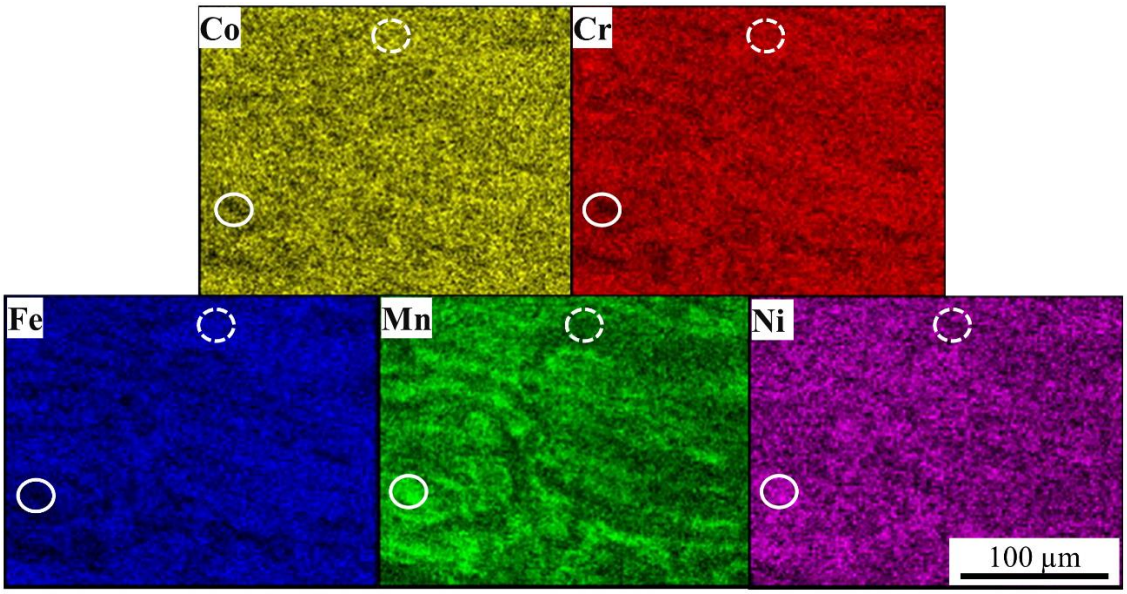

Fig. 3.34: Elemental maps for the CoCrFeMnNi HEA obtained by EDS. The brighter the colour, the higher the concentration. The dashed and solid white circles indicate Co/Cr/Fe-rich and Mn/Ni-rich regions, respectively, where micropillar compression tests were carried out.

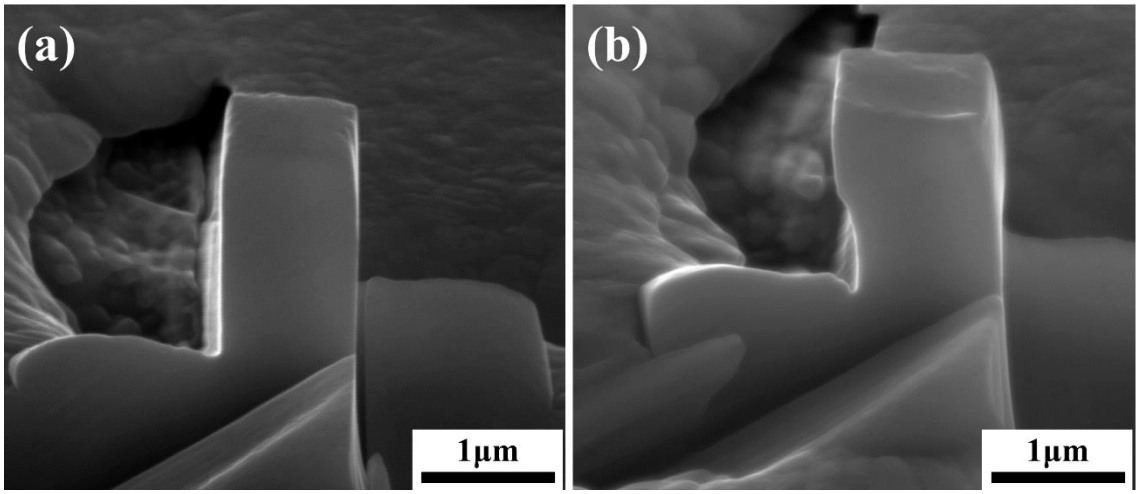

Fig. 3.35: A micropillar fabricated in a Co/Cr/Fe rich region (a) before and (b) after compression.

Fig. 3.36 shows typical engineering stress-strain curves obtained by compression of micropillars for the Co/Cr/Fe-rich and the Mn/Ni-rich regions. The stress was calculated as the ratio of the applied load and the initial area of the top surface of the micropillars determined by SEM. The strain was obtained as the ratio

of the indenter displacement and the initial height of the micropillars. The experiments revealed that a saturation of the flow stress was achieved at a total strain of ~13%. The micropillar compression tests show that the saturation flow stress for the Mn/Ni-rich regions (1594 ± 65 MPa) agrees with the value determined for the Co/Cr/Fe-rich regions (1475 ± 71 MPa) within the experimental error. Therefore, the chemical heterogeneities have only a marginal effect on the local flow stress of this HEA.

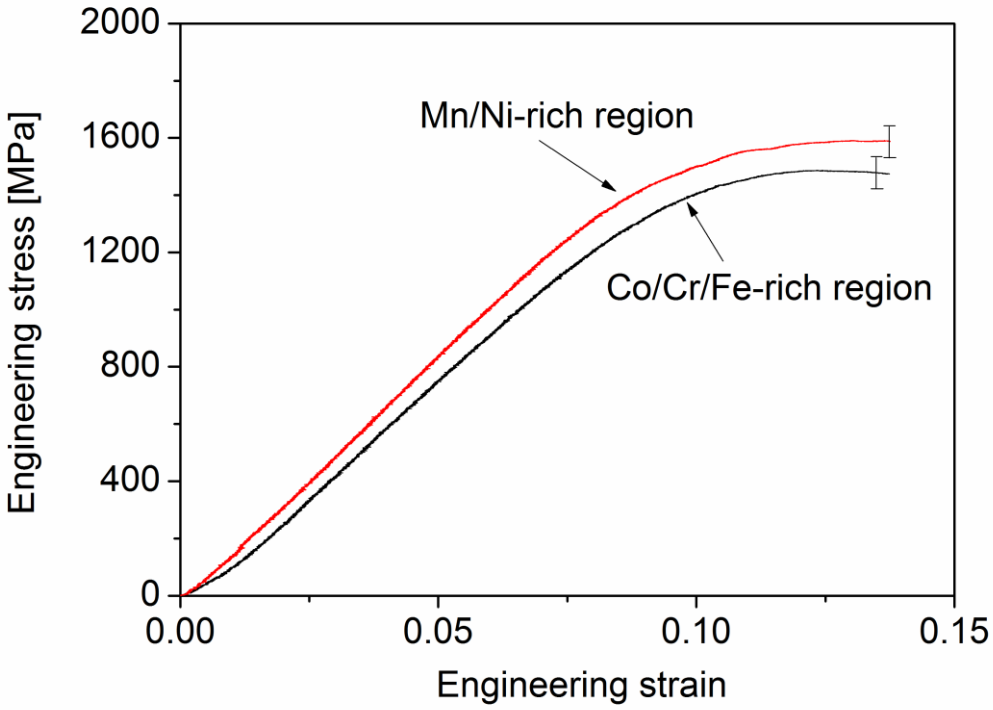

Fig. 3.36: Typical engineering stress-strain curves obtained by pillar compression for the Co/Cr/Fe-rich and the Mn/Ni-rich regions. The bars indicate the errors of the flow stress values determined from compressions of different pillars.

It has been shown for other materials that a decrease in the size of the pillars led to a change in strength (referred to as "size effect") [161]. This effect can be checked for the present study if the flow stress measured by pillar compression is compared with the macroscopic flow stress. The average of the saturation flow stress values determined by pillar compression for the different regions was 1535 ± 68 MPa. This value was compared to the macroscopic flow stress determined as

one third of the macrohardness determined by Vickers indentation. The Vickers hardness was measured using a load of 500 g, which gave an indent size of ~40 μm. Considering the length scale of the chemical heterogeneities (see Fig. 3.34), the hardness value measured with 500 g reflects the average behavior of the material. The flow stress determined as one third of the hardness was 1758 ± 100 MPa which is only slightly higher than the average saturation flow stress determined by pillar compression. This result suggests that the flow stress values obtained from the micropillar compression reflect the macroscopic behavior, so that the "size effect" is negligible. This observation is in line with a former study which revealed the lack of "size effect" for nanocrystalline Cu with the grain size of ~30 nm even if the pillar size was only ~0.4 μm [162].

3.3.8 Summary

In this chapter, the evolution of the defect structure, grain size and hardness during HPT processing of an equiatomic CoCrFeMnNi HEA was studied. In the initial sample, the average grain size was determined as ~60 μm. After 2 turns of HPT, the grain size was refined to ~30 nm at the periphery of the disk. At the same time, in the disk center the grain size was reduced only to ~4 μm after 2 turns, indicating a high sensitivity of grain refinement on the gradient in shear strain along the disk radius. It has been shown that the dislocation density increased rapidly with increasing numbers of turns in HPT processing. After 1/4 turn, high dislocation densities with the values of ~43 and ~91×10^{14} m^{-2} were detected in the center and the periphery of the HPT disk, respectively. Further straining up to 2 turns increased the dislocation density to ~126 and ~194×10^{14} m^{-2} in the center and the periphery, respectively. The high shear strains at the edge of the disks processed by 1 and 2 turns of HPT yielded large twin fault probabilities of ~2.2-2.7%. The low SFE of the equiatomic CoCrFeMnNi HEA is a deterministic factor in the development of the very high defect density (dislocations and twin faults) during HPT. At the same time, the minimum grain size in the HPT-processed CoCrFeMnNi HEA was much smaller

than in Ag with very similar SFE due to the significantly higher melting point of the HEA material.

Similar to the microstructure, there was a large gradient in the hardness along the disk radius. After 1/4 turn of HPT, the hardness increased from ~1440 MPa to ~2400 and ~4860 MPa in the center and the periphery of the disk, respectively. Even after 2 turns of HPT a large gradient in hardness remained along the disk radius. The maximum hardness value at the periphery of the disk processed by 2 HPT turns was measured as ~5380 MPa. A good correlation between the yield strength estimated as one-third of the hardness and the calculated values was achieved using $\alpha = 0.16$ and $k = 21$ MPa·μm$^{1/2}$ in the Taylor and Hall-Petch terms of yield strength, respectively. The relatively small value of α was attributed to the low SFE of the CoCrFeMnNi HEA since the clustering of highly dissociated dislocations in low SFE materials is hindered and the less clustered dislocation structure usually yields a small value of α in the Taylor equation.

In addition, the local mechanical behavior was studied by micropillar compression test. Co/Cr/Fe-rich and Mn/Ni-rich regions were found in the nanocrystalline $Co_{20}Cr_{20}Fe_{20}Mn_{20}Ni_{20}$ HEA. In these regions, micropillars were fabricated and compressed. The heights and the widths of the pillars were 2 and 1 μm, respectively, which are in accordance with the length scale of the chemical inhomogeneities and the grain size of the HEA. Only slight differences were found between the stress-strain curves recorded in Co/Cr/Fe-rich and Mn/Ni-rich volumes, suggesting that the chemical heterogeneities in the $Co_{20}Cr_{20}Fe_{20}Mn_{20}Ni_{20}$ HEA have only a negligible effect on the local mechanical behavior. The average saturation flow stress obtained by pillar compression was 1535 ± 68 MPa which is only slightly smaller than the value determined as one third of the macrohardness (1758 ± 100 MPa). This observation suggests a negligible size effect in the present micropillar compression experiments.

4 New Scientific Results

The goal of my PhD work was to study the defect structure in plastically deformed HEAs with different chemical compositions and crystal structures, such as the equimolar $Ti_{20}Zr_{20}Hf_{20}Nb_{20}Ta_{20}$ with bcc structure, the Ti-rich $Ti_{35}Zr_{27.5}Hf_{27.5}Nb_5Ta_5$, which exhibited a martensitic phase transition from bcc to orthorhombic structure, and the equimolar $Co_{20}Cr_{20}Fe_{20}Mn_{20}Ni_{20}$ with fcc structure. The research results are summarized in the following 8 thesis points which are listed in three groups in accordance with the three different materials.

1. $Ti_{20}Zr_{20}Hf_{20}Nb_{20}Ta_{20}$ HEA was compressed at room temperature to the plastic strains of 3, 10 and 20%. Additionally, two samples were impacted using a Hopkinson pressure bar at the initial impact velocities of 10 and 20 m/s up to the equivalent strains of 50 % and 130 %, respectively. The following results were obtained:

1.1. The elastic anisotropy factor of $Ti_{20}Zr_{20}Hf_{20}Nb_{20}Ta_{20}$ HEA was determined by an indentation method as 2.3 ± 0.2 which was required for the determination of the edge/screw character and the density of dislocations by XLPA. Using the obtained elastic anisotropy factor, the theoretical values of the parameter describing the dislocation character were determined for pure edge and screw dislocations. Comparing these values with the experimentally determined parameters, it was found that the screw character of dislocations became stronger with increasing strain during compression of $Ti_{20}Zr_{20}Hf_{20}Nb_{20}Ta_{20}$ HEA. This can be explained by the reduced mobility of screw dislocations compared to edge dislocations in bcc structures.

1.2. A high density of dislocations (10-15 $\times$ 10^{14} m^{-2}) was developed during compression even at moderate plastic strains (10-20%). In the impacted samples, the dislocation density was even higher with the values of about 47×10^{14} m^{-2} and 32×10^{14} m^{-2} for the velocities of 10 and 20 m/s, respectively. This can be attributed to the higher strain and strain rate applied during the impact test. The smaller dislocation density for the sample impacted at 20 m/s compared to that for 10 m/s can be explained by a possible recovery of the microstructure due to the annealing

of the material at high strain rates. The dislocation density obtained by XLPA was in accordance with the dislocation spacing observed in the TEM images.

1.3. The present HEA material has a high yield strength of about 890 MPa. The strain hardening during compression was caused by the increase of the dislocation density. The dislocation hardening parameter (α) has a relatively low value (~0.16) but it is still in the range determined for other bcc non-HEA metallic materials. It was found that the Peierls stress has the main component in the flow stress, and dislocation hardening has a lower contribution even for high dislocation densities.

2. The evolution of the phase composition, microstructure and hardness during plastic deformation of a Ti-rich HEA with the composition of $Ti_{35}Zr_{27.5}Hf_{27.5}Nb_5Ta_5$ was studied. The following results were obtained:

2.1. Due to processing by 1 turn of HPT, the initial grain size (~800 μm) was refined to ~200-1000 nm, irrespective of the location along the disk radius. In this Ti-rich HEA material, besides the refinement of the microstructure, a phase transition also occurred during HPT. The initial bcc phase was transformed into an orthorhombic structure throughout the disk. Very high dislocation densities were observed in both the center (~43×10^{14} m^{-2}) and the periphery (~103×10^{14} m^{-2}) of the HPT-processed disk. A very high hardness with the values between 3500-3900 MPa was measured on the HPT-processed sample, which changed only slightly along the disk radius in accordance with the microstructure observations. These results indicate a very early saturation of the microstructure and the hardness with increasing strain imposed in HPT-processing.

2.2. Complementary compression test revealed that the phase transformation during deformation starts with the formation of orthorhombic lamellae in the initial bcc grains. This grain morphology was inherited in the elongated grain shape in the HPT-processed disk. The phase transformation was nearly completed even at a strain of about 11.5%. The yield strength of the initial material was ~277 MPa, which is much smaller than one-third of the hardness (~1000 MPa) measured on the initial sample due to the strong strain hardening in the beginning of compression. The yield strength and the strain hardening were lower and higher,

respectively, for the Ti-rich HEA than in the case of the equimolar $Ti_{20}Zr_{20}Hf_{20}Nb_{20}Ta_{20}$ material.

3. The evolution of the defect structure, grain size and hardness during HPT processing of an equiatomic CoCrFeMnNi HEA was studied. The following results were obtained:

3.1. In the initial sample, the average grain size was determined as ~60 μm. After 2 turns of HPT, the grain size was refined to ~30 nm at the periphery of the disk. At the same time, in the disk center the grain size was reduced only to ~4 μm after 2 turns, indicating a high sensitivity of grain refinement on the gradient in shear strain along the disk radius. It has been shown that the dislocation density increased rapidly with increasing numbers of turns in HPT processing. After 1/4 turn, high dislocation densities with the values of ~43 and ~91 × 10^{14} m^{-2} were detected in the center and the periphery of the HPT disk, respectively. Further straining up to 2 turns increased the dislocation density to ~126 and ~194 × 10^{14} m^{-2} in the center and the periphery, respectively. The high shear strains at the edge of the disks processed by 1 and 2 turns of HPT yielded large twin fault probabilities of ~2.2-2.7%. It was revealed that the low SFE of the equiatomic CoCrFeMnNi HEA is a deterministic factor in the development of the very high defect density (dislocations and twin faults) during HPT. At the same time, the minimum grain size in the HPT-processed CoCrFeMnNi HEA was much smaller than in Ag with very similar SFE, due to the significantly higher melting point of the HEA material.

3.2. Similar to the microstructure, there was a large gradient in the hardness along the disk radius. The maximum hardness value at the periphery of the disk processed by 2 HPT turns was measured as ~5380 MPa. A good correlation between the yield strength estimated as one-third of the hardness and the calculated values was achieved using $\alpha = 0.16$ and $k = 21$ MPa·$\mu m^{1/2}$ in the Taylor and Hall-Petch terms of yield strength, respectively. The relatively small value of α was attributed to the low SFE of the CoCrFeMnNi HEA since the clustering of highly dissociated dislocations in low SFE materials is hindered and the less clustered dislocation structure usually yields a small value of α in the Taylor equation.

3.3. The local mechanical behavior in the Co/Cr/Fe-rich and Mn/Ni-rich regions was studied by micropillar compression. Only slight differences were found between the stress-strain curves recorded in the Co/Cr/Fe-rich and Mn/Ni-rich volumes, suggesting that the chemical heterogeneities in the $Co_{20}Cr_{20}Fe_{20}Mn_{20}Ni_{20}$ HEA have only a negligible effect on the local mechanical behavior. The average saturation flow stress obtained by pillar compression was 1535 ± 68 MPa which is only slightly smaller than the value determined as one third of the macrohardness (1758 ± 100 MPa). This observation suggests a negligible size effect in the present micropillar compression experiments.

5 Publications of the Author Related to This Thesis

R1. G. Dirras, J. Gubicza, A. Heczel, L. Lilensten, J.-P. Couzinie, L. Perriere, Y. Guillot, A. Hocini, Microstructural investigation of plastically deformed Ti20Zr20Hf20Nb20Ta20 high entropy alloy by X-ray diffraction and transmission electron microscopy, Materials Characterization 108 (2015), 1-7.

R2. G. Dirras, H. Couque, L. Lilensten, A. Heczel, D. Tingaud, J.-P. Couzinie, L. Perriere, J. Gubicza, I. Guillot, Mechanical behavior and microstructure of Ti20Hf20Zr20Ta20Nb20 high-entropy alloy loaded under quasi-static and dynamic compression conditions, Materials Characterization 111 (2016), 106-113.

R3. A. Heczel, L. Lilensten, J. Bourgon, L. Perrière, J.P. Couzinié, I. Guillot, G. Dirras, Y. Huang; T.G. Langdon, J. Gubicza, Influence of High-Pressure Torsion on the Microstructure and the Hardness of a Ti-Rich High-Entropy Alloy, Materials Science Forum 879 (2017), 732-737.

R4. A. Heczel, Y. Huang, T.G. Langdon, J. Gubicza, Investigation of Lattice Defects in a Plastically Deformed High-Entropy Alloy, Materials Science Forum 885 (2017), 74-79.

R5. A. Heczel, M. Kawasaki, J.L. Lábár, J. Jang, T.G. Langdon, J. Gubicza, Defect structure and hardness in nanocrystalline CoCrFeMnNi High-Entropy Alloy processed by High-Pressure Torsion, Journal of Alloys and Compounds 711 (2017), 143-154.

R6. A. Heczel, M. Kawasaki, D. Ugi, J. Jang, T.G. Langdon, J. Gubicza, The influence of chemical heterogeneities on the local mechanical behavior of a high-entropy alloy: A micropillar compression study, Materials Science and Engineering: A 721 (2018), 165-167.

6 Acknowledgement

In the spring of 2014, I was a graduate physicist at National University of Ungvár, and I got an opportunity to study abroad at the Department of Materials Physics at the ELTE. My senior tutor was Dr. Jenő Gubicza, who later became my supervisor during my doctoral work. Hereby, I would like to thank him for taking the lead as my supervisor and for his professional support by providing excellent research opportunities for my doctoral work.

I am grateful for the support of our head of department and head of the Materials Science and Solid State Physics program, Dr. István Groma. I am thankful to all colleagues / friends of the Department of Materials Physics of ELTE for their technical support. I am particularly grateful to Péter Szommer for measuring nanoindentations, Gábor Varga and Zoltán Dankházi for SEM investigations as well as János Lábár for TEM experiments. Additionally, I thank Dávid Ugi for his help in micropillar compression and Alajos Ö. Kovács for technical assistance. I am also grateful to Peter Jenei for his help and suggestions whenever I had any doubt.

Moreover, I appreciate Ádam Vida for his advice, discussions, and a lot of collaborated work from which I have always learned something new. In addition, Garima Kapoor, who was always there to help me and motivated me by being so optimistic. I would also like to thank her for reviewing my dissertation. I am especially grateful to my friend Tatjana Turányi for constant encouragement and for finding the time to review my dissertation, in addition to show curiosity in listening about my research progress, despite having different professional background.

I want to thank my foreign co-authors Guy Dirras, Terence G. Langdon and Megumi Kawasaki for their continuous cooperation.

Last but not least, I would like to thank my family for their continued support and motivation. Without them, it could not have been possible. To my fiancé, István Biró, who helped me a lot and kept with me in difficult times. I know it was not easy.

7 References

[1] B. Cantor, I. T. H. Chang, P. Knight, and A. J. B. Vincent, "Microstructural development in equiatomic multicomponent alloys," *Mater. Sci. Eng. A*, vol. 375–377, no. 1–2 SPEC. ISS., pp. 213–218, 2004.

[2] J. W. Yeh *et al.*, "Nanostructured high-entropy alloys with multiple principal elements: Novel alloy design concepts and outcomes," *Adv. Eng. Mater.*, vol. 6, no. 5, pp. 299–303, 2004.

[3] M. H. Tsai and J. W. Yeh, "High-entropy alloys: A critical review," *Mater. Res. Lett.*, vol. 2, no. 3, pp. 107–123, 2014.

[4] Z. Tang *et al.*, "Aluminum alloying effects on lattice types, microstructures, and mechanical behavior of high-entropy alloys systems," *Jom*, vol. 65, no. 12, pp. 1848–1858, 2013.

[5] Y. Zhang *et al.*, "Microstructures and properties of high-entropy alloys," *Prog. Mater. Sci.*, vol. 61, no. October 2013, pp. 1–93, 2014.

[6] D. B. Miracle, J. D. Miller, O. N. Senkov, C. Woodward, M. D. Uchic, and J. Tiley, "Exploration and development of high entropy alloys for structural applications," *Entropy*, vol. 16, no. 1, pp. 494–525, 2014.

[7] O. N. Senkov, G. B. Wilks, J. M. Scott, and D. B. Miracle, "Intermetallics Mechanical properties of Nb 25 Mo 25 Ta 25 W 25 and V 20 Nb 20 Mo 20 Ta 20 W 20 refractory high entropy alloys," *Intermetallics*, vol. 19, no. 5, pp. 698–706, 2011.

[8] O. N. Senkov, J. M. Scott, S. V. Senkova, D. B. Miracle, and C. F. Woodward, "Microstructure and room temperature properties of a high-entropy TaNbHfZrTi alloy," *J. Alloys Compd.*, vol. 509, no. 20, pp. 6043–6048, 2011.

[9] O. N. Senkov, S. V. Senkova, C. Woodward, and D. B. Miracle, "Low-density, refractory multi-principal element alloys of the Cr-Nb-Ti-V-Zr system: Microstructure and phase analysis," *Acta Mater.*, vol. 61, no. 5, pp. 1545–1557, 2013.

[10] O. N. Senkov, J. M. Scott, S. V. Senkova, F. Meisenkothen, D. B. Miracle, and C. F. Woodward, "Microstructure and elevated temperature properties of a refractory TaNbHfZrTi alloy," *J. Mater. Sci.*, vol. 47, no. 9, pp. 4062–4074, 2012.

[11] C. P. Lee, C. C. Chang, Y. Y. Chen, J. W. Yeh, and H. C. Shih, "Effect of the aluminium content of AlxCrFe1.5MnNi0.5high-entropy alloys on the corrosion behaviour in aqueous environments," *Corros. Sci.*, vol. 50, no. 7, pp. 2053–2060, 2008.

[12] M. A. Hemphill *et al.*, "Fatigue behavior of Al0.5CoCrCuFeNi high entropy alloys," *Acta Mater.*, vol. 60, no. 16, pp. 5723–5734, 2012.

[13] Y. Zou, H. Ma, and R. Spolenak, "Ultrastrong ductile and stable high-entropy alloys at small scales," *Nat. Commun.*, vol. 6, pp. 1–8, 2015.

[14] A. J. B. Vincent, "A study of three multicomponent alloys," University of Sussex, UK, 1981.

[15] P. Knight, "Multicomponent alloys," University of Oxford, UK, 1995.

[16] K. H. Huang, "A study on multicomponent alloy systems containing equal-mole elements," Hsinchu: National Tsing Hua University, 1996.

[17] B. S. Murty, J. W. Yeh, and S. Ranganathan, *High Entropy Alloys*. Elsevier, 2014.

[18] Y. Zou, S. Maiti, W. Steurer, and R. Spolenak, "Size-dependent plasticity in an Nb25Mo25Ta25W25refractory high-entropy alloy," *Acta Mater.*, vol. 65, pp. 85–97, 2014.

[19] X. B. Feng *et al.*, "Size effects on the mechanical properties of nanocrystalline NbMoTaW refractory high entropy alloy thin films," *Int. J. Plast.*, vol. 95, pp. 264–277, 2017.

[20] C. Parkin *et al.*, "Investigation of High-Entropy Alloys Compositions for Radiation Damage Applications," *Adv. Mater. Manuf.*, vol. 118, no. June, pp. 1583–1586, 2018.

[21] S. Xia, X. Yang, M. Chen, T. Yang, and Y. Zhang, "The Al Effects of Co-Free and V-Containing High-Entropy Alloys," *Metals (Basel).*, vol. 7, no. 1, p. 18, 2017.

[22] C. A. Gearhart, "Einstein before 1905: The early papers on statistical mechanics," *Am. J. Phys.*, vol. 58, no. 5, p. 468, 1990.

[23] A. R. Ruffa, "Thermal potential, mechanical instability, and melting entropy," *Phys. Rev. B*, vol. 25, no. 9, pp. 5895–5900, 1982.

[24] J. W. Yeh, "Recent progress in high-entropy alloys," *Ann. Chim. Sci. des Mater.*, vol. 31, no. 6, pp. 633–648, 2006.

[25] S. Ranganathan, "Alloyed pleasures: Multimetallic cocktails," *Curr. Sci.*, vol. 85, no. 10, pp. 1404–1406, 2003.

[26] S. Singh, N. Wanderka, B. S. Murty, U. Glatzel, and J. Banhart, "Decomposition in multi-component AlCoCrCuFeNi high-entropy alloy," *Acta Mater.*, vol. 59, no. 1, pp. 182–190, 2011.

[27] O. N. Senkov, G. B. Wilks, J. M. Scott, and D. B. Miracle, "Mechanical properties of Nb 25Mo 25Ta 25W 25 and V 20Nb 20Mo 20Ta 20W 20 refractory high entropy alloys," *Intermetallics*, vol. 19, no. 5, pp. 698–706, 2011.

[28] X. F. Wang, Y. Zhang, Y. Qiao, and G. L. Chen, "Novel microstructure and properties of multicomponent CoCrCuFeNiTixalloys," *Intermetallics*, vol. 15, no. 3, pp. 357–362, 2007.

[29] Y. J. Zhou, Y. Zhang, Y. L. Wang, and G. L. Chen, "Solid solution alloys of AlCoCrFeNi Tix with excellent room-temperature mechanical properties," *Appl. Phys. Lett.*, vol. 90, no. 18, 2007.

[30] Y. F. Kao, T. J. Chen, S. K. Chen, and J. W. Yeh, "Microstructure and mechanical property of as-cast, -homogenized, and -deformed AlxCoCrFeNi ($0 \leq x \leq 2$) high-entropy alloys," *J. Alloys Compd.*, vol. 488, no. 1, pp. 57–64, 2009.

[31] Y. Zhang, X. Yang, and P. K. Liaw, "Alloy design and properties optimization of high-entropy alloys," *Jom*, vol. 64, no. 7, pp. 830–838, 2012.

[32] A. Takeuchi and A. Inoue, "Classification of Bulk Metallic Glasses by Atomic Size Difference, Heat of Mixing and Period of Constituent Elements and Its Application to Characterization of the Main Alloying Element," *Mater. Trans.*, vol. 46, no. 12, pp. 2817–2829, 2005.

[33] Y. Zhang, Y. J. Zhou, J. P. Lin, G. L. Chen, and P. K. Liaw, "Solid-solution phase formation rules for multi-component alloys," *Adv. Eng. Mater.*, vol. 10, no. 6, pp. 534–538, 2008.

[34] F. Otto, Y. Yang, H. Bei, and E. P. George, "Relative effects of enthalpy and entropy on the phase stability of equiatomic high-entropy alloys," *Acta Mater.*, vol. 61, no. 7, pp. 2628–2638, 2013.

[35] J. W. Yeh, S. Y. Chang, Y. Der Hong, S. K. Chen, and S. J. Lin, "Anomalous decrease in X-ray diffraction intensities of Cu-Ni-Al-Co-Cr-Fe-Si alloy systems with multi-principal elements," *Mater. Chem. Phys.*, vol. 103, no. 1, pp. 41–46, 2007.

[36] K. Y. Tsai, M. H. Tsai, and J. W. Yeh, "Sluggish diffusion in Co-Cr-Fe-Mn-Ni high-entropy alloys," *Acta Mater.*, vol. 61, no. 13, pp. 4887–4897, 2013.

[37] O. N. Senkov, G. B. Wilks, D. B. Miracle, C. P. Chuang, and P. K. Liaw, "Refractory high-entropy alloys," *Intermetallics*, vol. 18, no. 9, pp. 1758–1765, 2010.

[38] J. Dąbrowa, W. Kucza, G. Cieślak, T. Kulik, M. Danielewski, and J. W. Yeh, "Interdiffusion in the FCC-structured Al-Co-Cr-Fe-Ni high entropy alloys: Experimental studies and numerical simulations," *J. Alloys Compd.*, vol. 674, pp. 455–462, 2016.

[39] M. Vaidya, S. Trubel, B. S. Murty, G. Wilde, and S. V. Divinski, "Ni tracer diffusion in CoCrFeNi and CoCrFeMnNi high entropy alloys," *J. Alloys Compd.*, vol. 688, pp. 994–1001, 2016.

[40] S. Guo, C. Ng, J. Lu, and C. T. Liu, "Effect of valence electron concentration on stability of fcc or bcc phase in high entropy alloys," *J. Appl. Phys.*, vol. 109, no. 10, 2011.

[41] Z. Li, A. Ludwig, A. Savan, H. Springer, and D. Raabe, "Combinatorial metallurgical synthesis and processing of high-entropy alloys," *J. Mater. Res.*, pp. 1–14, 2018.

[42] M. H. Tsai, K. Y. Tsai, C. W. Tsai, C. Lee, C. C. Juan, and J. W. Yeh, "Criterion for sigma phase formation in Cr- and V-Containing high-entropy alloys," *Mater. Res. Lett.*, vol. 1, no. 4, pp. 207–212, 2013.

[43] K. M. Youssef, A. J. Zaddach, C. Niu, D. L. Irving, and C. C. Koch, "A novel low-density, high-hardness, high-entropy alloy with close-packed single-phase nanocrystalline structures," *Mater. Res. Lett.*, vol. 3, no. 2, pp. 95–99, 2014.

[44] W. Ji *et al.*, "Alloying behavior and novel properties of CoCrFeNiMn high-entropy alloy fabricated by mechanical alloying and spark plasma sintering," *Intermetallics*, vol. 56, pp. 24–27, 2014.

[45] C. Z. Yao *et al.*, "Electrochemical preparation and magnetic study of Bi-Fe-Co-Ni-Mn high entropy alloy," *Electrochim. Acta*, vol. 53, no. 28, pp. 8359–8365, 2008.

[46] F. Yuhu, Z. Yunpeng, G. Hongyan, S. Huimin, and H. Li, "AlNiCrFexMo0.2CoCu High Entropy Alloys Prepared by Powder Metallurgy," *Rare Met. Mater. Eng.*, vol. 42, no. 6, pp. 1127–1129, 2013.

[47] P. Veronesi, E. Colombini, R. Rosa, C. Leonelli, and M. Garuti, "Microwave processing of high entropy alloys: A powder metallurgy approach," *Chem. Eng. Process. Process Intensif.*, vol. 122, pp. 397–403, 2017.

[48] E. Colombini, R. Rosa, L. Trombi, M. Zadra, A. Casagrande, and P. Veronesi, "High entropy alloys obtained by field assisted powder metallurgy route: SPS and microwave heating," *Mater. Chem. Phys.*, vol. 210, pp. 78–86, 2018.

[49] R. Feng, P. K. Liaw, M. C. Gao, and M. Widom, "First-principles prediction of high-entropy-alloy stability," *npj Comput. Mater.*, vol. 3, no. 1, pp. 1–6, 2017.

[50] S. Singh, N. Wanderka, B. S. Murty, U. Glatzel, and J. Banhart, "Decomposition in Multi-component AlCoCrCuFeNi High Entropy Alloy S. Singh," *Acta Mater.*, vol. 59, no. 1, pp. 182–190, 2011.

[51] Y. Long, K. Su, J. Zhang, X. Liang, H. Peng, and X. Li, "Enhanced strength of a mechanical alloyed NbMoTaWVTi refractory high entropy alloy," *Materials (Basel).*, vol. 11, no. 5, pp. 1–8, 2018.

[52] S. Praveen and H. S. Kim, "High-Entropy Alloys: Potential Candidates for High-Temperature Applications – An Overview," *Adv. Eng. Mater.*, vol. 20, no. 1, pp. 1–22, 2018.

[53] M. C. Gao, J.-W. Yeh, P. K. Liaw, and Y. Zhang, *High-Entropy Alloys: Fundamentals and Applications*. 2016.

[54] C. J. Tong *et al.*, "Mechanical performance of the AlxCoCrCuFeNi high-entropy alloy system with multiprincipal elements," *Metall. Mater. Trans. A Phys. Metall. Mater. Sci.*, vol. 36, no. 5, pp. 1263–1271, 2005.

[55] C. J. Tong *et al.*, "Microstructure characterization of Al x CoCrCuFeNi high-

entropy alloy system with multiprincipal elements," *Metall. Mater. Trans. A*, vol. 36, no. 4, pp. 881–893, 2005.

[56] C. W. Tsai, Y. L. Chen, M. H. Tsai, J. W. Yeh, T. T. Shun, and S. K. Chen, "Deformation and annealing behaviors of high-entropy alloy Al0.5CoCrCuFeNi," *J. Alloys Compd.*, vol. 486, no. 1–2, pp. 427–435, 2009.

[57] C. Li, J. C. Li, M. Zhao, and Q. Jiang, "Effect of alloying elements on microstructure and properties of multiprincipal elements high-entropy alloys," *J. Alloys Compd.*, vol. 475, no. 1–2, pp. 752–757, 2009.

[58] M. R. Chen, S.-J. Lin, J.-W. Yeh, M.-H. Chuang, S.-K. Chen, and Y.-S. Huang, "Effect of vanadium addition on the microstructure, hardness, and wear resistance of Al0.5CoCrCuFeNi high-entropy alloy," *Metall. Mater. Trans. A*, vol. 37, no. 5, pp. 1363–1369, 2006.

[59] F. Wang, Y. Zhang, G. Chen, and H. A. Davies, "Tensile and compressive mechanical behavior of a CoCrCuFeNiAl0.5 high entropy alloy," *Int. J. Mod. Phys. B*, vol. 23, no. 6–7, pp. 1254–1259, 2009.

[60] F. Otto, A. Dlouhý, C. Somsen, H. Bei, G. Eggeler, and E. P. George, "The influences of temperature and microstructure on the tensile properties of a CoCrFeMnNi high-entropy alloy," *Acta Mater.*, vol. 61, no. 15, pp. 5743–5755, 2013.

[61] B. Gludovatz, A. Hohenwarter, D. Catoor, E. H. Chang, E. P. George, and R. O. Ritchie, "A fracture-resistant high-entropy alloy for cryogenic applications," *Science* , vol. 345, no. 6201, pp. 1153–1158, 2014.

[62] Z. Wu, C. M. Parish, and H. Bei, "Nano-twin Mediated Plasticity in Carbon-containing FeNiCoCrMn High Entropy Alloys," *J. Alloys Compd.*, vol. 647, pp. 815–822, 2015.

[63] L. H. Wen, H. C. Kou, J. S. Li, H. Chang, X. Y. Xue, and L. Zhou, "Effect of aging temperature on microstructure and properties of AlCoCrCuFeNi high-entropy alloy," *Intermetallics*, vol. 17, no. 4, pp. 266–269, 2009.

[64] Z. Tang *et al.*, "Tensile ductility of an AlCoCrFeNi multi-phase high-entropy alloy through hot isostatic pressing (HIP) and homogenization," *Mater. Sci. Eng. A*, vol. 647, pp. 229–240, 2015.

[65] T. G. Langdon, "Twenty-five years of ultrafine-grained materials: Achieving exceptional properties through grain refinement," *Acta Mater.*, vol. 61, no. 19, pp. 7035–7059, 2013.

[66] R. Z. Valiev, "Bulk Nanostructured Materials: Fundamentals and Applications," pp. 434–435, 2014.

[67] J. Gubicza, N. Q. Chinh, J. L. Lábár, Z. Hegedus, and T. G. Langdon, "Twinning and dislocation activity in silver processed by severe plastic deformation," *J. Mater. Sci.*, vol. 44, no. 6, pp. 1656–1660, 2009.

[68] Y. B. Wang *et al.*, "The role of stacking faults and twin boundaries in grain refinement of a Cu-Zn alloy processed by high-pressure torsion," *Mater. Sci. Eng. A*, vol. 527, no. 18–19, pp. 4959–4966, 2010.

[69] A. P. Zhilyaev and T. G. Langdon, "Using high-pressure torsion for metal processing: Fundamentals and applications," *Prog. Mater. Sci.*, vol. 53, no. 6, pp. 893–979, 2008.

[70] D.-H. Lee *et al.*, "Nanomechanical behavior and structural stability of a nanocrystalline CoCrFeNiMn high-entropy alloy processed by high-pressure torsion," *J. Mater. Res.*, vol. 30, no. 18, pp. 2804–2815, 2015.

[71] B. Schuh, B. Völker, V. Maier-Kiener, J. Todt, J. Li, and A. Hohenwarter, "Phase Decomposition of a Single-Phase AlTiVNb High-Entropy Alloy after Severe Plastic Deformation and Annealing," *Adv. Eng. Mater.*, vol. 19, no. 4, pp. 1–10, 2017.

[72] H. Yuan *et al.*, "Atomic-scale homogenization in an fcc-based high-entropy alloy via severe plastic deformation," *J. Alloys Compd.*, vol. 686, pp. 15–23, 2016.

[73] Q. H. Tang, Y. Huang, Y. Y. Huang, X. Z. Liao, T. G. Langdon, and P. Q. Dai, "Hardening of an Al0.3CoCrFeNi high entropy alloy via high-pressure torsion and thermal annealing," *Mater. Lett.*, vol. 151, pp. 126–129, 2015.

[74] W. Wu *et al.*, "Dual mechanisms of grain refinement in a FeCoCrNi highentropy alloy processed by highpressure torsion," *Sci. Rep.*, vol. 7, pp. 1–13, 2017.

[75] K. Sharman *et al.*, "Enhancement in mechanical properties of a β-titanium alloy by high-pressure torsion," *J. Mater. Res. Technol.*, vol. 4, no. 1, pp. 79–83, 2015.

[76] R. Z. Valiev, Y. V. Ivanisenko, E. F. Rauch, and B. Baudelet, "Structure and deformaton behaviour of Armco iron subjected to severe plastic deformation," *Acta Mater.*, vol. 44, no. 12, pp. 4705–4712, 1996.

[77] H. Jiang, Y. T. Zhu, D. P. Butt, I. V. Alexandrov, and T. C. Lowe, "Microstructural evolution, microhardness and thermal stability of HPT-processed Cu," *Mater. Sci. Eng. A*, vol. 290, no. 1, pp. 128–138, 2000.

[78] A. Vorhauer and R. Pippan, "On the homogeneity of deformation by high pressure torsion," *Scr. Mater.*, vol. 51, no. 9, pp. 921–925, 2004.

[79] Z. Yang and U. Welzel, "Microstructure-microhardness relation of nanostructured Ni produced by high-pressure torsion," *Mater. Lett.*, vol. 59, no. 27, pp. 3406–3409, 2005.

[80] A. P. Zhilyaev, S. Lee, G. V. Nurislamova, R. Z. Valiev, and T. G. Langdon, "Microhardness and microstructural evolution in pure nickel during high-pressure torsion," *Scr. Mater.*, vol. 44, no. 12, pp. 2753–2758, 2001.

[81] A. P. Zhilyaev, G. V. Nurislamova, B. K. Kim, M. D. Baró, J. A. Szpunar, and T. G. Langdon, "Experimental parameters influencing grain refinement and microstructural evolution during high-pressure torsion," *Acta Mater.*, vol. 51, no. 3, pp. 753–765, 2003.

[82] Q. H. Tang, Y. Huang, Y. Y. Huang, X. Z. Liao, T. G. Langdon, and P. Q. Dai, "Hardening of an Al0.3CoCrFeNi high entropy alloy via high-pressure torsion and thermal annealing," *Mater. Lett.*, vol. 151, pp. 126–129, 2015.

[83] B. Schuh *et al.*, "Mechanical properties, microstructure and thermal stability of a nanocrystalline CoCrFeMnNi high-entropy alloy after severe plastic deformation," *Acta Mater.*, vol. 96, pp. 258–268, 2015.

[84] V. Maier-Kiener, B. Schuh, E. P. George, H. Clemens, and A. Hohenwarter, "Insights into the deformation behavior of the CrMnFeCoNi high-entropy alloy revealed by elevated temperature nanoindentation," *J. Mater. Res.*, vol. 32, no. 14, pp. 2658–2667, 2017.

[85] P. F. Yu *et al.*, "Effects of high pressure torsion on microstructures and properties of an Al0.1CoCrFeNi high-entropy alloy," *Mater. Sci. Eng. A*, vol. 655, pp. 283–291, 2016.

[86] H. Shahmir, M. Kawasaki, and T. G. Langdon, "The potential for achieving superplasticity in high-entropy alloys processed by severe plastic deformation," *IOP Conf. Ser. Mater. Sci. Eng.*, vol. 194, no. 1, pp. 1–6, 2017.

[87] H. Shahmir, M. Nili-Ahmadabadi, A. Shafie, and T. G. Langdon, "Hardening and thermal stability of a nanocrystalline CoCrFeNiMnTi0.1high-entropy alloy processed by high-pressure torsion," *IOP Conf. Ser. Mater. Sci. Eng.*, vol. 194, no. 1, pp. 1–6, 2017.

[88] B. E. Warren, *X-ray Diffraction*, Dover Publ. 1990.

[89] T. Ungár and J. Gubicza, "Nanocrystalline materials studied by powder diffraction line profile analysis," *Zeitschrift für Krist. - Cryst. Mater.*, vol. 222, no. 3–4, pp. 114–128, 2007.

[90] J. Gubicza, *X-Ray Line Profile Analysis in Materials Science*, IGI-Global, USA 2014.

[91] P. Jenei, "Porkohászati módszerekkel előállított ultrafinom szemcsés fémek mikroszerkezete és mechanikai tulajdonságai," PhD thesis, 2014.

[92] T. Ungár, J. Gubicza, G. Ribárik, A. Borbély, "Crystallite size distribution and dislocation structure determined by diffraction profile analysis: Principles and practical application to cubic and hexagonal crystals," *J. Appl. Crystallogr.*, vol. 34, no. 3, pp. 298–310, 2001.

[93] L. Balogh, G. Ribárik, and T. Ungár, "Stacking faults and twin boundaries in fcc crystals determined by x-ray diffraction profile analysis," *J. Appl. Phys.*, vol. 100, no. 2, 2006.

[94] T. Ungár, G. Ribárik, J. Gubicza, and P. Hanák, "Dislocation Structure and Crystallite Size Distribution in Plastically Deformed Metals Determined by Diffraction Peak Profile Analysis," *J. Eng. Mater. Technol.*, vol. 124, no. 1, p. 2, 2002.

[95] J. Gubicza, *Defect Structure and Properties of Nanomaterials*, Woodhead P. 2012.

[96] Z. Hegedűs, "Defect Structure in Ultra fine-grained Silver and a Copper-Silver Alloy Processed by Severe Plastic Deformation," PhD thesis, 2013.

[97] A. Guinier, *X-ray Diffraction*, Freeman. 1963.

[98] G. Ribárik, T. Ungár, and J. Gubicza, "MWP-fit: A program for multiple whole-profile fitting of diffraction peak profiles by ab initio theoretical functions," *J. Appl. Crystallogr.*, vol. 34, no. 5, pp. 669–676, 2001.

[99] B. E. Warren and B. L. Averbach, "The separation of cold-work distortion and particle size broadening in x-ray patterns," *J. Appl. Phys.*, vol. 23, no. 4, p. 497, 1952.

[100] M. Wilkens, "Fundamental Aspects of Dislocation Theory," Nat. Bur., vol. II, no. 317, R. B. J.A. Simmons, R. de Wit, Ed. Washington, DC. USA, 1970, pp. 1195–1221.

[101] I. Groma, T. Ungár, and M. Wilkens, "Asymmetric X-ray line broadening of plastically deformed crystals. I. Theory," *J. Appl. Crystallogr.*, vol. 21, no. 1, pp. 47–54, 1988.

[102] T. Ungár and G. Tichy, "The effect of dislocation contrast on X-ray line profiles in untextured polycrystals," *Phys. Status Solidi Appl. Res.*, vol. 171, no. 2, pp. 425–434, 1999.

[103] A. Borbély, J. Dragomir-Cernatescu, G. Ribárik, and T. Ungár, "Computer program ANIZC for the calculation of diffraction contrast factors of dislocations in elastically anisotropic cubic, hexagonal and trigonal crystals," *J. Appl. Crystallogr.*, vol. 36, no. 1, pp. 160–162, 2003.

[104] T. Ungár, E. Schafler, and J. Gubicza, "Microstructure of Bulk Nanomaterials Determined by X-Ray Line-profile Analysis," *Bulk Nanostructured Mater.*, no. iii, pp. 361–386, 2009.

[105] K. Nyilas, H. Couvy, P. Cordier, and T. Ungár, "The dislocation-structure and crystallite-size in forsterite (olivine) deformed at 1400°C by 11 GPa," *Zeitschrift fur Krist. Suppl.*, vol. 1, no. 23, pp. 135–140, 2006.

[106] G. K. Williamson and W. H. Hall, "X-ray line broadening from filed aluminium and wolfram," *Acta Metall.*, vol. 1, no. 1, pp. 22–31, 1953.

[107] E. J. Mittemeijer and U. Welzel, "The 'state of the art' of the diffraction analysis of crystallite size and lattice strain," *Zeitschrift fur Krist.*, vol. 223, no. 9, pp.

552–560, 2008.

[108] T. Ungár, I. Dragomir, Á. Révész, and A. Borbély, “The contrast factors of dislocations in cubic crystals: The dislocation model of strain anisotropy in practice,” *J. Appl. Crystallogr.*, vol. 32, no. 5, pp. 992–1002, 1999.

[109] J. Gubicza *et al.*, “Delayed microstructural recovery in silver processed by equal-channel angular pressing,” *J. Mater. Sci.*, vol. 43, no. 16, pp. 5672–5676, 2008.

[110] L. Balogh, G. Tichy, and T. Ungár, “Twinning on pyramidal planes in hexagonal close packed crystals determined along with other defects by X-ray line profile analysis,” *J. Appl. Crystallogr.*, vol. 42, no. 4, pp. 580–591, 2009.

[111] J. Gubicza and T. Ungár, “Characterization of defect structures in nanocrystalline materials by X-ray line profile analysis,” *Zeitschrift fur Krist.*, vol. 222, no. 11, pp. 567–579, 2007.

[112] V. Pecharsky and P. Zavalij, *Fundamentals of Powder Diffraction and Structural Characterization of Materials*, Springer US, 2009.

[113] G. Ribárik, J. Gubicza, and T. Ungár, “Correlation between strength and microstructure of ball-milled Al-Mg alloys determined by X-ray diffraction,” *Mater. Sci. Eng. A*, vol. 387–389, no. 1–2 SPEC. ISS., pp. 343–347, 2004.

[114] D. P. Nelson, J. B.; Riley, “An experimental investigation of extrapolation methods in the derivation of accurate unit-cell dimensions of crystals,” *Proc. Phys. Soc.*, vol. 57, no. 3, pp. 160–177, 1945.

[115] J. Gubicza, A. Juhász, and J. Lendvai, “A new method for hardness determination from depth sensing indentation tests,” *J. Mater. Res.*, vol. 11, no. 12, pp. 2964–2967, 1996.

[116] N. Q. Chinh, J. Gubicza, Z. Kovács, and J. Lendvai, “Depth-sensing indentation tests in studying plastic instabilities,” *J. Mater. Res.*, vol. 19, no. i, pp. 31–45, 2004.

[117] H. Couque, “The use of the direct impact Hopkinson pressure bar technique to describe thermally activated and viscous regimes of metallic materials The use of the direct impact Hopkinson pressure bar technique to describe thermally activated and viscous regimes of me,” 2014.

[118] G. Dirras, D. Tingaud, G. Csiszár, J. Gubicza, H. Couque, and F. Mompiou, “Characterization of bulk bimodal polycrystalline nickel deformed by direct impact loadings,” *Mater. Sci. Eng. A*, vol. 601, pp. 48–57, 2014.

[119] C. K. H. Dharan and F. E. Hauser, “Determination of Stress-Strain Characteristics at Very High Strain Rates,” *Exp. Mech.* , vol. September, no. September, pp. 370–376, 1970.

[120] D. M. Dimiduk et al., “Scale-Free Intermittent Flow in Crystal Plasticity” vol.

312, no. 5777, pp. 1188–1190, 2006.

[121] Z. Liu *et al.*, "Micromechanical characterization of casting-induced inhomogeneity in an Al0.8CoCrCuFeNi high-entropy alloy," *Scr. Mater.*, vol. 64, no. 9, pp. 868–871, 2011.

[122] P. D. Ispánovity, Á. Hegyi, I. Groma, G. Györgyi, K. Ratter, and D. Weygand, "Average yielding and weakest link statistics in micron-scale plasticity," *Acta Mater.*, vol. 61, no. 16, pp. 6234–6245, 2013.

[123] Á. I. Hegyi *et al.*, "Micron-Scale Deformation: A Coupled in Situ Study of Strain Bursts and Acoustic Emission," *Microsc. Microanal.*, vol. 23, no. 6, pp. 1076–1081, 2017.

[124] E. Fazakas *et al.*, "Experimental and theoretical study of Ti20Zr20Hf20Nb20X20(X = v or Cr) refractory high-entropy alloys," *Int. J. Refract. Met. Hard Mater.*, vol. 47, pp. 131–138, 2014.

[125] J. P. Couzinié *et al.*, "Microstructure of a near-equimolar refractory high-entropy alloy," *Mater. Lett.*, vol. 126, pp. 285–287, 2014.

[126] J. W. Yeh, Y. L. Chen, S. J. Lin, and S. K. Chen, "High-Entropy Alloys – A New Era of Exploitation," *Mater. Sci. Forum*, vol. 560, pp. 1–9, 2007.

[127] W. D. Vlassak, Joost J. and Nix, "Measuring the Elastic Properties of Materials By Means of Indentation," vol. 42, no. 8, 1994.

[128] J. Gubicza *et al.*, "Microstructure of severely deformed metals determined by X-ray peak profile analysis," *J. Alloys Compd.*, vol. 378, no. 1–2, pp. 248–252, 2004.

[129] J. Gubicza, N. Q. Chinh, G. Krállics, I. Schiller, and T. Ungár, "Microstructure of ultrafine-grained fcc metals produced by severe plastic deformation," *Curr. Appl. Phys.*, vol. 6, no. 2, pp. 194–199, 2006.

[130] G. Dirras, A. Ouarem, H. Couque, J. Gubicza, P. Szommer, and O. Brinza, "Microstructure and nanohardness distribution in a polycrystalline Zn deformed by high strain rate impact," *Mater. Charact.*, vol. 62, no. 5, pp. 480–487, 2011.

[131] J. P. Couzinié, L. Lilensten, Y. Champion, G. Dirras, L. Perrière, and I. Guillot, "On the room temperature deformation mechanisms of a TiZrHfNbTa refractory high-entropy alloy," *Mater. Sci. Eng. A*, vol. 645, pp. 255–263, 2015.

[132] G. I. Taylor, "Plastic strain in metals," *J. Inst. Met.*, vol. 62, pp. 307–324, 1938.

[133] Q. Li, "Modeling the microstructure-mechanical property relationship for a 12Cr-2W-V-Mo-Ni power plant steel," *Mater. Sci. Eng. A*, vol. 361, no. 1–2, pp. 385–391, 2003.

[134] R. Madec and L. P. Kubin, "Second-order junctions and strain hardening in bcc

and fcc crystals," *Scr. Mater.*, vol. 58, no. 9, pp. 767–770, 2008.

[135] P. L. Mosbrucker *et al.*, "Neutron and X-ray diffraction analysis of the effect of irradiation dose and temperature on microstructure of irradiated HT-9 steel," *J. Nucl. Mater.*, vol. 443, no. 1–3, pp. 522–530, 2013.

[136] B. Jóni, E. Schafler, M. Zehetbauer, G. Tichy, and T. Ungár, "Correlation between the microstructure studied by X-ray line profile analysis and the strength of high-pressure-torsion processed Nb and Ta," *Acta Mater.*, vol. 61, no. 2, pp. 632–642, 2013.

[137] L. Lilensten, J. P. Couzinié, L. Perrière, J. Bourgon, N. Emery, and I. Guillot, "New structure in refractory high-entropy alloys," *Mater. Lett.*, vol. 132, pp. 123–125, 2014.

[138] R. B. Figueiredo, P. R. Cetlin, and T. G. Langdon, "Using finite element modeling to examine the flow processes in quasi-constrained high-pressure torsion," *Mater. Sci. Eng. A*, vol. 528, no. 28, pp. 8198–8204, 2011.

[139] I. C. Dragomir and T. Ungár, "Contrast factors of dislocations in the hexagonal crystal system," *J. Appl. Crystallogr.*, vol. 35, no. 5, pp. 556–564, 2002.

[140] L. Lilensten *et al.*, "Design and tensile properties of a bcc Ti-rich high-entropy alloy with transformation-induced plasticity," *Mater. Res. Lett.*, vol. 5, no. 2, pp. 110–116, 2017.

[141] D. Tabor, *The Hardness of Metals*. Oxford University Press, New York, 1951.

[142] G. A. Salishchev *et al.*, "Effect of Mn and v on structure and mechanical properties of high-entropy alloys based on CoCrFeNi system," *J. Alloys Compd.*, vol. 591, pp. 11–24, 2014.

[143] B. Schuh *et al.*, "Mechanical properties, microstructure and thermal stability of a nanocrystalline CoCrFeMnNi high-entropy alloy after severe plastic deformation," *Acta Mater.*, vol. 96, pp. 258–268, 2015.

[144] B. Gludovatz, E. P. George, and R. O. Ritchie, "Processing, Microstructure and Mechanical Properties of the CrMnFeCoNi High-Entropy Alloy," *Jom*, vol. 67, no. 10, pp. 2262–2270, 2015.

[145] M. Kawasaki, "Different models of hardness evolution in ultrafine-grained materials processed by high-pressure torsion," *J. Mater. Sci.*, vol. 49, no. 1, pp. 18–34, 2014.

[146] A. J. Zaddach, C. Niu, C. C. Koch, and D. L. Irving, "Mechanical properties and stacking fault energies of NiFeCrCoMn high-entropy alloy," *Jom*, vol. 65, no. 12, pp. 1780–1789, 2013.

[147] J. Gubicza, N. Q. Chinh, J. L. Lábár, Z. Hegedus, and T. G. Langdon, "Principles of self-annealing in silver processed by equal-channel angular pressing: The significance of a very low stacking fault energy," *Mater. Sci. Eng. A*, vol. 527,

no. 3, pp. 752–760, 2010.

[148] Z. Hegedűs, J. Gubicza, M. Kawasaki, N. Q. Chinh, Z. Fogarassy, and T. G. Langdon, "Microstructure of low stacking fault energy silver processed by different routes of severe plastic deformation," *J. Alloys Compd.*, vol. 536, no. SUPPL.1, pp. 190–193, 2012.

[149] T. M. Smith *et al.*, "Atomic-scale characterization and modeling of 60°dislocations in a high-entropy alloy," *Acta Mater.*, vol. 110, pp. 352–363, 2016.

[150] F. Otto, N. L. Hanold, and E. P. George, "Microstructural evolution after thermomechanical processing in an equiatomic, single-phase CoCrFeMnNi high-entropy alloy with special focus on twin boundaries," *Intermetallics*, vol. 54, pp. 39–48, 2014.

[151] G. Laplanche, A. Kostka, O. M. Horst, G. Eggeler, and E. P. George, "Microstructure evolution and critical stress for twinning in the CrMnFeCoNi high-entropy alloy," *Acta Mater.*, vol. 118, pp. 152–163, 2016.

[152] G. Laplanche, P. Gadaud, O. Horst, F. Otto, G. Eggeler, and E. P. George, "Temperature dependencies of the elastic moduli and thermal expansion coefficient of an equiatomic, single-phase CoCrFeMnNi high-entropy alloy," *J. Alloys Compd.*, vol. 623, pp. 348–353, 2015.

[153] N. J. Petch, "The cleavage strength of polycrystals," *J. Iron Steel Inst.*, vol. 173, pp. 25–28, 1953.

[154] E. O. Hall, "The deformation and ageing of mild steel; discussion of results," *Proc. Phys. Soc. Lond. B*, vol. 64, pp. 47–753, 1951.

[155] A. Gali and E. P. George, "Tensile properties of high- and medium-entropy alloys," *Intermetallics*, vol. 39, pp. 74–78, 2013.

[156] K. Lu, L. Lu, and S. Suresh, "Strengthening Materials by engineering coherent internal Boundaries at the Nanoscale," *Science*, vol. 324, no. 5925, pp. 349–353, 2009.

[157] B. B. Rath, M. A. Imam, and C. S. Pande, "Nucleation and Growth of Twin Interfaces in Fcc Metals and Alloys," *Mater. Phys. Mech.*, vol. 1, pp. 61–66, 2000.

[158] E. Schafler *et al.*, "A second-order phase-transformation of the dislocation structure during plastic deformation determined by in situ synchrotron X-ray diffraction," *Acta Mater.*, vol. 53, no. 2, pp. 315–322, 2005.

[159] J. Gubicza, N. Q. Chinh, J. L. Lábár, S. Dobatkin, Z. Hegedus, and T. G. Langdon, "Correlation between microstructure and mechanical properties of severely deformed metals," *J. Alloys Compd.*, vol. 483, no. 1–2, pp. 271–274, 2009.

[160] F. H. Olivares and J. Gil Sevillano, "A quantitative assessment of forest-

hardening in f.c.c. metals," *Acta Metall.*, vol. 35, no. 3, pp. 631–641, 1987.

[161] A. H. W. Ngan, X. X. Chen, P. S. S. Leung, R. Gu, and K. F. Gan, "Size effects of micrometer-scaled metals - The search continues for materials containing real microstructures," *MRS Commun.*, vol. 7, no. 2, pp. 131–140, 2017.

[162] N. L. Okamoto, D. Kashioka, T. Hirato, and H. Inui, "Specimen- and grain-size dependence of compression deformation behavior in nanocrystalline copper," *Int. J. Plast.*, vol. 56, pp. 173–183, 2014.

SUMMARY

Defect Structure in Plastically Deformed High-Entropy Alloys

Anita Heczel

High-Entropy Alloys (HEAs) are disordered solid solutions, containing five or more principal elements in equal or near-equal atomic ratios, in which all the atomic concentrations are between 5% and 35%. These alloys are currently in the focus of materials science because they can have desirable properties, such as high hardness and strength, good resistance to thermal softening, oxidation, wear and corrosion.

The goal of my PhD work was to study the defect structure and mechanical properties in HEAs with different chemical compositions and crystal structures. The following results were obtained from the investigation of $Ti_{20}Zr_{20}Hf_{20}Nb_{20}Ta_{20}$, $Ti_{35}Zr_{27.5}Hf_{27.5}Nb_5Ta_5$ and $Co_{20}Cr_{20}Fe_{20}Mn_{20}Ni_{20}$ alloys:

1) The microstructure in body-centered cubic (bcc) $Ti_{20}Zr_{20}Hf_{20}Nb_{20}Ta_{20}$ high entropy alloy during quasi-static and dynamic compression tests were studied by X-ray line profile analysis (XLPA), electron backscatter diffraction and transmission electron microscopy. The average lattice constant and other important parameters of the microstructure such as the mean diffraction domain size, the dislocation density and the edge/screw character of dislocations were determined by XLPA. The elastic anisotropy factor required for XLPA procedure was determined by nanoindentation. XLPA showed that the diffraction domain size decreased while the dislocation density increased with increasing strain during compression. The average dislocation density for the strain rate of $4700\ s^{-1}$ is $47 \pm 7 \times 10^{14}\ m^{-2}$ which is much larger than the value determined for a quasi-statically compressed specimen ($15 \pm 2 \times 10^{14}\ m^{-2}$). It was revealed that with increasing strain the dislocation character became more screw. This can be explained by the reduced mobility of screw dislocations compared to edge dislocations in bcc structures. These observations are in line with TEM investigations. This HEA material has a high yield strength of about 890 MPa. The strain hardening during compression was caused by the increase of the dislocation density. The dislocation hardening parameter (α) in the Taylor equation has a relatively low value ($\sim$0.16) but it is still in the range determined for other bcc non-HEA metallic materials. The Peierls stress is the main component in the flow stress and dislocation hardening has a lower contribution even for high dislocation densities.

2) The influence of High-Pressure Torsion (HPT) on the microstructure and hardness of $Ti_{35}Zr_{27.5}Hf_{27.5}Nb_5Ta_5$ HEA was investigated. The evolution of the grain size due to 1 turn of HPT was studied by transmission electron microscopy. Besides the refinement of the microstructure, a phase transition also occurred during HPT, as revealed by X-ray diffraction. The initial bcc structure transformed into an orthorombic phase throughout the material. The features of this phase

transformation were studied on a sample compressed to low strain values. It was found that the phase transformation was nearly completed even at a strain of about 11.5%. XLPA evaluation revealed that there is no significant difference between the diffraction domain size values observed at the center and periphery of the disk. The average diffraction domain size was in the range of 11-16 nm. At the same time, the dislocation density increased with increasing the distance from the disk center. Its values were ~40×10^{14} m^{-2} and ~100×10^{14} m^{-2} at the disk center and periphery, respectively. The hardness in the center of the HPT-processed disk was ~3500 MPa which increases slightly towards the disk edge. At the periphery of the sample, the hardness was ~3900 MPa. The difference between the hardness values measured at the center and the periphery can be attributed to the variation of the dislocation density along the disk radius.

3) An equiatomic $Co_{20}Cr_{20}Fe_{20}Mn_{20}Ni_{20}$ HEA was processed by HPT. The evolution of the microstructure during HPT was investigated after 1/4, 1/2, 1 and 2 turns using electron backscatter diffraction and transmission electron microscopy. The spatial distribution of constituents was studied by energy-dispersive X-ray spectroscopy. The dislocation density and the twin-fault probability in the HPT-processed samples were determined by XLPA. It was found that the grain size was gradually refined from ~60 μm to ~30 nm while the dislocation density and the twin-fault probability increased to very high values of about 194×10^{14} m^{-2} and 2.7%, respectively, at the periphery of the disk processed for 2 turns. It was revealed that the low SFE of the equiatomic CoCrFeMnNi HEA is a deterministic factor in the development of the very high defect density (dislocations and twin faults) during HPT. At the same time, the minimum grain size in the HPT-processed CoCrFeMnNi HEA was much smaller than in Ag with very similar SFE, due to the significantly higher melting point of the HEA material. The hardness evolution was measured as a function of the distance from the center of the HPT-processed disks. After 2 turns of HPT, the microhardness increased from ~1440 MPa to ~5380 MPa at the disk periphery where the highest straining was achieved. A good correlation between the estimated and the calculated yield strength values was achieved using $\alpha=0.16$ and $k=21$ $MPa \cdot mm^{1/2}$ in the Taylor and Hall-Petch terms of yield strength. The relatively small value of α was attributed to the low SFE of the CoCrFeMnNi HEA since the clustering of highly dissociated dislocations in low SFE materials is hindered and the less clustered dislocation structure usually yields a small value of α in the Taylor equation. In addition, a micropillar compression study revealed that the chemical heterogeneities in the $Co_{20}Cr_{20}Fe_{20}Mn_{20}Ni_{20}$ HEA have only a negligible effect on the local mechanical behavior.

ÖSSZEFOGLALÁS

Rácshibák vizsgálata képlékenyen deformált nagy-entrópiás ötvözetekben

Heczel Anita

A nagy-entrópiás ötvözetek (angolul: high-entropy alloys, HEAs) olyan rendezetlen szilárd oldatok, amelyek öt vagy több fő elemet tartalmaznak egyenlő vagy közel azonos atomaránnyal, amelyek mennyisége az ötvözetekben 5% - 35 at.% között van. A HEA ötvözetekre egyre nagyobb figyelem irányul az anyagtudományi kutatásokban, mivel kiváló tulajdonságokkal rendelkeznek, úgymint nagy szilárdság és szívósság, nagy hőstabilitás, és jó korrózió- és kopásállóság.

A doktori munkám célja a HEA ötvözetek rácshibaszerkezetének és mechanikai tulajdonságainak tanulmányozása különböző kémiai összetételű és kristályszerkezetű ötvözetek esetén. A $Ti_{20}Zr_{20}Hf_{20}Nb_{20}Ta_{20,}$ $Ti_{35}Zr_{27.5}Hf_{27.5}Nb_5Ta_5$ és $Co_{20}Cr_{20}Fe_{20}Mn_{20}Ni_{20}$ összetételű ötvözetek vizsgálata során a következő következtetésekre jutottam:

1) A kvázi-statikus és dinamikus összenyomási vizsgálatok során a tércentrált köbös szerkezetű (bcc) $Ti_{20}Zr_{20}Hf_{20}Nb_{20}Ta_{20}$ HEA ötvözet mikroszerkezetét röntgen vonalprofil analízissel, visszaszórt elektron-diffrakcióval és transzmissziós elektronmikroszkópiával (TEM) vizsgáltam. A röntgen vonalprofil analízis segítségével meghatároztam az átlagos diffrakciós domén méretet, a diszlokáció sűrűséget és a diszlokációk él/csavar jellegét jellemző paramétert. Nanokeménységméréssel meghatároztam a vonalprofil kiértékelésekhez szükséges rugalmas anizotrópia faktort. A 4700 s^{-1}alakváltozási sebességgel alakított mintán a diszlokáció sűrűség $47 \pm 7 \times 10^{14}$ m^{-2} volt, ami sokkal nagyobb, mint a kvázi-statikusan összenyomott mintán mért érték ($15 \pm 2 \times 10^{14}$ m^{-2}). Arra is fény derült, hogy a növekvő deformációs sebességgel a diszlokációk csavar jelleget mutatnak. Ez azzal magyarázható, hogy az éldiszlokációkkal összehasonlítva a csavardiszlokációk nehezebben mozognak bcc anyagokban, így annihilációjuk is nehezebb. Ezek a megfigyelések jó összhangban vannak a TEM vizsgálatokkal. A vizsgált kiindulási HEA ötvözeten mért folyáshatár magas volt (~890 MPa). Az anyag keményedése az összenyomás során a diszlokáció sűrűség növekedésével magyarázható. A Taylor-egyenletben a diszlokációk keményítő hatását jellemző paraméter (α) viszonylag kis értékű (~0.16), de az még így is a hagyományos bcc ötvözetekre korábban kapott értékek közé esik. A folyásfeszültségben a Peierls feszültség adja a domináns járulékot, míg a diszlokációk okozta keményedés kisebb mértékű, még nagy diszlokáció sűrűségek esetén is.

2) Megvizsgáltam a nagynyomású csavarás (angolul: high-pressure torsion, HPT) hatását a titán gazdag $Ti_{35}Zr_{27.5}Hf_{27.5}Nb_5Ta_5$ HEA ötvözet mikroszerkezetére és keménységére. A mikroszerkezet fejlődését 1 HPT fordulat után elektron mikroszkópiával vizsgáltuk meg. A képlékeny deformáció során a szemcsefinomodással egyidejűleg fázisátalakulás is zajlik. A kiindulási bcc szerkezet ortorombos szerkezetűvé alakul át. Ennek a fázisátalakulásnak a tulajdonságait egytengelyű összenyomással tanulmányoztam. Megállapítottam, hogy a fázisátalakulás már kis deformáció értéknél (11.5%) szinte teljesen lezajlik. A röntgen vonalprofil kiértékelés azt mutatta, hogy nincs jelentős különbség a diffrakciós domén méret között a HPT korong közepén és szélén. Az átlagos diffrakciós domén méret 11-16 nm közé esett. Ugyanakkor a diszlokáció sűrűség nőtt a korong közepétől mért távolság függvényében. A korong közepén a diszlokáció sűrűség $\sim 40 \times 10^{14}$ m^{-2} volt, míg a szélén $\sim 100 \times 10^{14}$ m^{-2} értéket mértem. A HPT-vel deformált korong közepén a keménység ~3500 MPa volt, amely kissé nőtt a korong peremével közeledve. A peremen mért legnagyobb keménység ~3900 MPa volt. A korong középen és peremén mért keménység értékek közötti különbség magyarázható a korong sugara mentén mért a diszlokáció sűrűség változással.

3) Az ekvimoláris $Co_{20}Cr_{20}Fe_{20}Mn_{20}Ni_{20}$ HEA ötvözetet HPT-vel alakítottuk 1/4, 1/2, 1 és 2 fordulatig. A mikroszerkezet fejlődését visszaszórt elektron-diffrakcióval és transzmissziós elektronmikroszkópiával vizsgáltuk. Megállapítottam, hogy a legnagyobb mértékben deformált mintában (a 2 HPT-s korong peremén) a szemcseméret ~60 μm-ről ~30 nm-re finomodott, míg a diszlokáció sűrűség 194×10^{14} m^{-2} értékre növekedett és az ikerhibák valószínűsége is 2,7%-ra emelkedett. Megállapítottam, hogy az ekvimoláris $Co_{20}Cr_{20}Fe_{20}Mn_{20}Ni_{20}$ HEA alacsony rétegződési hibaenergiájának döntő szerepe van ezeknek a nagy rácshiba sűrűségeknek az elérésében. Ugyanakkor, a HPT-vel elért minimális szemcseméret sokkal kisebb, mint a hasonlóan fcc szerkezetű és alacsony rétegződési hibaenergiájú ezüstben kapott érték. Ezt a különbséget a HEA anyag nagyobb olvadáspontjával magyarázhatjuk. A HPT-vel deformált minták keménységét a korongok középpontjától mért távolság függvényében vizsgáltam meg. 2 HPT fordulat után a mikrokeménység 1440 MPa-ról 5380 MPa-ra emelkedett a korong szélén. A Taylor és Hall-Petch összefüggésekben használt anyagfüggő paramétereket (α és k) meghatároztam a számolt és mért folyáshatárok összehasonlításából. Viszonylag alacsony értéket kaptam α-ra, amit valószínűleg az alacsony rétegződési hibaenergia okoz, mivel az közvetve akadályozza a diszlokációk falakba rendeződését. Mikrooszlop összenyomással megállapítottam, hogy az ekvimoláris $Co_{20}Cr_{20}Fe_{20}Mn_{20}Ni_{20}$ HEA ötvözetben a kémiai heterogenítások csak kissé befolyásolják a lokális mechanikai viselkedést.

ADATLAP

a doktori értekezés nyilvánosságra hozatalához*

I. A doktori értekezés adatai

A szerző neve: Heczel Anita

MTMT-azonosító: 10051085

A doktori értekezés címe és alcíme: Defect structure in plastically deformed High-entropy Alloys

DOI-azonosító[46]: 10.15476/ELTE.2018.250

A doktori iskola neve: ELTE Fizika Doktori Iskola

A doktori iskolán belüli doktori program neve: Anyagtudomány és Szilárdtestfizika program

A témavezető neve és tudományos fokozata: Prof. Gubicza Jenő, egyetemi tanár

A témavezető munkahelye: ELTE Anyagfizikai tanszék

II. Nyilatkozatok

1. A doktori értekezés szerzőjeként
a) hozzájárulok, hogy a doktori fokozat megszerzését követően a doktori értekezésem és a tézisek nyilvánosságra kerüljenek az ELTE Digitális Intézményi Tudástárban. Felhatalmazom a Természettudományi kar Dékáni Hivatal Doktori, Habilitációs és Nemzetközi Ügyek Csoportjának ügyintézőjét, hogy az értekezést és a téziseket feltöltse az ELTE Digitális Intézményi Tudástárba, és ennek során kitöltse a feltöltéshez szükséges nyilatkozatokat.
b) kérem, hogy a mellékelt kérelemben részletezett szabadalmi, illetőleg oltalmi bejelentés közzétételéig a doktori értekezést ne bocsássák nyilvánosságra az Egyetemi Könyvtárban és az ELTE Digitális Intézményi Tudástárban;
c) kérem, hogy a nemzetbiztonsági okból minősített adatot tartalmazó doktori értekezést a minősítés (*dátum*)-ig tartó időtartama alatt ne bocsássák nyilvánosságra az Egyetemi Könyvtárban és az ELTE Digitális Intézményi Tudástárban;
d) kérem, hogy a mű kiadására vonatkozó mellékelt kiadó szerződésre tekintettel a doktori értekezést a könyv megjelenéséig ne bocsássák nyilvánosságra az Egyetemi Könyvtárban, és az ELTE Digitális Intézményi Tudástárban csak a könyv bibliográfiai adatait tegyék közzé. Ha a könyv a fokozatszerzést követőn egy évig nem jelenik meg, hozzájárulok, hogy a doktori értekezésem és a tézisek nyilvánosságra kerüljenek az Egyetemi Könyvtárban és az ELTE Digitális Intézményi Tudástárban.
2. A doktori értekezés szerzőjeként kijelentem, hogy
a) az ELTE Digitális Intézményi Tudástárba feltöltendő doktori értekezés és a tézisek saját eredeti, önálló szellemi munkám és legjobb tudomásom szerint nem sértem vele senki szerzői jogait;
b) a doktori értekezés és a tézisek nyomtatott változatai és az elektronikus adathordozón benyújtott tartalmak (szöveg és ábrák) mindenben megegyeznek.
3. A doktori értekezés szerzőjeként hozzájárulok a doktori értekezés és a tézisek szövegének plágiumkereső adatbázisba helyezéséhez és plágiumellenőrző vizsgálatok lefuttatásához.

Kelt: 2018.12.06.

Heczel Anita
……
a doktori értekezés szerzőjének aláírása

**ELTE SZMSZ SZMR 12. sz. melléklet*